

Smoothed Particle Dynamics Methods for the Simulation of Viscoelastic Fluids

vorgelegt von
Diplom-Physiker
Marco Ellero
aus Triest

Von der Fakultät II - Mathematik und Naturwissenschaften
der Technischen Universität Berlin
zur Erlangung des akademischen Grades
Doktor der Naturwissenschaften
– Dr. rer. nat –
genehmigte Dissertation

Promotionsausschuss:

Vorsitzender: Prof. Dr. rer. nat. Erwin Sedlmayr

Berichter: Prof. Dr. Siegfried Hess

Berichter: PD Dr. Martin Kröger

Tag der wissenschaftlichen Aussprache: 22. Juni 2004

Berlin 2004

D 83

Acknowledgments

First of all, I am deeply indebted to Prof. Dr. Siegfried Hess, who supervised this work and gave me the opportunity to study this fascinating subject with the freedom to choose research directions.

I am very grateful to PD Dr. Martin Kröger for having been my co-advisor. Without its fruitful hints and suggestions this work would have been difficult to complete.

Thanks are also due to Prof. Dr. Erwin Sedlmayr for having the kindness to head the examination committee.

In addition, I would like to thank Prof. Dr. Pep Español which gave me the possibility to join his group in Madrid and for having introduced me to the field of complex mesoscopic fluid dynamics. The time spent there has been for me an invaluable professional and human experience.

I am also very grateful to Dr. Patrick Ilg and Dr. Jose Cifre Hernandez for the stimulating conversations and discussions which we had in the last years. Of course, the same acknowledgment goes to all the people in my group: Igor Stankovic, Haiko Steuer and Nana Sadowsky.

I would like to thank specially Eloisa for her appreciable interest in listening to abstruse problems of fluid mechanics and of course for her love support.

Another thank goes also to all the friends of 'Kinzo'. My remember of Berlin could not be separated from them.

Finally, the most particular acknowledgment goes to my father Ennio and my mother Bruna. Without their constant love, presence and encourage I would not simply be here.

Abstract

This thesis is devoted to analytical and numerical studies of viscoelastic fluids. In first instance, a numerical scheme based on the Smoothed Particle Hydrodynamics method (SPH) is developed. The viscoelasticity is introduced macroscopically by incorporating a corotational Maxwell model for the stress tensor into the hydrodynamics equations. Numerical results are presented for a channel and shear flows in simple bulk and complex geometries. Whenever possible, the results are compared with analytical solutions. Furthermore, a viscoelastic material interacting with a periodic structure of rigid non-rotating cylindrical inclusions is investigated. The analysis of the multi-inclusion problem, widely used to model composite materials characterised by an internal microstructure, shows that the effective shear viscosity exhibits an increase which is linearly proportional to the volume concentration of the inclusions.

The second part is focused on the mesoscopic level of description. If the physical scales of the problem are smaller than a typical length, thermal fluctuations become relevant for the description of the system. As a numerical scheme at this level the Dissipative Particle Dynamics (DPD) is used. The mesoscopic model derived via DPD by ten Bosch for the study of polymer flows is generalised. The complex behaviour of polymeric fluids is captured by introducing an additional variable associated with each particle, thus collecting the elastic information about the fluid at scales “within” the dissipative particles. The ten Bosch model suffers from some conceptual shortcomings: it is not thermodynamically consistent, it is not possible to specify an arbitrary equation of state, nor has it a well-defined physical scale, and one needs kinetic theory to relate the transport coefficients of the fluid with the parameters of the model. Here a thermodynamically consistent generalisation of the ten Bosch model is formulated. The resulting algorithm is tested for a simple bulk shear flow showing the typical anisotropic distribution for the elongational variables. In addition, a rheological study of the steady-state viscometric functions is carried out, very good agreement with known theoretical solutions is found.

Finally, a hybrid technique is discussed for efficient multiscale simulations of polymer dynamics. A micro-macro numerical approach has emerged which avoids the use of constitutive equations for the stress tensor, which now is directly evaluated from the solution of an underlying Fokker-Planck equation by stochastic methods based on Brownian Dynamics. Although very promising, this multiscale approach is very demanding in terms of computer resources. In the last part of this thesis, a new hybrid method for efficient, i.e. memory saving, micro-macro simulations is presented and tested for a simple homogenous shear flow. The new method requires considerable smaller computer memory for comparable accuracy.

Zusammenfassung

Diese Dissertation ist analytischen und numerischen Studien viskoelastischer Fluide gewidmet. Zunächst wird ein numerisches Verfahren auf Basis der Smoothed-Particle-Hydrodynamics-Methode (SPH) entwickelt. Die Viskoelastizität wird hierbei makroskopisch eingeführt, indem die hydrodynamische Gleichungen um ein korotationales Maxwell-Modell für den Spannungstensor erweitert werden. Numerische Ergebnisse für Kanal- und Scherströmungen, sowohl im einfachen *bulk*, als auch in komplexen Geometrien werden angegeben. Wenn dies möglich ist, wird mit theoretischen Lösungen verglichen. Ausserdem wird ein viskoelastisches Material in Wechselwirkung mit einer periodischen Struktur starrer, nicht rotierender zylinderförmiger Einschlüsse untersucht. Die *multi-inclusion* Problem wird ferner benutzt, um Kompositmaterialien mit innerer Mikrostruktur zu modellieren. Die effektive Scherviskosität zeigt einen effektiven Anstieg, der linear proportional zur Volumenkonzentration der Einschlüsse ist.

Die zweite Teil dieser Arbeit konzentriert sich auf die mesoskopische Ebene der Beschreibung. Sobald die fuer das Stroemungsproblem relevanten Laengen und Abmessungen kleiner als eine materialabhaengige, intrinsische, Laengenskala sind, werden die thermische Fluktuationen wichtig fuer die Beschreibung des Systems. Eines der meistverwendeten Verfahren auf dieser Ebene ist die Dissipative-Particle-Dynamics-Methode (DPD). Das mesoskopische Modell zum Studium von Polymerströmungen, mithilfe der DPD entwickelt, wird verallgemeinert. Hierbei wird das komplexe Verhalten der Polymer-Fluessigkeiten durch eine zusätzliche Variable für jedes Teilchen beschrieben. Im vorliegenden Fall repraesentiert die Variable die Konformation eines Polymers. Diese sammelt die Information über die Elastizität der Flüssigkeit auf einer Skala von der Grössenordnung der dissipativen Polymer-Teilchen. Das ten Bosch-Modell zeigt einige konzeptionelle Unzulänglichkeiten: Es ist thermodynamisch nicht konsistent, es besitzt keine wohldefinierte physikalische Längenskala, und es benötigt die kinetische Theorie, um den Zusammenhang zwischen Transportkoeffizienten und Modellparametern herzustellen. Eine thermodynamisch konsistente Verallgemeinerung des ten Bosch-Modells wird in diesem Teil der vorliegenden Arbeit formuliert. Zusätzlich wird eine rheometrische Studie der stationären viskometrischen Funktionen durchgeführt, die wiederum sehr gute Übereinstimmung mit den bekannten theoretischen Lösungen zeigt.

Zuletzt wird eine Hybridmethode zur effizienten Durchführung mehrskaliger Polymerdynamik-Simulationen diskutiert. Ein 'Micro-Macro' numerischer Ansatz wurde kürzlich entwickelt, um die Verwendung von konstitutiven Gleichungen für den Spannungstensor zu vermeiden. Bei dieser Methode extrahiert man mithilfe stochastischer Methoden, basierend auf Brownscher Dynamik, den polymerischen Beitrag zum Spannungstensor direkt aus der Lösung der zugrundeliegenden Fokker-Planck-Gleichung. Obwohl dieser Multiskalenansatz sehr vielversprechend ist, benötigt er doch erhebliche Rechnerressourcen. Im letzten Teil der vorliegenden Arbeit wird eine neue Hybridmethode für effiziente (das heisst, Arbeitsspeicher sparende) Micro-Macro-Simulationen präsentiert und für eine einfachen, homogenen Scherströmung auch getestet. Die neue Methode benötigt für vergleichbare Genauigkeit weniger Arbeitsspeicher.

Contents

1	Introduction	9
1.1	Numerical methods for viscoelastic flows	10
1.1.1	Traditional macroscopic approaches	10
1.1.2	Micro-macro approaches	11
1.1.3	Lagrangian concepts in computational rheology	13
1.2	The Smoothed Particle Hydrodynamics method	14
1.3	Motivation of the present work	14
1.4	Outline of the thesis	15
2	The Smoothed Particle Hydrodynamics method	19
2.1	Basic SPH formalism	19
2.2	Hydrodynamics equations	21
2.2.1	Momentum equation	21
2.2.2	Energy equation	23
2.2.3	Continuity equation	24
2.3	Particle motion	25
2.4	Constitutive relations	26
2.4.1	Equation of state	26
2.4.2	Dissipation	28
2.5	The kernel function	30
2.6	Boundary conditions	32
2.6.1	Periodic boundary conditions	32
2.6.2	Rigid boundary conditions	34
2.7	Time integration	37
2.8	Numerical tests: the incompressible Newtonian flow	38
2.8.1	Couette flow	39
2.8.2	Poiseuille flow	41
3	Smoothed Particle Dynamics for viscoelastic flows	45
3.1	The constitutive equation	46
3.1.1	The corotational Maxwell model	46
3.1.2	The limiting case of vanishing elasticity	48
3.1.3	Non-dimensional formulation	48
3.2	Velocity profile relaxation in a 2D channel	49
3.3	Viscoelastic fluid under a steady shear flow	53

3.4	Viscoelastic matrix with solid inclusions	57
3.4.1	SPH implementation for the inclusion problem	58
3.4.2	Flow analysis: Newtonian matrix	59
3.4.3	Rheological analysis: non-Newtonian matrix	66
3.4.4	Flow analysis: non-Newtonian matrix	69
4	Smoothed Particle Dynamics for mesoscopic problems	75
4.1	Modelling mesoscopic flow problems	75
4.2	Mesoscopic simulations of complex fluids	77
4.3	TC fluid particle model of polymer solutions	78
4.4	GENERIC formulation	81
4.5	Reversible part of the dynamics	82
4.6	Irreversible part of the dynamics	85
4.7	Polymer diffusivity	91
4.8	Simulation results	96
4.8.1	Theoretical results for Hookean dumbbells	97
4.8.2	Setup of the numerical simulations	98
4.8.3	Numerical results	99
4.9	Final remarks	103
5	Multiscale simulations of viscoelastic flows	105
5.1	Micro-macro methods for complex fluids	106
5.2	Microscopic kinetic model and standard CT approach	108
5.3	The hybrid BDDFS method	111
5.4	Numerical results	116
5.5	Final remarks	122
6	Conclusions	125
A	Review of GENERIC	129
B	Microscopic calculation of entropy	131
C	Advection of a vector	135
D	Diffusion of dumbbells	137
E	SPH discretisation of the advection diffusion equation	139

Chapter 1

Introduction

It is known from the experience that whether a system behaves like a 'solid' or a 'fluid' is a matter of observation times. Fluids like water responds like a solid under very rapid deformations, while a glacier, usually considered quite hard, will flow like a fluid when observed on a sufficiently large time. If we assume that a solid is generally characterised by an elastic behaviour and a fluid by a viscous one, then a viscoelastic material, mathematically speaking, is a model in which these effects become comparable or, in other terms, where shear stresses are sustained for an appreciable time before flowing. Even if in principle, under specific circumstances, also the water can be described by a viscoelastic model, in practice this is of little interest, indeed the times at which its elastic behaviour has a considerable effect are so small (typically $10^{-10}s$) that phenomena of practical interest take place widely behind this scale and are very well described by its viscous dynamics, i.e Navier-Stokes equations. Nevertheless, a variety of fluids, whose behaviour differs from the Newtonian one, are usually encountered in real life. Indeed, it is easy comprehensible that materials like polymers solutions, polymers melts, foods and rubbers cannot be described within the classical formalism of the Newtonian fluid mechanics. At the same time, the interest into model their dynamics and predict their mechanical, thermal and rheological properties is of essential importance in many industrial and manufacturing sectors.

Materials like those mentioned above are characterised by a typical relaxation time for their internal microstructure which becomes comparable with the macroscopic scales, for example with the viscous diffusion time. The mathematical viscoelastic models are therefore required to describe the complex interactions between such phenomena, which manifest themselves in the governing equations usually as strong memory effects and functional dependence of the stress tensor upon its strain history. It is therefore expected that this complex interplay of effects is much more difficult to describe theoretically than in a Newtonian fluid and it reflects the complexity of the correspondent model equations. Although analytical solutions are available in simple cases, it is obvious that proceed by 'pencil and paper' is a quite hard challenge while, at the same time, the new frontiers opened by the increasing power and speed of digital computers allows for fast and accurate numerical solutions of the equation discussed above.

The main subject of this thesis is the numerical modelling of viscoelastic fluids, i.e.

polymer solutions, by using Lagrangian techniques derived by the Smoothed Particle Hydrodynamics method. In the present work, different approaches depending on the physical length and time scales are studied. Indeed, we will consider first a purely macroscopic approach based on the solution of a constitutive model equations combined with the usual hydrodynamics conservation laws; secondly, we will focus on the mesoscopic level of description, constructing a model for polymer solutions which is thermodynamically consistent, that is, equipped with fluctuations properly introduced in the fluid variables. Finally, we will investigate the interplay between such scales and attempt to develop efficient numerical techniques which can contribute to make the multiscale approach computationally feasible.

We start in the next section by giving a general overview of the numerical methods mostly used in the simulations of viscoelastic flows.

1.1 Numerical methods for viscoelastic flows

1.1.1 Traditional macroscopic approaches

Until recently, numerical simulations of viscoelastic flows in complex geometries have been often based on a purely *macroscopic* approach where one solves numerically the conservation laws together with a suitable rheological constitutive equation. In this area many numerical schemes have been proposed, generally based on finite difference (FDM), finite element (FEM), finite volume (FVM) or boundary element methods (BEM) to mention but a few [1,2,3]. One of the problems that emerges when trying to describe a non-Newtonian flow in this way is purely mathematical and is related to the correctness of the model constitutive equation adopted. Indeed, it is well-known that a rigorous derivation of the evolution equation for the macroscopic stress tensor starting from an “exact” kinetic theory is to date not available. In order to obtain a closed form relating the stress to the other macroscopic variables, many more or less physically motivated, approximations must be performed, which can alter, if not completely destroy, the viscoelastic properties of the original microscopic system [4,5]. Although progresses in the derivation of suitable constitutive equations for complex fluids, as polymer melts, foods, rubbers, has been very impressive, the subject, however, is by no means resolved and further developments are still called for. On the validity of macroscopic constitutive equations, the reader is referred for example to the monography by Tanner [6] or Larson [7].

Once the validity of a suitable model equation has been assumed, the second main problem, which the computational rheologists must face, is its numerical discretisation. Indeed, the constitutive equations can be cast into an integral or differential form and particular techniques must be developed in order to solve them accurately and in a reasonable time. It is beyond the scope of this introduction to review in detail all the numerical methods developed in this direction, nevertheless it has been widely recognised that one of the major challenges for the traditional schemes based on the solution of the constitutive equations cast in differential form, is the presence of the advective term which, whenever its contribution becomes dominant, can highly affect the stabil-

ity and the accuracy of the resulting algorithm. This is similar to the problem already encountered in advective-dominated Newtonian flows where special techniques must be implemented in order to ensure a safe, stable integration of the correspondent flow fields. A complete state-of-the-art review of the methods used in computational rheology can be found in [1, 2, 3, 8].

1.1.2 Micro-macro approaches

The classical numerical schemes presented above are based on the assumption of validity of a suitable constitutive equation describing a complex fluid. As already pointed out, the derivation of a consistent macroscopic model is an hard theoretical challenge and often, inaccurate approximations must be made in order to obtain a final manageable equation. Only very recently, a new class of methods, denoted as *micro-macro*, have appeared in the literature, which try to combine the macroscopic hydrodynamics (conservation laws) with un-approximated dynamics coming from a kinetic description of the microstructural model [9]. The basic idea is to split the dynamics of the system in two parts: at the macroscopic level, the usual conservation laws for mass, momentum and energy are solved by using traditional discretisation techniques, while the microscopic properties of the system are obtained by solving a kinetic theory model. This approach provides a consistent way to extract the evolution of the stress tensor for complex fluids, bypassing the need to use potentially inaccurate closure approximations. On the other hand, it should be pointed out that the solution of a kinetic theory model must be performed, in principle, on a very high-dimensional configurational space and, as a consequence, the technique can be very demanding in term of computer requirements. Although the approach can be considered in many complex situations, to date the method has been applied successfully only in relatively simple cases, characterised by low-dimensional configurational spaces, such as dilute suspensions of polymers described by quite coarse-grained models (dumbbells or 'small' chains). The starting point common to all the micro-macro approaches is the solution of a Fokker-Planck equations in the configurational space. Although, very recently some works have appeared in the literature showing that reasonably fast numerical solutions can be obtained by a crude direct discretisation of the Fokker-Planck equation based on a spectral method [10], it is generally acknowledged that even for low-dimensional configurational spaces (polymer chains characterised by $N > 3$ beads) the relative simulations require unacceptable CPU-time and memory.

For the sake of clarity, we next sketch the basic ideas of the micro-macro approaches, based on the standard method developed in the early 90's by Laso and Öttinger [11]. Here, instead of solving the deterministic Fokker-Planck equation, one solves an associated isomorphic set of stochastic differential equations for a large number of realizations. This is the so-called CONNFESSIT method (Calculation Of Non-Newtonian Flows using Finite Elements and Stochastic Simulation Techniques) which combines a Finite Element discretisation of the conservation laws with a stochastic evaluation of the stress tensor. A large number of polymer-models (i.e. dumbbells) are dispersed over all the physical domain and the stochastic differential equations must be integrated along the correspondent trajectories. The macroscopic stress is finally evaluated as an ensemble

average over many microscopic configurations. It is not the scope of this section to give an exact description of this method, which will be discussed in great details in Chapt. 5 of this work. Nevertheless, it is useful to outline here some of the drawbacks suffered by this approach. Maybe the most difficult problem is inherent to the stochastic nature of the methods and it is related to the determination of the macroscopic stress based on ensemble averages. If the number of realizations is not sufficiently large, large fluctuations can affect the macroscopic variables, eventually making the averaged signal indistinguishable. The reduction of such undesirable noise is a big challenge and is often referred to as *variance reduction problem*. We will come back to this point in the next section. Here we would like to focus on another drawback suffered by the standard micro-macro approaches. As it has been recognised by Keunings in its recent review [3], one difficulty is associated with the fact that the dumbbells are allowed to flow through the domain and, in order to evaluate their local contribution to the stress, one has to know at every time step in which spatial element they are contained. The consequent searching algorithm can cause a numerical bottleneck whenever the number of simulated dumbbells becomes quite large. On the other hand, a large number of dumbbells is often required in order to have a sufficiently large number of stochastic realizations for permitting accurate, noise-free averages. This problem is by nature due to the Lagrangian character of the dumbbells dynamics which contrast with the fixed Eulerian discretisation for the macroscopic flow fields.

The method of the Brownian Configuration Fields (BCF), recently introduced by van den Brule [12], partially solves the problem, by considering a continuous, totally correlated (in space) configurational field instead of a discrete set of uncorrelated dumbbells. In this way, one bypass the need to consider dumbbells advection through the Eulerian grid, but one solves directly a partial differential stochastic equation for the configurational field. One of the problems of this approach lies in the fact that completely artificial correlations over the physical domain are assumed in order to deal with a continuous field. Of course, this hypothesis becomes questionable whenever dealing with problems characterised by physical fluctuations.

A semi-Lagrangian numerical scheme, Lagrangian Particle method (LPM), has now been introduced by Keunings in the attempt to solve such difficulties [13]. This method combines, in a decoupled fashion, the Eulerian solution of the conservation laws (using a Galerkin finite elements technique) with a Lagrangian computation of the extra-stress at a number of discrete particles that are convected by the flow. The extra-stress is computed by integrating along the particle paths either the relevant differential constitutive equation (macroscopic approach), or the stochastic differential equation associated to the kinetic theory model (micro-macro approach). In the micro-macro LPM simulations, each Lagrangian particle convected by the flow carries an ensemble of particles with internal degrees of freedom, which can be statistically uncorrelated or correlated. Keeping track of the motion of this 'small' set of Lagrangian particle is not an expensive task and, at the same time, it permits the avoidance of the problem of using dispersed dumbbells and the consequent time-consuming searching algorithm. The time-history for the flow variables is here directly accessible in every Lagrangian particle and we can regard the microscopic dumbbells as a constant set of stochastic realizations of

the same process. The technique seems to be very useful and it has been applied successfully to a variety of viscoelastic problems. Nevertheless, the Eulerian-Lagrangian formalism requires to have at least three particles in every element of the Eulerian grid in order to perform an interpolation for the stress tensor. Modification of the original LPM method have been developed in the last years which corrects this drawback and improves its efficiency. In the opinion of the author, the LPM method seems to be the most promising, and surely the most flexible, micro-macro method presently available. Its strength is mainly due to the natural way in which it takes into account the typical advective character of the stochastic differential equations presented above. Nevertheless, as it has been recognised by Keunings, some problems still exist which are related to the exchange of information between the Eulerian grid and the Lagrangian particles. Smoothing effects due to this transfer, have been shown to affect the accuracy and the stability of the resulting algorithm. In this context, a fully Lagrangian description could permit to avoid such numerical artifacts.

1.1.3 Lagrangian concepts in computational rheology

From the discussions presented above, it emerges quite clearly that one of the main difficulties in the numerical simulation of viscoelastic fluids, is often related to the intrinsic advective character of the governing equations. This happens, both in the macroscopic and in the micro-macro approaches. In the first case, the hyperbolic nature of the differential constitutive equation seems to affect strongly the stability and the accuracy of the Eulerian based algorithm used for the numerical solution. As already mentioned, many of these problems can be partially remedied by using the large staff of numerical results available for the analogous problem of advective-dominated Newtonian flows (high Reynolds number). For these simulations, many specific techniques have been developed to deal with the hyperbolic character of the resulting equations as for example the well-known “upwind” scheme, which, in the case of viscoelastic flows simulations, consists of considering a further artificial diffusivity tensor in the constitutive equation acting in the streamline direction. Although the method has been able to successfully reproduce many viscoelastic flows, some doubts still remain on its final resulting accuracy which seems to be limited to first order [3].

As mentioned above, the problem also presents itself in the context of micro-macro approaches. Here, it is related to the advective flow of the model dumbbells dispersed over the flow domain, for which time-consuming searching algorithms are required. It seems therefore natural to apply ideas from a Lagrangian framework to such kind of fluids, trying to avoid directly all the problems related to the complicate treatment of advective terms, which now disappear, automatically absorbed by the material derivative. In addition to these theoretical argumentations, the Lagrangian picture can represent the best framework to deal with general flow problems represented by complex boundary conditions, free-surface flows or flows characterised by large deformations, where the classical Eulerian schemes encounter many difficulties. In this work, a numerical methods based on a fully Lagrangian formalism will be presented and applied specifically to viscoelastic flow problems. In the next section, a brief historical review with a list of the most relevant applications of the method will be given.

1.2 The Smoothed Particle Hydrodynamics method

Smoothed Particle Hydrodynamics (SPH) is a Lagrangian ‘macro’ method developed twenty-five years ago for astrophysical problems by Lucy [14], Gingold and Monaghan [15]. SPH is a fully Lagrangian scheme permitting to discretize a prescribed set of macroscopic equations by interpolating the flow properties directly at a discrete set of points, i.e. pseudo-particles, distributed randomly over the domain of solution, without the need to define a spatial mesh. Its Lagrangian nature, associated to the absence of a fixed grid, is its main strength allowing to remove difficulties associated to convective term and to tackle fluid and solid flow problems involving large deformations and free surfaces in a relatively natural way. In the last ten years many SPH simulations have been applied to different physical situations including compressible Newtonian flows [16], incompressible free surface flows [17], high strain mechanics, ultrarelativistic shocks [18], impact and sliding friction problems between elasto-plastic materials [19, 20, 21, 22], numerical fluid [23] and gas dynamics in astrophysics [24]. The SPH method has been also applied to problems in kinetic theory, such as the dynamics of homogeneous liquid crystals [25] based on a Fokker-Planck approach while implementations of standard SPH for parallel architectures have become recently available [26]. In addition, a detailed mathematical study showing the numerical convergence of the methodology has been carried out by Pulvirenti et al. [27]

The method has received substantial theoretical support in order to make it consistent from a statistical point of view, that is correct treatments of thermal fluctuations and consistent fluctuating hydrodynamics [28]. In Ref. [29], a close connection is made between SPH and Dissipative Particle Dynamics (DPD), a fully Lagrangian method in which the force between the particles are modelled on the mesoscale, following the philosophy of Lattice Boltzmann or Lattice Gas Automata schemes but with the advantage of the flexibility being gridless. Recently, application of DPD to viscoelastic flow has been proposed consisting in assigning to every DPD particle one or more internal structural variables [30].

The increasing literature that has appeared in recent years on SPH shows that the method has been improved, correcting many of its original shortcoming and applying it to a variety of physical problems involving fluid and solid-mechanics. Nevertheless, although its success for numerical modelling in the areas above mentioned, it is clear that this method has not yet achieved its mature stadium but many theoretical and computational improvements are still called for in order to compare it with the well-established field of the Eulerian grid-based techniques.

1.3 Motivation of the present work

The goal of the present work is to investigate the applications of the Smoothed Particle Hydrodynamics methods in the context of viscoelastic flows modelling. The SPH literature that has appeared in this area, seems to be a rarity in contrast with the potential contribution that such Lagrangian technique could offer. To our knowledge, the only paper published on this argument, except ours, has appeared last year and

involves a numerical study of a Non-Newtonian free-surface flow [31]. Unfortunately, the constitutive equation used was based on a generalised Newtonian fluid while it is commonly believed that such a model have only a limited range of applicability and it is too 'simple' to describe complex flows where the elastic effects play a crucial role. The introduction of viscoelasticity in the SPH method through a macroscopic constitutive Maxwell model and the consequent application to many different flow problems, i.e. channel-flows, bulk-shear flows or flows in complex geometries, is the main issue of the first part of this work. The results demonstrates that, accurate and stable solutions can also be obtained in unsteady situations.

Particular attention is also paid to the modelling of mesoscopic flow problems via the SPH method. It is obvious that at such 'small' level of description, the fluctuations emerging in the system dynamics represent a crucial physical ingredient and they should be carefully introduced in the numerical model. Indeed, if one is interested in resolving submicronic scales, it is of fundamental importance to have a fluid particle whose variables are equipped with thermal fluctuations consistent with the first and second laws of thermodynamics. The construction of a thermodynamically consistent viscoelastic fluid model suitable for mesoscale simulations is another goal of the present thesis.

Finally, as already mentioned in the previous section, a big issue concerning micro-macro simulations of viscoelastic flows is the one related to the variance reduction. In particular flows of interest, a large number of stochastic realizations must be taken into account in order to extract reliable averaged quantities. Indeed, it is well-known that in the limit of small elasticity, whenever the variance reduction techniques, such as BCF, are numerically not applicable or physically not motivated, averaged results extracted by the stochastic runs are affected by unacceptable noise. The way to reduce it is of course to increase the dimensions of the stochastic ensemble with the obvious associated numerical difficulties in term of CPU-time and mainly memory requirements for the correspondent algorithm. It is the last scope of this work, to study possible hybrid algorithms based on standard Brownian Dynamics methods, able to obtain accurate results at lower memory price. The hybrid BDDFS (Brownian Dynamics and Distribution Function) method presented in the last chapter of this thesis, could offer an alternative for those particular viscoelastic flows (i.e turbulent) where a large number of freedom degrees are necessary for accurate stochastic estimates of the flow variables.

1.4 Outline of the thesis

The present work is organised as follows.

Chapt. 2 describes the basic ideas of the Smoothed Particle Hydrodynamics (SPH) method. In particular, a weak formulation for the discretized equations based on the rigorous derivation of Benz [32], is presented for the conservation equations of mass, momentum and energy. The accuracy of the resulting discretized equations is also discussed, demonstrating that, under suitable choice of the interpolation functions, a numerical method which is second order accurate in space can be obtained. Particular

attention is devoted also to the problem of closure for the hydrodynamics equations for the well-established case of a Newtonian compressible fluid, providing at the same time some technical details regarding treatment of boundary conditions and time integration of the flow fields. Finally, some numerical results are shown proving the correctness of the numerical scheme to simulate a Newtonian fluid in simple flow geometries.

Chapt. 3 is devoted to the generalisation of the SPH method previously introduced for the description of more complex viscoelastic fluids. The formalism describing viscoelasticity is introduced in the ordinary conservation laws by providing a further independent partial differential constitutive equations for the stress tensor based on the corotational Maxwell model. In order to test the validity of this description for non-Newtonian fluids, the numerical method is applied to non-stationary relaxation processes in a 2D channel geometry and simple bulk shear flows, for which analytical comparisons are available. Finally, once the accuracy of the method in simple situations is proven, the model is applied to the specific problem of a viscoelastic bulk matrix contaminated with non-rotating rigid circular inclusions and underlying a steady-shear flow. The so called 'multi-inclusion' problem is widely adopted in literature to model composite materials characterised by a microstructure. A study of interplay between its macroscopic rheological properties and the microstructure is carried out giving evidence that some few microscopic parameters have a major influence on the effective transport properties of the material.

Chapt. 4 deals with the simulations of viscoelastic flow at a mesoscopic level. It is obvious that whenever the length scale characterising a specific problem becomes quite small, fluctuations in the physical quantities represent a crucial ingredient for the dynamics. On the other hand, it is important to introduce such fluctuations into the description in a consistent way. This chapter is focused on a particular viscoelastic Dissipative Particle Dynamics model, recently proposed by ten Bosch in [30], and it is put into a thermodynamically consistent form that allows for non-isothermal situations. This model consists of fluid particles that have an additional elastic vector characterising the state of elongation of the molecules within the fluid particle. Very simple physical mechanisms are proposed for the dynamics of the elastic vector that, with the help of the GENERIC formalism, allows us to derive the full set of dynamic equations for the model. The model is further generalised to include polymer diffusion. The connection of the present model with the CONNFFESSIT approach and the Brownian Configuration Fields approach is finally discussed.

Chapt. 5 proposes and test the 'Brownian Dynamics and Distribution Function Storing' (BDDFS) strategy for performing numerical calculations of viscoelastic complex flows based on the unapproximated CONNFFESSIT-type approach. Hardware limits this established approach for highly complex flows due to fluctuations which come together with the stochastic determination of the macroscopic extra stress tensor. As soon as the number of cells in the flow domain becomes large an even much larger number of freedom degrees must be used to extract accurate results. Usually, variance reduction techniques are used to suppress noise, lower the memory requirements, produce correlated dynamics, and obtain approximate, and 'good' results. BDDFS is a numerical method for the still approximate, but 'uncorrelated' solution of the same

problem with limited memory needs. It relies on a discrete storage of the configurational distribution function (D-CDF) for dumbbells, or polymers. Configurational variables subject to standard BD are sampled consistently with the D-CDF. Compared with the original approach, the memory requirement is reduced by the ratio between the number of D-CDF grid points and the number of molecules. The strategy has been tested against a homogeneous shear flow of dumbbells. Results reveal that the BDDFS concept may offer advantages upon alternative approaches which must become larger with the complexity of the system under study and whenever molecular correlations on length scales larger than the grid size contain information relevant to interpret experiments.

Chapter 2

The Smoothed Particle Hydrodynamics method

In this chapter we review the basic formalism of the Smoothed Particle Hydrodynamics (SPH) method which will be used in the following of the thesis in the attempt to generalise it for the description of more complex viscoelastic fluids. After recalling in the first section the basic SPH ideas based on interpolation theory, we derive rigorously, in section 2.2, a weak SPH formulation for the discretized hydrodynamics equation. Section 2.3 describes briefly the Lagrangian evolution of the adaptative grid constituted by the SPH particles, while section 2.4 is devoted to the problem of physical closure for the hydrodynamics equations, that is, the choice of suitable constitutive relations for pressure and friction stress. In particular, in Sec. 2.4.1 we review many forms of equations of state usually adopted in the literature discussing positive and negative aspects in relation with their numerical implementation. The description of a mechanism of viscous dissipation is the subject of section 2.4.2, where we discuss firstly the historical approach consisting in the introduction of a completely artificial viscosity and, secondly, the consistent approach followed in our work and based on a direct discretisation of the Navier-Stokes friction stress tensor. Section 2.5 deals with the accuracy of the scheme which, translated in the SPH formalism, corresponds to the choice of a suitable interpolating kernel. Sections 2.6 and 2.7 are devoted to the description of technical aspects of the numerical implementation, respectively boundary conditions and time integration. Finally, in section 2.8 we present some numerical results and comparison with known theoretical solution in the cases of a Couette and Poiseuille flows of a Newtonian incompressible fluid.

2.1 Basic SPH formalism

It has been shown that SPH can be derived in the context of interpolation theory [14,15]. Any function f , defined over a domain of interest and representing some physical variable or density, can be expressed in terms of its values at a discrete set of disordered points (SPH particle positions) by suitable definition of an interpolation kernel. Let us start with some basic definitions: given a function f defined over all the domain Ω , we can

always write it as

$$f(\mathbf{x}) = \int_{\Omega} f(\mathbf{x}') \delta(\mathbf{x} - \mathbf{x}') d\mathbf{x}', \quad (2.1)$$

where $\delta(\mathbf{x})$ is the Dirac delta function centred at the position \mathbf{x} . Eq. (2.1) is an identity and it is referred as *integral representation* of a function $f(\mathbf{x})$.

Let us introduce now the concept of the *integral estimate* $\langle f \rangle$ at the point \mathbf{x} . If we replace the Dirac delta function in (2.1) with an *interpolating kernel* $W(\mathbf{x} - \mathbf{x}', h)$, we obtain

$$\langle f(\mathbf{x}) \rangle = \int_{\Omega} f(\mathbf{x}') W(\mathbf{x} - \mathbf{x}', h) d\mathbf{x}', \quad (2.2)$$

which represents evidently an approximation of $f(\mathbf{x})$ so far as the kernel function is not exactly equal to the Dirac delta. Here, h represents the range of the interpolating kernel if it is supposed to have compact support, or, for example in the case of Gaussian kernel, its width at half height. In order to obtain a correct integral estimate $\langle f \rangle$, usually the following two assumptions are made

$$\int_{\Omega} W(\mathbf{x} - \mathbf{x}', h) d\mathbf{x}' = 1, \quad (2.3)$$

and

$$\lim_{h \rightarrow 0} W(\mathbf{x} - \mathbf{x}', h) = \delta(\mathbf{x} - \mathbf{x}'). \quad (2.4)$$

These features assure proper normalisation and consistency in the continuum limit. Concerning accuracy, the approximation corresponding to Eq. (5.1) is known to be second order in space. This can be easily shown [32], considering the fact that $W(\mathbf{x} - \mathbf{x}, h)$ is a strongly peaked function at $\mathbf{x} = \mathbf{x}'$ and therefore we can expand $f(\mathbf{x}')$ in a Taylor series around \mathbf{x} . If $W(\mathbf{x}, h)$ is an even function, particularly in the case $W(\mathbf{x}, h) = W(|\mathbf{x}|, h)$, the term of order $O(h)$ vanishes automatically and Eq. (5.1) becomes

$$\langle f(\mathbf{x}) \rangle = f(\mathbf{x}) + C \nabla^2 f(\mathbf{x}) h^2 + O(h^3), \quad (2.5)$$

where C is a coefficient independent of h . Provided that f varies quite smoothly on a length scale of the dimensions h , this relation gives a leading error term which is proportional to h^2 with a resulting accuracy for the SPH discretisation of the second order in space.

In addition, a further approximation is introduced at this point which is purely numerical and it corresponds to an estimate of the integral in (5.1) as a sum over points of the domain. To this end, let us introduce the concept of number density which defines the positions of a disordered set of points where the physical properties of the system are considered known,

$$n(\mathbf{x}) = \sum_j \delta(\mathbf{x} - \mathbf{x}_j). \quad (2.6)$$

We can therefore associate the infinitesimal integration volume $d\mathbf{x}'$ with the quantity ϕ_j (volume occupied by the j -th particle), which is defined through the replacement rule

$$d\mathbf{x}' \rightarrow \phi_j \equiv \frac{m_j}{\rho_j}, \quad (2.7)$$

where we introduced the concepts of mass m_j and density $\rho_j = m_j \langle n(\mathbf{x}_j) \rangle$ associated with the j -th particle. The final SPH approximation for a function f defined in some point \mathbf{x} reads

$$\langle f(\mathbf{x}) \rangle \simeq \sum_j \frac{m_j}{\rho_j} f_j W(|\mathbf{x} - \mathbf{x}_j|, h), \quad (2.8)$$

and $f_j \equiv f(\mathbf{x}_j)$. By substituting the function mass density $f(\mathbf{x}) = \rho(\mathbf{x})$ into (5.5) we obtain the following expression

$$\langle \rho(\mathbf{x}) \rangle \simeq \sum_j m_j W(|\mathbf{x} - \mathbf{x}_j|, h). \quad (2.9)$$

This is a direct way to evaluate the density explicitly as a sum over the particles and justifies the original denomination ‘‘SPH’’ in the sense that the particles are not intended like points but their masses are smoothed out over a distance of order h . A good overview of the mathematical basis of SPH can be found for example in Benz [32] or Monaghan [33, 34].

2.2 Hydrodynamics equations

Keeping in mind the definitions and the approximations introduced in the previous section, we will present here the derivation of a weak SPH form for the continuity, momentum and energy equations. This will be obtained following the rigorous approach of Benz [32]. The basic step consists actually in an integration over all the domain of the partial differential equations describing the conservation laws of continuum mechanics. An integration by parts removes therefore a surface term permitting to differentiate directly the interpolating kernel which is analytic. We postpone the section dealing with the evaluation of the mass density which requires a particular discussion.

2.2.1 Momentum equation

Let us consider the equation for the conservation of momentum which describes the balance of momentum fluxes on a macroscopic (continuum assumption) volume of fluid. Written in the Eulerian form, it reads

$$\frac{\partial V^\alpha}{\partial t} + (V^\beta \nabla^\beta) V^\alpha = \frac{1}{\rho} \nabla^\beta P^{\alpha\beta}, \quad (2.10)$$

where tensorial notation with Greek indices indicating spatial coordinates and the summation convention for repeated indices is used. As usual, V^α denotes the velocity field

and $P^{\alpha\beta}$ is the general stress tensor. By multiplying both sides of Eq. (2.10) by the kernel function and integrating over the spatial domain Ω we obtain

$$\int_{\Omega} \left(\frac{\partial V^{\alpha}}{\partial t} + (V^{\beta} \nabla'^{\beta}) V^{\alpha} \right) W(|\mathbf{x} - \mathbf{x}'|, h) d\mathbf{x}' = \int_{\Omega} \left(\frac{1}{\rho} \nabla'^{\beta} P^{\alpha\beta} \right) W(|\mathbf{x} - \mathbf{x}'|, h) d\mathbf{x}', \quad (2.11)$$

where ∇' represents the spatial gradient in the integration variable \mathbf{x}' . Let us consider now the LHS of Eq. (2.11). We rewrite it in the following way

$$\begin{aligned} \frac{\partial}{\partial t} \int_{\Omega} V^{\alpha} W(|\mathbf{x} - \mathbf{x}'|, h) d\mathbf{x}' + \int_{\Omega} V^{\beta} \nabla'^{\beta} V^{\alpha} W(|\mathbf{x} - \mathbf{x}'|, h) d\mathbf{x}' \\ = \frac{\partial \langle V^{\alpha} \rangle}{\partial t} + \langle V^{\beta} \rangle \nabla^{\beta} \langle V^{\alpha} \rangle = \frac{d \langle V^{\alpha} \rangle}{dt} + O(h^2), \end{aligned} \quad (2.12)$$

where the term $V^{\beta} \nabla'^{\beta} V^{\alpha}$ has been expanded in Taylor series around $\mathbf{x}' = \mathbf{x}$ similarly to Eq. (2.5). This allows us to extract the Lagrangian derivative from the integration. The RHS of Eq. (2.10) needs some more attention. Let us notice that

$$\frac{1}{\rho} \nabla^{\beta} P^{\alpha\beta} = \nabla^{\beta} \left(\frac{P^{\alpha\beta}}{\rho} \right) + \frac{P^{\alpha\beta}}{\rho^2} \nabla^{\beta} \rho. \quad (2.14)$$

By substituting this expression in the RHS of Eq. (2.11), we have

$$\int_{\Omega} \nabla'^{\beta} \left(\frac{P^{\alpha\beta}}{\rho} \right) W(|\mathbf{x} - \mathbf{x}'|, h) d\mathbf{x}' + \int_{\Omega} \frac{P^{\alpha\beta}}{\rho^2} \nabla'^{\beta} \rho W(|\mathbf{x} - \mathbf{x}'|, h) d\mathbf{x}'. \quad (2.15)$$

We can therefore apply the divergence theorem to the first term of the previous equation which becomes

$$\int_{\Omega} \nabla'^{\beta} \left(\frac{P^{\alpha\beta}}{\rho} \right) W(|\mathbf{x} - \mathbf{x}'|, h) d\mathbf{x}' = \int_{\Sigma} \frac{P^{\alpha\beta}}{\rho} W(|\mathbf{x} - \mathbf{x}'|, h) n^{\beta} d\Sigma - \int_{\Omega} \frac{P^{\alpha\beta}}{\rho} \nabla'^{\beta} W(|\mathbf{x} - \mathbf{x}'|, h) d\mathbf{x}'. \quad (2.16)$$

where Σ represents the boundary containing the physical domain Ω . Now, assuming that the boundary conditions lie at an infinite distance, we can neglect the surface term. If boundary conditions are present, clearly this term is no longer neglectable, but it should be taken into account. We will come back on this point in the section 2.6.

In addition, considering the fact that $\nabla' W(|\mathbf{x} - \mathbf{x}'|, h) = -\nabla W(|\mathbf{x} - \mathbf{x}'|, h)$, we are able to extract the differential operator out of the integration obtaining the following expression for the RHS of Eq. (2.11)

$$\nabla^{\beta} \int_{\Omega} \frac{P^{\alpha\beta}}{\rho} W(|\mathbf{x} - \mathbf{x}'|, h) d\mathbf{x}' + \int_{\Omega} \frac{P^{\alpha\beta}}{\rho^2} \nabla^{\beta} \rho W(|\mathbf{x} - \mathbf{x}'|, h) d\mathbf{x}'. \quad (2.17)$$

Finally, using Eq. (5.1) and by expanding in Taylor series the function $P^{\alpha\beta}/\rho^2$ around

$\mathbf{x}' = \mathbf{x}$ (neglecting terms of order h^2), we obtain the integral Lagrangian form of Eq. (2.10)

$$\frac{d}{dt} \langle V^\alpha \rangle = \nabla^\beta \left\langle \frac{P^{\alpha\beta}}{\rho} \right\rangle + \frac{P^{\alpha\beta}}{\rho^2} \nabla^\beta \langle \rho \rangle + O(h^2). \quad (2.18)$$

where we substituted $\rho = \langle \rho \rangle$. By using the particle approximation corresponding to Eq. (5.5), Eq. (2.18) becomes

$$\frac{d}{dt} \langle V^\alpha \rangle = \nabla^\beta \left(\sum_j m_j \frac{P_j^{\alpha\beta}}{\rho_j^2} W(|\mathbf{x} - \mathbf{x}_j|, h) \right) + \frac{P^{\alpha\beta}(\mathbf{x})}{\rho^2(\mathbf{x})} \nabla^\beta \left(\sum_j m_j W(|\mathbf{x} - \mathbf{x}_j|, h) \right). \quad (2.19)$$

Finally, evaluating the previous equation on the particle location \mathbf{x}_i and by reordering the terms, we obtain the final SPH discretized equation for the momentum

$$\frac{dV_i^\alpha}{dt} = \sum_j m_j \left(\frac{P_i^{\alpha\beta}}{\rho_i^2} + \frac{P_j^{\alpha\beta}}{\rho_j^2} \right) \nabla_i^\alpha W_{ij}, \quad (2.20)$$

where Roman indices indicate particles and V_i^α is the smooth velocity corresponding to the i -th particle. Here we used also the abbreviation $W_{ij} \equiv W(|\mathbf{x}_i - \mathbf{x}_j|, h)$. Because of $\nabla_i W_{ij} = -\nabla_j W_{ij}$, we have, that the contribution to the force acting on the i -th particle due to the j -th particle $F_{ij} = -F_{ji}$ and the momentum is automatically and exactly conserved from the bulk particles. This is a property of this particular set of equations, in fact it must be pointed out that there is not a unique derivation of them. A large number of different sets of SPH equations, all describing the same physics to the second order accuracy, can be in principle found using other approximations. The equation (5.7) is, on the other hand, preferable because it conserves exactly the momentum. Many different forms of SPH have been discussed by Monaghan [33].

2.2.2 Energy equation

Let us consider now the equation for the conservation of energy. In the adiabatic case, we can neglect the heat flux and the equation reflects the first law of thermodynamics. Written in Eulerian form, it reads

$$\frac{\partial U}{\partial t} + (V^\beta \nabla^\beta) U = \frac{P^{\alpha\beta}}{\rho} \nabla^\alpha V^\alpha, \quad (2.21)$$

where U represents the specific (for unit of mass) internal energy of the fluid. By repeating the same steps described for the derivation of the momentum equation, that is integrating by parts and neglecting surface terms, we obtain the following second order accurate SPH discretisation of Eq. (2.21)

$$\frac{dU_i}{dt} = -\frac{P_i^{\alpha\beta}}{\rho_i} \sum_j m_j (V_i^\alpha - V_j^\alpha) \nabla_i^\beta W_{ij}, \quad (2.22)$$

where $U_i = \langle U_i \rangle$ is the smooth internal energy of the i -th particle. It can be shown that this equation conserves automatically the total energy. In order to prove this, we identify the global energy of the i -th particle with $E_i = m_i U_i + K_i$, where $K_i = (1/2)m_i V_i^2$ is its kinetic energy. Let us consider now the total global energy (due to the contribution of every SPH particle) $E = \sum_j E_j$. We want to show that $\dot{E} = 0$. At this end, we evaluate firstly the time variation of the global internal energy $U = \sum_i m_i U_i$

$$\frac{dU}{dt} = \sum_i \frac{d}{dt} m_i U_i = - \sum_{i,j} m_i m_j \frac{P_i^{\alpha\beta}}{\rho_i^2} (V_i^\alpha - V_j^\alpha) \nabla_i^\beta W_{ij}, \quad (2.23)$$

where we used Eq. (2.22). Looking at the previous equation, we notice that, simply by swapping the indices, the result of the summation remains the same but we get a slightly different expression for \dot{U}

$$\frac{dU}{dt} = - \sum_{i,j} m_i m_j \frac{P_j^{\alpha\beta}}{\rho_j^2} (V_i^\alpha - V_j^\alpha) \nabla_i^\beta W_{ij}, \quad (2.24)$$

Therefore, we can rewrite Eq. (2.23) as follows

$$\frac{dU}{dt} = -\frac{1}{2} \sum_{i,j} m_i m_j \left(\frac{P_i^{\alpha\beta}}{\rho_i^2} + \frac{P_j^{\alpha\beta}}{\rho_j^2} \right) (V_i^\alpha - V_j^\alpha) \nabla_i^\beta W_{ij}, \quad (2.25)$$

Let us evaluate now the time variation of the global kinetic energy K

$$\frac{dK}{dt} = \frac{1}{2} \frac{d}{dt} \sum_i m_i (V_i^\alpha V_i^\alpha) = \sum_i m_i V_i^\alpha \frac{d}{dt} V_i^\alpha \quad (2.26)$$

$$= \sum_{i,j} m_i m_j V_i^\alpha \left(\frac{P_i^{\alpha\beta}}{\rho_i^2} + \frac{P_j^{\alpha\beta}}{\rho_j^2} \right) \nabla_i^\beta W_{ij}, \quad (2.27)$$

where we used Eq. (5.7) to express \dot{V}_i^α . Analogously to the previous case, by swapping the indices we obtain a different but equivalent form for \dot{K} , in such a way that Eq. (2.27) can be rewritten as follows

$$\frac{dK}{dt} = \frac{1}{2} \sum_{i,j} m_i m_j \left(\frac{P_i^{\alpha\beta}}{\rho_i^2} + \frac{P_j^{\alpha\beta}}{\rho_j^2} \right) (V_i^\alpha - V_j^\alpha) \nabla_i^\beta W_{ij}, \quad (2.28)$$

This shows that $\dot{U} = -\dot{K}$ and therefore the total energy is globally conserved in an adiabatic case.

2.2.3 Continuity equation

As already anticipated, the density calculation requires a particular attention. The natural way to evaluate it is indeed that one mentioned in the first section and corresponding to solve directly Eq. (2.9) which, for the i -th particle, reads

$$\rho_i = \sum_j m_j W(|\mathbf{x}_i - \mathbf{x}_j|, h). \quad (2.29)$$

This calculation takes into account the contribution of every particle lying within the range of the i -th particle. It could seem that this procedure involves a computational complexity for the algorithm of order N^2 where N is the total number of particles. Indeed, this is the case when a kernel function with infinite range is considered (i.e. Gaussian kernel). Nevertheless, provided that the support of the kernel function is compact, the particles which contribute to the estimate of a quantity in some points are only those neighbours whose distance is smaller than h . In this case many acceleration techniques can be used such as the popular ‘linked’ or ‘layered linked cell’ algorithms which reduce the order of interactions per time step to $N \log N$ [35,36].

Using the expression (2.29) has the main advantage upon other formulations that the mass is conserved exactly provided only that the number of particles is constant. On the other hand it poses a number of problems concerning boundary and edge effects. Artificial boundary layers can cause instabilities and/or slowing down the code requiring a very small time step for reliable trajectory evaluations near the walls. We will consider these problems in detail in the section concerning boundary conditions.

The alternative formulation for the density evaluation follows the standard derivation given for momentum and energy. The starting point is the continuity equation which reads

$$\frac{\partial \rho}{\partial t} + (V^\alpha \nabla^\alpha) \rho = -\rho \nabla^\alpha V^\alpha, \quad (2.30)$$

In analogy to the procedure described in the previous sections, for the density one obtains the following SPH discretisation

$$\frac{d\rho_i}{dt} = -\rho_i \sum_j \frac{m_j}{\rho_j} (V_i^\alpha - V_j^\alpha) \nabla_i^\alpha W_{ij}. \quad (2.31)$$

This strategy is preferable for problems involving free-boundaries and also establishes a computational advantage, that is, all the variable fields can be evaluated in one step without the need of a pre-loop for the density calculation. On the other hand, the relation (2.31) does not retain the exact mass conservation.

2.3 Particle motion

As already stressed, the Smoothed Particle Hydrodynamics method does not need a underlying grid to evolve the physical quantities, but they are interpolated directly on the SPH particles which move “with the fluid” through the domain. The motion of a SPH particle obeys therefore the following equation:

$$\frac{dX_i^\alpha}{dt} = V_i^\alpha, \quad (2.32)$$

where we used here the notation X_i^α to indicate the position of the i -th particle and V_i^α is evaluated from (5.7). It has been noticed in earlier SPH works that, for flow problems characterised by high velocities, some penetration between the particles can occur when using Eq. (2.32). This causes the density field to vary over the domain

producing fluctuations, which can be highly overdamped in the pressure field if a quasi-incompressible equation of state is used (see next section). A large amount of noise enters therefore in the velocity field (via the momentum equation), causing instabilities and eventually cracking down the code. One possibility to remove such effects is to evolve the particles with a velocity which takes into account the mean flow around them. Monaghan proposed the so called XSPH variant [33]

$$\frac{dX_i^\alpha}{dt} = V_i^\alpha + \varepsilon \sum_j \frac{m_j}{\rho_{ij}} (V_j^\alpha - V_i^\alpha) W_{ij}, \quad (2.33)$$

where $\rho_{ij} = (\rho_i + \rho_j)/2$ and ε is a factor which should have a value between 0 and 1. The correction term in Eq. (2.33) represents the difference between the velocity of the i -th particle and the mean flow. It has been shown that this expression still conserves both linear and angular momentum preventing, on the other hand, compenetration between the particles. This smoothing procedure has proven to reduce the fluctuations present in the velocity field and stabilise the code. As final remark, it should be pointed out that Balsara et al. showed that this procedure is the SPH analogy of the filtering operators commonly used in finite difference schemes and suggested a value for ε similar to 0.1 for best results.

2.4 Constitutive relations

The set of conservation equations (2.10,2.21,2.30) collected in the previous section is not closed. We need a closure relationship which expresses the stress tensor as function of known variables. In the case of an isothermal flow we require $P^{\alpha\beta} = P^{\alpha\beta}(\rho, V^\alpha)$. A general form for the symmetric stress tensor can be obtained by splitting it in two parts

$$P^{\alpha\beta} = -p\delta^{\alpha\beta} + \sigma^{\alpha\beta}, \quad (2.34)$$

where p is the ordinary *hydrostatic pressure* at equilibrium and $\sigma^{\alpha\beta}$ is the *friction stress tensor*. In the following we will discuss different constitutive equations relating the previous quantities to the basic set of independent variables.

2.4.1 Equation of state

A closure relation for p in (2.34) is given from an equation of state relating hydrostatic pressure to local density. Many possible forms for this can be adopted depending on the particular problem. Ideal gas-like equation $p(\rho) \propto \rho$ have been mostly found in the literature, while Hoover chose an equation of state with quadratic dependence on ρ to simulate viscous and heat conducting gases [37].

$$p(\rho) = \alpha \rho^2, \quad (2.35)$$

Particular attention should be given to the problem of incompressible fluids modelling. Indeed, in that case a realistic liquid equation of state is too expensive to solve computationally, therefore an artificial one must be used. One possibility is to use eq. (2.35)

with a choice of the parameter α such that the resulting speed of sound c_0

$$c(\rho) \equiv \sqrt{\frac{\partial p(\rho)}{\partial \rho}} \simeq \sqrt{2\alpha\rho_0}, \quad (2.36)$$

is suitably larger than a typical flow velocity V characterising the model. It has been argued by Monaghan that a choice of c_0 being ten times larger than this typical velocity V should diminish density fluctuations under a level comparable with the squared Mach number M^2 ($M \equiv V/c_0$) which in this case corresponds to 1%. This condition of *quasi incompressibility* introduces of course small errors due to density fluctuations but these are consistent with the global accuracy of SPH which comes together with the interpolation process.

One problem of this equation is that it can introduce a large amount of noise in the simulation when used to simulate flow characterised by high speeds of sound. In order to clarify this point, let us consider the SPH discretisation of the momentum equation for an inviscid fluid (where $P^{\alpha\beta}$ has been neglected) equipped with the equation of state given in (2.35). The SPH form of the momentum equation (5.7) becomes

$$\frac{dV_i^\alpha}{dt} = 2\alpha m_0 \sum_j \nabla_i^\alpha W_{ij}, \quad (2.37)$$

where we assumed a constant mass m_0 for every SPH particle. Now, looking at the momentum equation (2.10), one can easily notice that the pressure term appears under differential operator. That is, only variations of the pressure field are important, while its reference value is left out of the dynamics. Therefore, the presence of a constant density field ρ_0 produces a constant pressure field which should give no contributions to the particle accelerations, independently on its absolute value.

If we use eq. (2.29), the constant-density contribution to the acceleration of the i -th particle due to the j -th particle is $2\alpha m_0 \nabla_i^\alpha W_{ij}$, which is in principle different from zero. Now, assuming to be in the continuum limit (number of particle $N \rightarrow \infty$), we will have a very large number of particle randomly distributed in the neighbourhood of the i -th particle and therefore, all the contributions appearing in eq. (2.37) will delete exactly by symmetry.

Nevertheless, from a numerical point of view the picture is quite different. Indeed there will be always a *finite* number of SPH particles distributed inhomogeneously in the neighbourhood of a particular location \mathbf{x}_i and, consequently, the summation in (2.37) will introduce spurious fluctuating terms proportional to c_0^2 . Therefore, for incompressible flow problems, modelled by large values of the speed of sound, this spurious term can introduce a big amount of numerical noise in the simulations.

Another equation widely used, mainly in the case of free-surface flows, is the follow one

$$p(\rho) = p_0 \left(\left(\frac{\rho}{\rho_0} \right)^\gamma - 1 \right). \quad (2.38)$$

proposed initially by Batchelor [39] with $\gamma = 7$ for the description of water. A property of this equation of state is that it introduces an equilibrium pressure reference equal to zero.

This can be sometimes seen as an advantage because it reduces the random fluctuations coming from the SPH discretisation of the term $\nabla p/\rho$ appearing in the momentum equation. On the other hand it must be noticed that, although the advantages above mentioned, the equation of state (4.66) exhibits numerical instabilities in particular flow situations where the mass density decreases under the equilibrium value ρ_0 (specially for regions characterised by a very low pressure). In this case, the pressure contributions become negative, resulting in attractive force between the particle and causing the code to cracking down.

Finally, let us notice that an exact treatment of the incompressibility should take into account a further kinematic constraint on the velocity field which ensures its divergence-freeness [38].

2.4.2 Dissipation

It has often been observed that numerical solutions usually present large unphysical oscillations and are unstable if a dissipative term is not introduced in the equations. This is because shocks are always present – mostly in the first stages when initial conditions must relax – and if they are not well enough smeared out on a length scale larger than the discretisation step h , strong instabilities can occur.

In order to introduce a mechanism of dissipation in our model, let us consider the friction stress tensor appearing in Eq. (2.34). This symmetric stress tensor can be rewritten as the sum of an isotropic plus a symmetric traceless (anisotropic) part

$$\sigma^{\alpha\beta} = \sigma\delta^{\alpha\beta} + \overline{\sigma}^{\alpha\beta}, \quad (2.39)$$

where σ is a dynamic pressure responsible of volumetric changes and $\overline{\sigma}^{\alpha\beta}$ is the deviatoric traceless tensor related to shape deformations preserving volumes.

The formalism introduced above is purely mathematical and does not provide still any physical information about the friction stress tensor. Let us restrict now our analysis to the simple case of Newtonian fluids. In that case, it can be show that, on the basis of physical considerations, we can motivate the following two constitutive relations for the Newtonian friction stress tensor, [40]

$$\sigma = \zeta\nabla^\alpha V^\alpha, \quad \overline{\sigma}^{\alpha\beta} = 2\eta\overline{\nabla^\alpha V^\beta} = \eta\left(\nabla^\alpha V^\beta + \nabla^\beta V^\alpha - \frac{2}{d}\delta^{\alpha\beta}\nabla^\alpha V^\alpha\right) \quad (2.40)$$

where η and ζ are, respectively, the shear and bulk viscosities. This corresponds to the well-known stress tensor appearing in the Navier-Stokes equations for viscous compressible Newtonian fluids.

The natural way to proceed should be to discretize, in the SPH formalism, the contribution of the friction stress $\sigma^{\alpha\beta}$ and to add it to the hydrostatic pressure term. As it can be seen in Eq. (2.40), $\sigma^{\alpha\beta}$ is proportional to gradients of the velocity field, i.e. terms like $\nabla^\beta V^\alpha$. It should be also noticed that the stress tensor enters into the momentum equation under divergence operation, therefore, we should perform SPH discretizations of terms containing second derivatives of the velocity field, i.e. $\nabla^\alpha\nabla^\beta V^\alpha$.

Now, there are basically two ways to perform this discretisation. One possibility is to

consider a double differentiation of the interpolating kernel. Although this procedure can be shown to produce quite accurate results in simple cases, it introduces large scattering in the results when the particle are spatially disordered. As we will see in the next chapter, this problem becomes evident when dealing with simulations in complex geometries which involve complicated particle-paths.

The other possibility is to consider a preliminary SPH discretisation for the first derivatives of the velocity field (producing the following tensor field $(\nabla^\alpha V^\beta)_i$ defined for the every particle) and therefore, in a second loop, a further derivation of the previously estimated field. As for the previous case, also this approach does not solve completely the problem of the large fluctuations present in the evaluated quantities and, on the other hand, introduces nested sums over the particles causing the code to slow down. Nevertheless, it should be pointed out that one way to improve the accuracy and reduce the scatter is by employing higher-order kernel functions (i.e. quintic spline), which, although involving a little extra CPU-time, permit to reduce the noise and stabilise the simulation.

In conclusion, in spite of the numerical problems above mentioned, we are convinced that this approach is the most physically consistent one because based on a direct SPH discretisation of the exact Navier-Stokes friction stress tensor (without introducing artificial terms) and therefore we will adopt it in the following when dealing with Newtonian flows.

At this point, it is instructive to present the most commonly adopted solution, historically suggested by Gingold and Monaghan [15] and consisting in the introduction of a completely *artificial viscosity* term in the momentum equation acting only when shocks are present and smearing out the discontinuities, mimicking in some way a physical mechanism. The artificial viscosity is actually build up by two contributions: one linearly proportional to the divergence of velocity and another one substantially analogous to the Von Neumann-Richtmeyer viscosity [41] able to handle high Mach number flows. This artificial viscosity Π_{ij} , which creates a force on particle i in the presence of particle j as explicitly stated by Eq. 2.48 below, reads

$$\Pi_{ij} = \begin{cases} (-\alpha \bar{c}_{ij} \mu_{ij} + \beta \mu_{ij}^2) / \bar{\rho}_{ij} & , \quad V_{ij}^\alpha x_{ij}^\alpha < 0 \\ 0 & , \quad V_{ij}^\alpha x_{ij}^\alpha \geq 0 \end{cases} , \quad (2.41)$$

where the abbreviations

$$\begin{aligned} \bar{\rho}_{ij} &\equiv (\rho_i + \rho_j) / 2, & \bar{c}_{ij} &\equiv (c_i + c_j) / 2, \\ V_{ij}^\alpha &\equiv V_i^\alpha - V_j^\alpha, & x_{ij}^\alpha &\equiv x_i^\alpha - x_j^\alpha, \end{aligned} \quad (2.42)$$

and

$$\mu_{ij} \equiv \frac{h V_{ij}^\alpha x_{ij}^\alpha}{V_{ij}^\alpha V_{ij}^\alpha + 0.01 h^2}, \quad (2.43)$$

were used. Here c_i represents the speed of sound associated with the i -th particle. The parameters α and β are arbitrary, but Monaghan suggested to choose their values

approximately equal to 1 for best results. The term $0.01 h^2$ is introduced in order to prevent singularities when two particles come too close. This viscosity is incorporated in the momentum equation in the following way

$$\frac{dV_i^\alpha}{dt} = \sum_j m_j \left(\frac{p_i}{\rho_i^2} + \frac{p_j}{\rho_j^2} + \Pi_{ij} \right) \nabla_i^\alpha W_{ij}, \quad (2.44)$$

Although numerical results have been obtained which are in good agreement with experimental observations of flows with complex topologies [17], it has also been noted that for simple test cases, where analytical solutions and/or previous exact calculations are available, this term produces inaccuracies in the velocity profiles. These are actually due to an excessive shear viscosity giving a too large vorticity decay and unphysical transfer of momentum. Several ways to escape this difficulty have been proposed as, for example, another form of the viscosity term which takes into account also the vorticity associated with every particle, thus assuring the artificial viscosity to vanish in pure shear flows [42]. Other switches are based on the definition of a further viscosity parameter associated to a source-decay equation causing increasing and decaying of this parameter respectively in an entering and outgoing shock [43].

Finally, it should be also pointed out that this formulation for the dissipation does not allow to know *a priori* the exact viscosity of the simulated fluid, while for the direct discretisation of the friction stress tensor it represents a simple input parameter. In the following, if not explicitly remarked, the above mentioned discretisation of stress tensor based on the nested summation approach will be used for the Newtonian case.

2.5 The kernel function

Until now, we did not specify the kernel function but only discussed the main properties which it should possess. In this section we want to discuss different forms for it all satisfying the previous requirements. One of the simplest choice is that one adopted by Takeda et al. [16], in the simulation of viscous compressible flows, and corresponding to use a simple *Gaussian function* which has best stability properties, and is infinitely differentiable:

$$W(\mathbf{r}, h) = w_0 \exp^{-(r/h)^2}, \quad (2.45)$$

where $w_0 = 1/(2\pi h^2)$ in 2D. The main problem of this kernel is that it has no compact support. This is a severe deficiency because it is not possible to use acceleration techniques like linked lists [35] and the contribution of every particles must be taken into account in the evaluation of the force and not only that one of few first neighbours. The resulting algorithmic complexity is of the order N^2 , where N is the number of particles.

It seems therefore reasonable to take a kernel which unifies a computational efficiency with good smoothing properties. The most frequently used kernel is the *cubic spline kernel* with

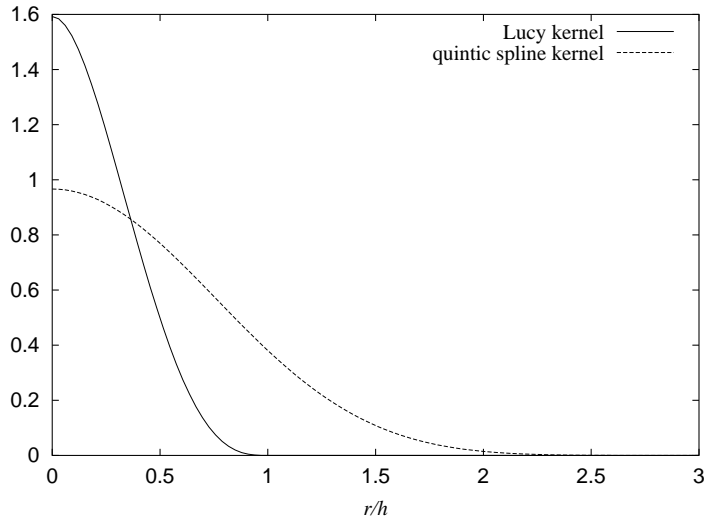


Figure 2.1: Lucy kernel vs. quintic spline kernel. Both kernels interpolates at second order in h . Nevertheless the Lucy kernel has only two continuous derivatives while for the quintic spline kernel the first five ones are continuous. This assures better stability properties, but with an increasing computational cost, since the region of contributing neighbours is larger.

$$W(\mathbf{r}, h) = w_0 \begin{cases} 1 - \frac{3}{2}(r/h)^2 + \frac{3}{4}(r/h)^3 & , \quad 0 \leq r/h < 1 \\ \frac{1}{4}(2 - r/h)^3 & , \quad 1 \leq r/h < 2 \\ 0 & , \quad r/h \geq 2, \end{cases}$$

where w_0 is a normalisation factor which in two dimensions, for example, takes the value $10/(7\pi h^2)$. The advantage of this particular kernel is that it has compact support, is spherically symmetric, the leading order term is $O(h^2)$, and the first and second derivatives are continuous. Nevertheless, it has been often pointed out that such low-differentiable kernels with compact support are unstable to transverse modes. These kind of instability can be reduced when using higher-differentiable kernels characterised by a smoother second derivative. This property assures that the kernel is not too sensitive of particle disorder and the errors present in the summation estimate are small provided that the number of neighbours per particle does not fluctuates too much. A possible choice is the *quintic spline kernel* which reads

$$W(\mathbf{r}, h) = w_0 \begin{cases} (3 - r/h)^5 - 6(2 - r/h)^5 + 15(1 - r/h)^5 & , \quad 0 \leq r/h < 1 \\ (3 - r/h)^5 - 6(2 - r/h)^5 & , \quad 1 \leq r/h < 2 \\ (3 - r/h)^5 & , \quad 2 \leq r/h < 3 \\ 0 & , \quad r/h \geq 3, \end{cases}$$

where $w_0 = 7/(478\pi h^2)$. This kernel has the first four derivatives continuous. Although, it requires a computational effort bigger than for lower-differentiable kernels, it has shown to be much more stable in simulations of quasi-incompressible flows involving

very low Reynolds number. In that case, the cubic spline kernel produces very noisy hydrodynamics fields.

Higher-order kernels have been also proposed which interpolate more accurately in space, for example the *super-Gaussian kernel* (dominant error $O(h^4)$), but they possess disadvantages such as expensive computational performance, or they become locally negative in some parts of the domain. This introduces conceptual difficulties in order to describe positive-definite hydrodynamics field, i.e. mass density. A detailed discussion can be found in [44].

In most of the present work, we choose for the kernel the *Lucy weighting function* originally introduced by Lucy and Monaghan in the first SPH papers [15] and more recently used in problems dealing with ideal gases [45, 46], i.e., we employ

$$W(\mathbf{r}, h) = w_0 \begin{cases} (1 + 3r/h)(1 - r/h)^3 & , \quad r/h < 1 \\ 0 & , \quad r/h \geq 1 \end{cases} \quad (2.46)$$

where $w_0 = 5/(\pi h^2)$ in 2D. It interpolates at second order in h , has a compact support and its first and second derivatives are continuous, cf. Fig. 2.1.

2.6 Boundary conditions

Until now we discussed the SPH equations which must be solved in a bulk fluid disregarding what happens at the boundaries. From a numerical point of view, boundaries must be always specified, not only for problems defined on bounded domains, but also for bulk fluids. In the last case, the finite availability of memory and CPU-time limits the size of the simulated systems and force us to use a finite number of elements (i.e. SPH particles) to discretize the physical problem. As a consequence, suitably boundary conditions must be imposed which eliminate unwanted surface effects.

In this section we will present the common implementation of boundary conditions first for a bulk fluid (unbounded domain) and, secondly, for fluids in confined geometries.

2.6.1 Periodic boundary conditions

The first question which arises when performing numerical simulations of bulk fluids is: “How to deal with boundary conditions for systems defined on an unbounded domain?”. If we simply allow the system to terminate, the particles near the surfaces will experience quite different forces from the particles in the bulk. Unless we want to describe small system (i.e. clusters, drops of liquid), where the finite size play a crucial physical role, this situation is not satisfactory. For simulations of bulk fluids, we must remove the surface effects, if we want to have a consistent homogeneous description of a system extending indefinitely.

This problem can be solved by using the so called *periodic boundary conditions* (PBC) [36]. This approach describes the system via a “primary box”, representing a fixed control volume, which is replicated to infinity by rigid translations in all Cartesian directions. The replicas are called “image boxes” and contain the same sets of particles

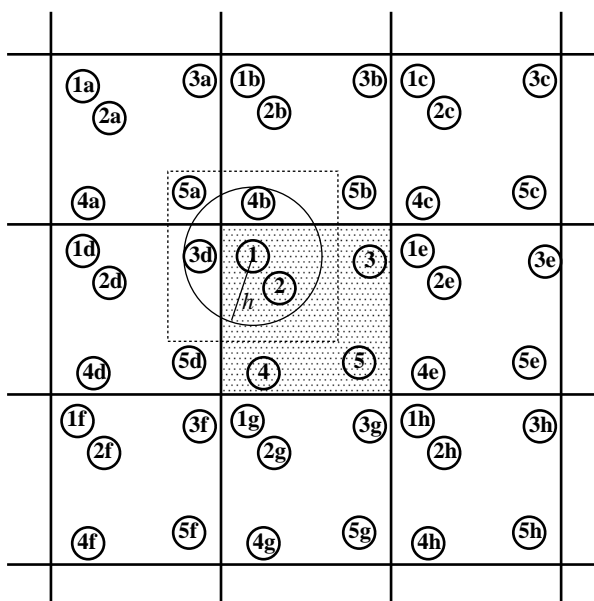


Figure 2.2: Implementation of the PBC: the bulk fluid is simulated only in one *primary box* while the unbounded domain is modelled by periodic replicas of the main box. The particles are allowed to interact with the bulk particles of the same box plus all their *images*. By using short range particle interaction is it possible to use the *minimum image criterium* to reduce the computational effort. That is, particle 1, for example, will not interact with all its images but only with those ones lying within a box of size L , with $L > h$.

as that simulated in the primary box, fig. 5.10. As a particle is evolved in the central box, all its periodic images will move through the infinite domain in the exact the same way. Therefore we need to take into account only a finite number N of sampling particles. The key point is that every simulated particle does not interact only with its neighbours in the primary box but also with all its “image particles” in the nearby boxes: this allow us to eliminate unwanted surface effects. On the other hand, the price to pay is the introduction of an artificial periodicity in the simulated system which restricts the numerical study to short range and short-time phenomena (comparable with the size of the box). In spite of this, the numerical experience shows that PBC have a little effect on global equilibrium properties when considering short-range particle interactions.

Let us start giving some details on the PBC implementation. As already mentioned, only the particle in the primary box need to be simulated, while all the other images are replicated over the domain. Attention must be paid when a particle crosses the border and leaves the primary box. In that case, an image will simultaneously enter the primary box through the opposite face. Numerically, we remove the simulated particle which has gone out and replace it with an other particle (with equal momentum) places symmetrically at the opposite face. This approach conserves automatically the total particle number and momentum of the bulk system.

For what concerning interactions, it could seems that, by implementing PBC, the

number of interacting pairs should increase enormously. In practice, if we deal with short-range forces, we can optimise the algorithm by using the so called *periodic image criterium* and no additional complexity is introduced in the code. The main idea is the following one: assumed that the interaction range h is less than the size of the box L , the particle in the primary box does not interact with all its possible images but only with those ones whose centre lies within a box of edge L centred on the particle location. As shown in fig. 5.10, the SPH particle labelled with $i = 1$ in the primary box, will interact only with the particle 2 in the same box and with the image particles 4b and 3d in the remaining domain.

This permits to reduce the computational effort to $(1/2)N(N-1)$ where N is the number of simulated particles in the main box. This squared dependence over N represents still a potential bottleneck for the program, but it can be easily removed considering linked cell algorithms as those described in [36]

2.6.2 Rigid boundary conditions

Solid boundary conditions represent a crucial point in SPH. Many possible approaches have been addressed in the last years. One may consider fixed boundary particles lying at the wall surfaces and interacting with the SPH bulk particles via an artificial repulsive force which prevents penetration. Problems arise if particle density has to be evaluated near the wall: as already mentioned in the previous section, if we consider just one layer of equispaced boundary particles, the density of those particles approaching the surface will decrease rapidly to an approximatively half value of that one into the domain. This is because, for a particle just on the surface, only the half sphere intersecting the inner domain is taken into account in the average process, while the remaining particle-volume lying outside does not contribute. This causes a gradient of density and consequently, via Eq. 2.35, a strongly deeper gradient of pressure in the momentum equation which forces the particle to accelerate towards the wall producing loss of homogeneity in the dynamical grid and artificial layers parallel to the surface. One possible way to escape this difficulty is to evaluate the density via the continuity equation and not like a summation over neighbouring particles. In this calculation, only one layer of boundary particles is involved, which does not contribute to the quantities estimated in the inner domain, see fig. 2.3. This permit to eliminate the artificial pressure force due to the gradient of density near the wall [17]. Nevertheless, it introduces other problems related to a consistent evaluation of other hydrodynamics field in the boundary layers, i.e. velocity field evaluation for moving boundary conditions.

Some other alternatives have been proposed in the literature: one possibility is to evaluate the contribute of a gas of *imaginary particles* supposed existing outside the domain. As already mentioned in section 2.1, the derivation of the integral SPH equations is exact until a distance of order $h/2$ apart from the walls. In the vicinity of the solid boundaries, the surface terms present in Eq. (2.16) must be taken into account. In the Takeda's approach [16], such surface terms are evaluated analytically assuming a homogeneous continuum distribution of SPH particles outside the domain. This is actually the best approach, because it is exact SPH in the continuum limit (no artificial assumption are considered but only SPH interaction are used) and does not involve ex-

ternal particles. On the other hand, although good results have been obtained in simple cases, complicated surface integrals must be solved when we have to deal with complex geometries.

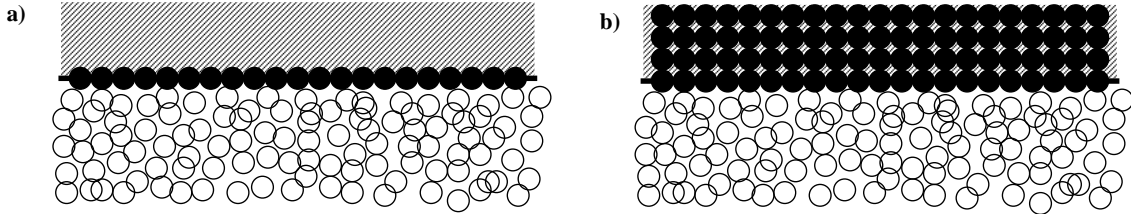


Figure 2.3: Two possible implementation of rigid boundary conditions: a) a unique layer of boundary particle (black circles) non-entering in the interpolation process for the bulk properties and interacting with the fluid particle (white circles) via LJ plus artificial viscous forces. b) the outside region is filled (until a distance of order h) with boundary particle which enter in the calculation of bulk quantities.

Another approach is to consider the contribution of a gas of *mirror boundary particles*, which are created outside the domain simply by reflecting fluid particles across the boundary with opposite velocities [19, 20, 21, 37]. Once more, although this approach has been shown useful for modelling simple channel flows, it introduces numerical errors when dealing with curved solid surfaces. A better procedure is that one due to Morris [42] and consisting to fill the exterior (at least a range of depth comparable with the support h of the weight function) with *image boundary particles* which reproduce the desired internal averaged density and to consider also these ones entering in the evaluation process of averaged quantities, fig. 2.3. The difference with the previous method lies in the estimate of the velocities for the boundary particles. In this case, for every fluid particles i a normal distance d_i to the solid surface is defined. This is used to evaluate a tangent plane to the surface, and consequently the normal distance d_j to this plane for a selected boundary particle j . Finally, the velocity \mathbf{V}_j is extrapolated across the tangent plane assuming zero velocity on it: $\mathbf{V}_j = -(d_j/d_i)\mathbf{V}_i$. This approach permit to handle solid surfaces whose curvature radius is not too small.

In this work, we tested three of the strategies mentioned above. In particular, we considered: A) one single layer of boundary particles non-entering in the interpolation process for the evaluation of the bulk quantities and interacting with the bulk particles simply via suitable artificial forces, responsible of the impenetrability and no-slip condition at the wall; B) a thick region filled, until a distance $h/2$ apart from the wall, with equispaced boundary particles, which are now characterised by fluid variables (mass density, velocity, stress) and interacting with the bulk particles hydrodynamically (via SPH equations) as well as via the artificial forces already considered (see fig. 2.3); C) a thick region filled with equispaced *image* boundary particles interacting with the bulk particles hydrodynamically and characterised by artificial fluid variables ensuring the correct interpolated conditions at the solid interface.

Usually, the first method is employed in conjunction with the evaluation of the mass density via the continuity equation (2.31), in such a way to remove the artificial wall

effects described at the beginning of this section. Inversely, the second approach can be implemented with the usual evaluation of density based on eq. (2.29), provided that the distribution of boundary particles reproduce the correct bulk density.

As already mentioned, in order to enforce incompentetrability and no-slip at the wall special forces are considered in both cases. In particular the following repulsive Lennard-Jones like force vector is adopted

$$f_{\text{wall}}^{\alpha}(r) \propto \begin{cases} [(r_0/r)^4 - (r_0/r)^2] r^{-2} r_{\alpha} & , \quad r \leq r_0 \\ 0_{\alpha} & , \quad r > r_0 \end{cases}, \quad (2.47)$$

which prevents particles to cross the border via adjustment of a (in any other respect unimportant) proportionality factor in (2.47). In order to consider no-slip boundary conditions, just for particles approaching the wall (whose distance from the boundary is less than the cutoff radius in the Lucy function) we take into account a viscous force based on the artificial viscosity already introduced. This term introduce a repulsive interaction which push the bulk particles forcing them to assume the same velocity of the boundary ones. With an appropriate choice of the parameters α and β appearing in Eq. (2.41), we can obtain an exact zero velocity at the wall or, alternatively, suitable slips as experimentally observed in several microscopic flows. Therefore, the final form for the boundary contribute to the force, which should be added to eq. (5.7), reads

$$F_{\text{ext},i}^{\alpha} = - \sum_j (m_j \Pi_{ij} \nabla_i^{\alpha} W_{ij} + f_{\text{wall},ij}^{\alpha}), \quad (2.48)$$

with Π from (2.41), and where the term appearing in the sum represents now the effect of the j -th boundary particle to the i -th bulk particle. As already pointed out, this approach is consistent with the fact that we are going to solve the physical conservation equations in the inner domain as far as a distance of order $h/2$ (h : smooth cutoff radius) apart from the boundary. In this thin area artificial terms are included in the exact discretized SPH bulk equations in order to take into account wall effects.

A brief discussion on the two forms of boundary conditions presented above is in order. Although both of them solve the problem of density evaluation near the walls, none enable to discretize the gradients of velocity field in a satisfactory way. Indeed, the absence of boundary particles in the first case, or the impositions of an arbitrary velocity field on the external domain in the second one, introduce inconsistencies or inaccurate interpolations at the border. This problem can be however remedied by suitable choice of the parameters α and β entering in (2.41), and forcing the system, in some sense “against its will”, to assume the correct behaviour. Concerning advantage of one formulation upon the other one, the second approach was found to be numerically more stable and accurate, specially for problems involving moving boundaries therefore, if not explicitly stated, we will adopt it in the following.

As last remark, we should point out that this treatment of the boundary conditions should be replaced with other approaches, i.e. image particles [42] or, whenever feasible, the Takeda’s one [16], if accurate estimate of the hydrodynamics fields are needed in the vicinity of the walls, i.e. high Reynolds number problems involving very thin boundary layers.

2.7 Time integration

We adopt a simple two-step predictor-corrector (P-C) scheme with 2nd order accuracy in time to calculate the evolution of the independent variables. It should be replaced if higher precision is essential. In the following, the superscript indicates the discrete time step. Actually, the P-C scheme consists in an Eulerian explicit first evaluation of all quantities (predictor step):

$$\begin{aligned}\tilde{x}_\alpha^{n+1} &= x_\alpha^n + V_\alpha^n \frac{\Delta t}{2} \\ \tilde{V}_\alpha^{n+1} &= V_\alpha^n + F_\alpha^n \frac{\Delta t}{2} \\ \tilde{\rho}^{n+1} &= \rho^n + G^n \frac{\Delta t}{2}\end{aligned}\tag{2.49}$$

where F and G are the sources evaluated as follows $G^n = G(\rho^n, V_\alpha^n)$, $F_\alpha^n = F_\alpha(\rho^n, V_\alpha^n)$ and we are considering the density ρ as an independent variable evolved via the continuity equation (2.31). Alternatively, if eq. (2.29) is used, a pre-loop over all the particles is necessary to determine the density before to calculate the source terms: this approach requires extra CPU-time but has the remarkable advantage to conserve exactly the mass.

Once we obtained the predicted values of all the independent variables (for every particle) we evaluate the source over these states in order to calculate the final corrected variables. This step involves the calculation of the following quantities as summation over all the particles: $\tilde{G}^{n+1} \equiv G(\tilde{\rho}^{n+1}, \tilde{V}_\alpha^{n+1})$ and $\tilde{F}_\alpha^{n+1} \equiv F_\alpha(\tilde{\rho}^{n+1}, \tilde{V}_\alpha^{n+1})$. It must be pointed out that this part of the algorithm is the most CPU-time requiring if fast searching neighbours routines (described in the previous section) are not employed. The final corrected quantities read therefore

$$\begin{aligned}X_\alpha^{n+1} &= X_\alpha^n + (V_\alpha^n + \tilde{V}_\alpha^{n+1}) \frac{\Delta t}{2}, \\ V_\alpha^{n+1} &= V_\alpha^n + (F_\alpha^n + \tilde{F}_\alpha^{n+1}) \frac{\Delta t}{2}, \\ \rho_\alpha^{n+1} &= \rho_\alpha^n + (G^n + \tilde{G}^{n+1}) \frac{\Delta t}{2},\end{aligned}\tag{2.50}$$

where the source terms appearing in the previous integration equations are obtained by a summation of contributions over the SPH particles. For example, the term $F_\alpha^n(x_i)$ – evaluated on the position of the particle i – is obtained by a summation process like the one given by Eq. 2.48. This form is valid only in the bulk part of the fluid, while for particles approaching the boundaries the previous source term (2.48) is supplemented by an expression involving the L-J like force (2.47) and the contribution due to the artificial pressure, Eqs. 2.41-2.43, in order to enforce the incompressibility and no-slip condition at the wall. For the stability condition, it should be sufficient to accommodate a Courant-Friedrichs-Lewy [47] condition which actually makes sure that there is no numerical propagation of signals faster than the speed of sound c_0 , i.e., for the time step we require $\Delta t \leq h/c_0$. In addition, we consider also a condition on the forces acting on

any particle. This should be also satisfied in order to ensure a correct, safe integration: $\Delta t \leq \min_{\forall i} (h/|F_{\alpha}^i|)$.

2.8 Numerical tests: the incompressible Newtonian flow

In this section we want to validate the SPH algorithm in the simple Newtonian case. We will present some numerical results for the transient flow in a 2D channel flow geometries. We use a square simulation box where the fluid particle are immersed and interacting each other hydrodynamically via the SPH equation.

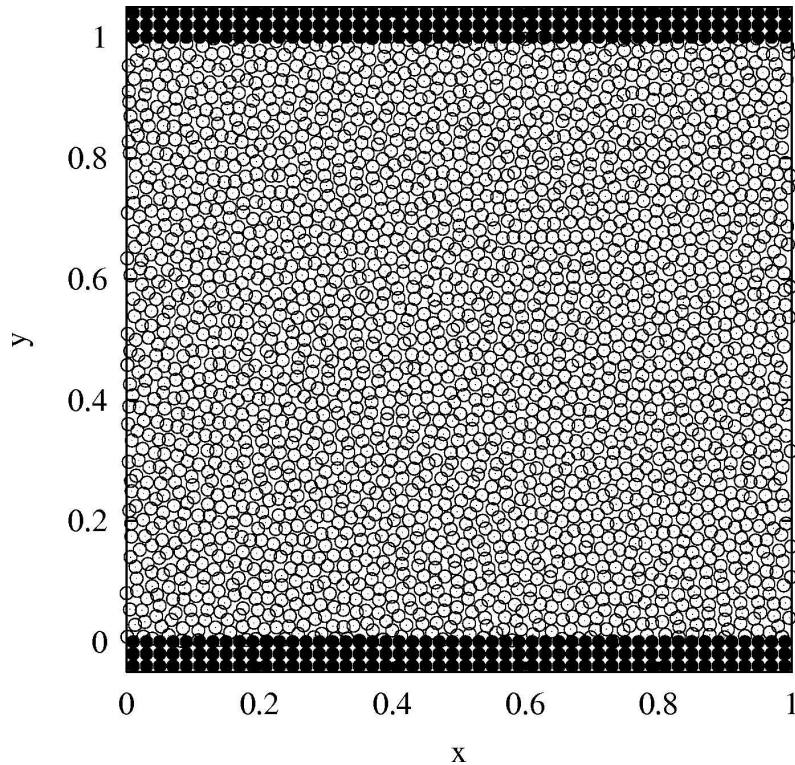


Figure 2.4: SPH bulk particle (white) and fixed boundary particles (black). A total number of 2500 particles were used. Periodic boundary condition have been imposed in the x -direction with particle outgoing from the right side, re-inserted on the left side with the same velocity and y -coordinate. It should be pointed out that in this picture the particle radius has been chosen for pure illustrative purpose and does not correspond to the real quantity $h = 0.05$ used for the numerical calculations.

In addition, boundary conditions must be imposed for the consider channel flow problem. In order to describe this, we consider rigid boundary conditions at the upper and lower plate, which consist of a thick region filled with boundary particles entering in the interpolation process and interacting with the fluid particles via the LJ-forces plus a further artificial viscosity pressure in order to enforce the no-slip condition at the

wall, Eq. (2.48). On the other hand, periodic boundary conditions, as described in sec. 2.6.1, will be implemented in the x -direction (parallel to the plates) in order to model an infinitely extended fluid. Fig. 2.4 shows the typical SPH geometry, with boundary particles marked with black circles.

2.8.1 Couette flow

The geometry of the problem is showed in fig.2.5 and consists of a flow between two infinite parallel plates, whose distance is L_0 . At the initial time $t = 0$ the fluid is at rest and for $t > 0$ the upper plate is moved suddenly with constant velocity V_0 in the y -direction.

The problem considered here is isothermal, therefore we do not need to take into account an equation for the internal energy. We evaluate the density via the summation in (2.29) and the momentum equation (5.7), for the velocity field coupled with the external contribution due to the boundaries. Concerning constitutive relations, we employ the equation of state (2.35) for the pressure, while dissipation is taken into account via a direct discretisation of (2.40) based on the nested summation approach.

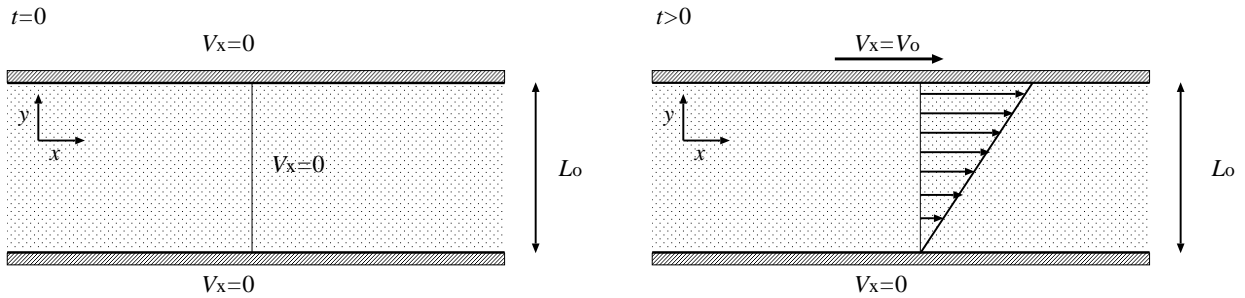


Figure 2.5: Geometry for the Couette problem. Initially the fluid is at rest and at time $t > 0$ the upper plate start to move with constant velocity V_0 . At steady state the usual linear velocity profile for $V_x(y)$ is achieved.

Numerically, in order to do quantitative analysis, it is necessary to make the equations dimensionless [49]. We introduce therefore the following dimensionless variables (denoted by a superscript *):

$$X^{\alpha*} = \frac{X^\alpha}{L_0}, \quad V^{\alpha*} = \frac{V^\alpha}{V_0}, \quad p^* = \frac{p}{p_0}, \quad \rho^* = \frac{\rho}{\rho_0}, \quad \sigma^{\alpha\beta*} = \frac{\sigma^{\alpha\beta}}{\sigma_0}, \quad (2.51)$$

where L_0 , V_0 , ρ_0 , p_0 and σ_0 are, respectively, reference quantities for length, velocity, mass density, pressure and friction stress. The reference time is automatically defined $t_0 = L_0/V_0$. Let us consider now the expression for the friction stress tensor appearing in Eq. (2.40). In the case of incompressible flow the divergence of the velocity field $\nabla^\alpha V^\alpha$ is approximatively zero and $\sigma^{\alpha\beta} = \eta (\nabla^\alpha V^\beta + \nabla^\beta V^\alpha)$. Therefore we choose as reference value for the friction pressure $\sigma_0 = \eta V_0/L_0$. In addition, we assume that $p_0 \alpha_0^2 =$

$(1/2)\rho_0 c_o^2$, which is consistent with the definition of speed of sound $c_o = (\sqrt{\partial p / \partial \rho})_{\rho=\rho_0}$. The dimensionless momentum equation can be finally cast in the following form

$$\frac{dV^\alpha}{dt} = -\frac{1}{2M^2} \frac{\nabla^\alpha p}{\rho} + \frac{1}{Re} \nabla^\beta \sigma^{\alpha\beta}, \quad (2.52)$$

where all the variable are now made dimensionless and for the sake of simplicity we omitted the superscript $*$. Let us notice that the only two free parameter characterizing the problem (resulting from the coupling between all the reference quantities) are the *Mach number* and the *Reynolds number* defined in the following way

$$M = \frac{V_0}{c_o}, \quad Re = \frac{\rho_0 L_0 V_0}{\eta}. \quad (2.53)$$

The Mach number quantifies the effects due to the propagation of sound waves (for compressible flows) in comparisons with a typical velocity which characterises our problem. As already mentioned, quasi-incompressible flows are described by a very small Mach number ($M \lesssim 0.1$), while Mach numbers comparable or larger than 1 describe respectively transonic and supersonic flows, which we will not discuss in the present work. The Reynolds number Re is a measure of the inertial forces present in the fluid over the viscous ones. High values of Re are commonly chosen to simulate turbulent flow, while $Re \lesssim 10$ usually characterise laminar flows.

A time-dependent solution for the start-up of this flow, written in dimensionless form, is found to be:

$$V_x(y, t) = y + \sum_{n=1}^{\infty} \frac{2}{n\pi} (-1)^n \sin(n\pi y) \exp\left(-\frac{n^2\pi^2}{Re} t\right), \quad (2.54)$$

where V_x is the x -component of the velocity field parallel to the plates. If V_y is assumed to be initially zero, than $V_y = 0$ for every $t > 0$.

As already mentioned in section 2.4, we use a quasi-incompressible equation of state characterised by a speed of sound c_o 10 times bigger than the typical flow velocity V_0 : this gives a Mach number $M = 0.1$ and keeps density fluctuations under 1%. The dynamic viscosity ν is properly chosen in order to have a Reynolds number $Re = 1$, while the bulk viscosity ζ is set here to zero. The boundary particles which lie on the upper plate are moved at time $t = 0$ with constant velocity, while the bottom plate is maintained fixed. We compared the results of the SPH simulation with the analytical solution, Eq. (2.54), at many different time: $t = 0.01, 0.05, 0.1, 0.2, 0.3$. In the present simulation we used 2200 bulk particles and 300 boundary particles initially placed on a square grid. The interpolating function used here is the Lucy kernel with a cutoff radius $h = 0.05$. This choice involves approximately 20 neighbours for every SPH particle. The time step chosen was $\Delta t = 0.0001$. Figure 2.6 shows a very good agreement, confirming that SPH can handle non-stationary problems with high accuracy. The Couette problem is a good working-test also for boundary conditions. In fact, the no-slip conditions is satisfied not only at the fixed plate, where V_x is zero, but also at the upper moving plate where it assumes the correct wall velocity V_0 as expected.

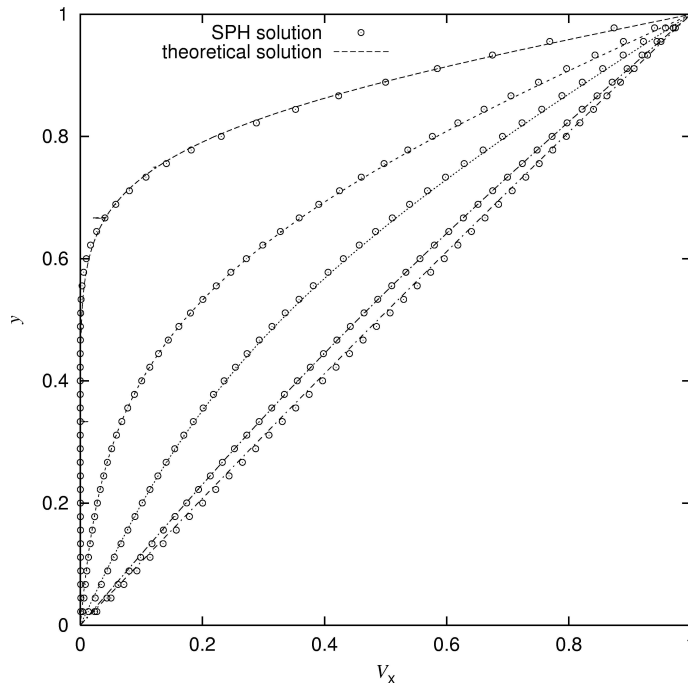


Figure 2.6: Comparisons between the analytical solutions and the numerical SPH results. The velocity profiles were extracted at different times $t = 0.01, 0.05, 0.1, 0.2, 0.3$ and show a very good agreement with the predicted curves. The dimensionless parameters used were $M = 0.1$ and $Re = 1.0$.

2.8.2 Poiseuille flow

The Poiseuille problem consists of a fluid between two fixed plate placed at $y = 0$ and $y = 1$. Initially the fluid is at rest while for $t > 0$ a volume force F is acting parallel to the x -direction, see fig. 2.8.2.

The Navier-Stokes equation for this problem, written in dimensionless form, corresponds to eq. (2.52) except for an additional body-force contribution F which drives the fluid

$$\frac{dV^\alpha}{dt} = -\frac{1}{2M^2} \frac{\nabla^\alpha p}{\rho} + \frac{1}{Re} \nabla^\beta \sigma^{\alpha\beta} + F, \quad (2.55)$$

where we have still to define M and Re . The previous expressions given in eq. (2.56) are evidently not applicable to this flow, indeed the reference values for the velocity V_0 can not be specified *a priori* for this problem. Nevertheless, we can construct two dimensionless numbers by considering a reference value F_0 for the body force. In this case the dimensionless parameters characterizing our flow are

$$M = \frac{\sqrt{F_0 L_0}}{c_o}, \quad Re = \frac{\rho_0 \sqrt{F_0 L_0^3}}{\eta}. \quad (2.56)$$

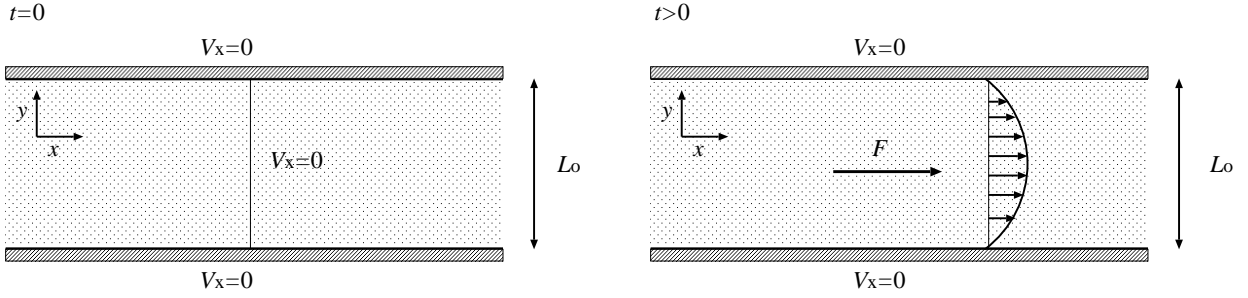


Figure 2.7: Geometry for the Poiseuille flow problem.

As in the Couette problem, a solution in series can be found which reads

$$V_x(y, t) = \frac{Re}{2}y(y-1) + \sum_{n=0}^{\infty} \frac{4Re}{\pi^3(2n+1)^3} \sin(\pi y(2n+1)) \exp\left(-\frac{(2n+1)^2\pi^2}{Re}t\right), \quad (2.57)$$

which describes the transitory behaviour of the system toward the steady state represented from the well known parabolic velocity profile.

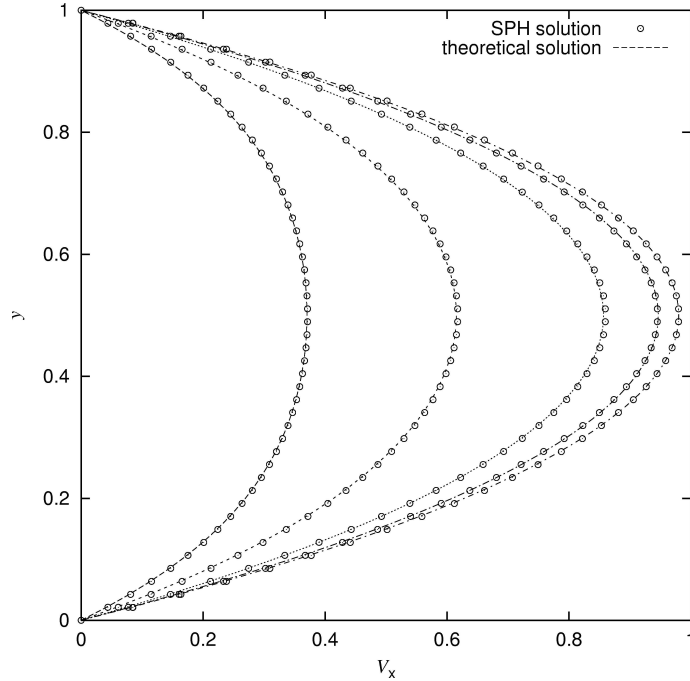


Figure 2.8: Comparisons between the analytical solutions and the numerical SPH results for $M = 0.1$ and $Re = 8.0$. The velocity profiles were extracted at different times $t = 0.05, 0.1, 0.2, 0.3, 0.4$

As in the previous case we, we performed SPH runs with 2500 particles placed as shown in fig. 2.4. Figure 2.8 shows a quantitative comparisons between the numerical

solution and the theoretical one, eq. (2.57), at five different times: $t = 0.05, 0.1, 0.2, 0.3, 0.4$. The free parameters chosen here were $M = 0.1$ and $Re = 8.0$.

Chapter 3

Smoothed Particle Dynamics for viscoelastic flows

In this chapter a viscoelastic numerical scheme based on Smoothed Particle Dynamics, which goes a step beyond the Smoothed Particle Hydrodynamics method (SPH) discussed in the previous chapter, is presented. The formalism describing viscoelasticity is introduced in the ordinary conservation laws by a differential constitutive equation for the anisotropic part of the stress tensor [50]. For illustrative purpose we choose the non-linear Jaumann-Maxwell (i.e. corotational Maxwell) model, which in turn is obtained by replacing the partial derivative appearing in the linear Maxwell model with a Jaumann derivative which contains a nonlinear advective term plus a term which takes into account solid-body rotations. Some remarks should be done on this particular choice. It is widely acknowledged that such a model, although exhibiting typical non-Newtonian effects like shear-dependent viscosity and presence of normal stress differences, it does not represent an adequate approach for quantitative comparisons with real viscoelastic flows [7, 6]. In particular, some anomalies in the behaviour of the shear stress coupled with an excessive shear thinning at large shear rates are not consistent with experimental observations in polymeric fluids. Nevertheless, the same properties above mentioned, showing very complex non-linear behaviours, test severely the resulting numerical implementation of the model. It is not the goal of the present investigation to study whether or not our choice of the constitutive equation give realistic results, rather, assumed the validity of the model, to develop a stable, accurate and consistent numerical algorithm for it. As it will be clear later, more realistic constitutive equations can be used with only minor modifications in the coding.

The scheme of the chapter is the following one: in Sec. 3.1 we present rigorously the Jaumann-Maxwell model used in this work, discussing the way to discretize it numerically in the SPH formalism, its consistency and proper dimensional analysis. After that, in Sec. 3.2, some numerical results are discussed for unsteady relaxation processes of an initial sinusoidal velocity profile, since an analytic reference solution is readily available in that particular non-equilibrium problem. Sec. 3.4 deals with the problem of bulk steady shear-flow: here a rheological study in the elastic parameter will be presented and compared with theoretical results. Finally, in Sec. 3.5 we apply the method described

above to the specific problem of shear flow of a viscoelastic matrix contaminated with rigid non-rotating inclusions. Since this is a severe test for the numerical algorithm, we compare first our results in the case of a Newtonian matrix where analytical solutions are recoverable, secondly we focus on the J-M viscoelastic model, showing the effect of the presence of such inclusions on global material properties and discussing local features of its resulting flow dynamics.

3.1 The constitutive equation

In this section we will describe in details the constitutive model which we chose for the implementation in the SPH algorithm. As already discussed, the set of hydrodynamics conservation equations given in sec. 2.2, (2.10,2.21,2.30), must be suitably closed. This has been done in the previous chapter dealing with simple Newtonian flows. In that case a standard Newtonian constitutive relation has been adopted to model the friction stress tensor.

In analogy with the formalism already introduced, it is possible describe the general symmetric stress tensor $P^{\alpha\beta}$ by splitting it into an isotropic plus an anisotropic part, cf. eq.(2.39). For the sake of clarity we rewrite it here again

$$P^{\alpha\beta} = -(p - \sigma)\delta^{\alpha\beta} + \overline{\sigma}^{\alpha\beta}. \quad (3.1)$$

where $p - \sigma$ is the total pressure (hydrostatic and friction term) responsible of volumetric changes, while $\overline{\sigma}^{\alpha\beta}$ is the deviatoric traceless tensor related to shape deformations preserving volumes.

A closure relation for p in (4.65) is given from an equation of state relating hydrostatic pressure to local density. We will adopt the equations of state defined in (2.34) and (4.66), depending on the particular application. In any case, both of them will be characterised by large values of the speed of sound in order to simulate incompressible flows: this was the already mentioned hypothesis of *quasi-incompressibility*. Concerning the dynamic pressure σ , we will neglect it in the following by assuming a zero bulk viscosity.

3.1.1 The corotational Maxwell model

In order to describe shear and extensional deformations we propose tentatively a non-linear corotational Maxwell model for the components of the anisotropic stress tensor $\overline{\sigma}$ [4]. As already mentioned in the previous section, Maxwell-like models does not exhibit theoretical behaviours which can be useful for a realistic modelling of practical problems. Despite their inability to describe quantitatively real complex fluids, they have been widely used in numerical calculations because their relative simplicity which make them understandable but at the same time able to reproduce, at least qualitatively, many macroscopic viscoelastic phenomena. The model used in this work is chosen for purely illustrative purpose, and have been used in a limited number of applications [19, 20, 21]. Nevertheless, as it will be clear at the end of the section, the SPH

discretisation of this equation assumes a very general form, which allows for changes and adaptations to more 'realistic' constitutive equations with only minor modifications of the algorithm.

Let us start by defining the symmetric strain rate tensor as follows

$$\dot{\epsilon}^{\alpha\beta} = \frac{1}{2} \left(\frac{\partial V^\beta}{\partial x^\alpha} + \frac{\partial V^\alpha}{\partial x^\beta} \right). \quad (3.2)$$

This tensor characterises the local total deformation (shape and volume) of the material. On the other hand, changes in volume are controlled in our scheme uniquely from the equation of state, while the constitutive Maxwell equation describes separately the deviatoric strain rate tensor which is by definition the traceless part of symmetric strain rate tensor, i.e.,

$$\dot{\bar{\epsilon}}^{\alpha\beta} \equiv \dot{\epsilon}^{\alpha\beta} - \frac{1}{d} \delta^{\alpha\beta} \dot{\epsilon}^{\gamma\gamma} = \dot{\epsilon}^{\alpha\beta} - \frac{1}{d} \frac{\partial V^\gamma}{\partial x^\gamma} \delta^{\alpha\beta}, \quad (3.3)$$

where d is the dimensionality of the problem. The corotational Maxwell model [4] relates at this point locally the deviatoric stress to deviatoric strain rate in the following way

$$\frac{d}{dt} \bar{\sigma}^{\alpha\beta} + \bar{\sigma}^{\alpha\gamma} \omega^{\gamma\beta} + \bar{\sigma}^{\gamma\beta} \omega^{\alpha\gamma} = \frac{2\eta}{\lambda} \dot{\bar{\epsilon}}^{\alpha\beta} - \frac{1}{\lambda} \bar{\sigma}^{\alpha\beta}, \quad (3.4)$$

where λ is the viscoelastic relaxation time, η is the viscosity of the specimen and the lhs of (4.70) is the so called *Jaumann temporal derivative* of $\bar{\sigma}$ which describes the time evolution of a fixed volume in a Lagrangian way and subjected to rotations, and $\omega^{\alpha\beta}$ is the vorticity tensor defined as

$$\omega^{\alpha\beta} \equiv \frac{1}{2} \left(\frac{\partial V_\beta}{\partial x_\alpha} - \frac{\partial V_\alpha}{\partial x_\beta} \right). \quad (3.5)$$

Finally, the SPH model equations for the stress tensor are obtained, from (4.70), in the same way as those ones for momentum or mass conservation giving

$$\begin{aligned} \frac{d}{dt} \bar{\sigma}_i^{\alpha\beta} &= \bar{\sigma}_i^{\alpha\gamma} (k_i^{\gamma\beta} - k_i^{\beta\gamma}) + \bar{\sigma}_i^{\gamma\beta} (k_i^{\alpha\gamma} - k_i^{\gamma\alpha}) - \frac{1}{\lambda} \bar{\sigma}_i^{\alpha\beta} \\ &\quad + \frac{2\eta}{\lambda} (k_i^{\alpha\beta} + k_i^{\beta\alpha} - \frac{2}{d} k_i^{\gamma\gamma} \delta^{\alpha\beta}) \end{aligned} \quad (3.6)$$

where the SPH discretisation of the transposed velocity gradient appearing through strain (4.69) and rotation rate (vorticity) tensors, explicitly appearing in (4.72) reads

$$k_i^{\mu\nu} \equiv \frac{1}{2} \left(\frac{\partial V^\mu}{\partial x^\nu} \right)_i \simeq \frac{1}{2} \sum_j \frac{m_j}{\rho_j} (V_j^\mu - V_i^\mu) \frac{\partial W_{ij}}{\partial x^\nu}. \quad (3.7)$$

There are comparable approaches using differential constitutive equations adapted to simulate elasto-plastic materials [19, 20, 21, 22]. In these works, the term due to elasticity in (4.70) remains the same but a further relation, e.g. based on the von Mises criterion, is used to recognise the plastic regime where the stress stays constant.

3.1.2 The limiting case of vanishing elasticity

A brief discussion on the mechanism of dissipation introduced in the momentum equation with (4.70) is in order. Our approach is based on the solution of a further dynamic equation for the stress tensor based on the Maxwell model, in this sense we used the typical mixed stress-velocity-pressure formulation in which the deviatoric stress tensor becomes a primary unknown variable [1]. This choice has a direct implication on the computational requirements of the resulting algorithm. We will come back to this point later.

The key message of this section is that the introduction of dissipation via the Jaumann-Maxwell model is consistent with the definition of the friction stress tensor for the Newtonian case given in the previous chapter (see sec. 2.5). Indeed in our model, the dissipation does not enter in the momentum equation but rather in this constitutive equation via the correspondent time-dependent stress tensor (and the related time-dependent viscosity). Eq. (4.70) is characterised by a typical relaxation time λ which quantifies the time scales on which elastic effects are important or, in other words, the persistence of memory effects in the simulated flow. It is therefore clear that in the limiting case $\lambda \rightarrow 0$, the elastic behaviour is negligible and the lhs term in (4.70) vanishes producing the usual *explicit* constitutive stress-strain relation for Newtonian viscous compressible flows

$$\overline{\sigma}^{\alpha\beta} = 2\eta \dot{\epsilon}^{\alpha\beta} = \eta \left(\frac{\partial V^\alpha}{\partial x^\beta} + \frac{\partial V^\beta}{\partial x^\alpha} \right) - \frac{2}{d} \eta \frac{\partial V^\gamma}{\partial x^\gamma} \delta^{\alpha\beta}. \quad (3.8)$$

analogous to the friction stress tensor given in eq. (2.40) where the bulk viscosity ζ is set here to zero. The viscosity enters therefore implicitly in the momentum equation via the stress tensor. The treatment of the dissipation is therefore consistent and avoids the need to use an artificial viscosity retaining the correct limiting behaviour as prescribed by the exact Navier-Stokes equations.

As final remark, we should also point out that, in the limit of small λ , although the form of the stress tensor used in section 2.5 and here are the same, the way to discretize it in the SPH formalism, is pretty different. As already mentioned at the beginning of this section, we consider here the deviatoric stress tensor as a further primary unknown variable at the same level as velocity or pressure. $\overline{\sigma}$ is therefore evolved independently and enters in the momentum equation by only one differentiation. This permit to reduce the CPU-time by avoiding both nested sums over the particles and double differentiation of the kernel function in the time loop. On the other hand, in comparisons with the classical SPH (discussed in the previous chapter), we increased weakly the memory costs by the the use of further independent variables describing the stress components.

3.1.3 Non-dimensional formulation

Following the same steps already presented for the momentum equation in the Newtonian case, we will derive here a possible dimensionless form for the constitutive equation. Let us assume to have specified the following primary physical quantities for our problem: a typical length L_0 , velocity V_0 , mass density ρ_0 . Then, we can define the following

secondary quantities in term of the previous one. That is, a typical reference time $t_0 = L_0/V_0$, pressure $p_0 = \rho_0 c_0^2$ (c_0 : speed of sound) and reference value for the friction stress $\sigma = \eta V_0/L_0$ (η : dynamic viscosity). As described in section 10.1, this choice produce the dimensionless momentum equation given in (2.52), where the two free control parameters are the Mach number M and the Reynolds number Re . This form is completely general and remains still valid in the present case.

Adopting the same set of reference quantities mentioned above, the Jaumann-Maxwell equation can be written in the following dimensionless form

$$\frac{d}{dt} \overline{\sigma}^{\alpha\beta} + \overline{\sigma}^{\alpha\gamma} \omega^{\gamma\beta} + \overline{\sigma}^{\gamma\beta} \omega^{\alpha\gamma} = \frac{1}{De} \left(2 \dot{\overline{\epsilon}}^{\alpha\beta} - \overline{\sigma}^{\alpha\beta} \right), \quad (3.9)$$

where all the variables are intended here dimensionless. The new parameter De comes from the coupling between all the reference quantities and is called *Deborah number*. Its definition is

$$De = \frac{\lambda}{t_0}. \quad (3.10)$$

This number controls the elastic effects in the simulated flow by comparing the typical relaxation time λ for the Maxwell model with the characteristic time t_0 where the inertial effects are dominant. It is clear that the limiting case discussed in the previous section correspond to a Deborah number $De \rightarrow 0$, while large value of this parameter characterise proportionally highly elastic liquids. We will see the effects of changing this parameter over the flow properties in the next few sections, where we present the numerical results for the SPH algorithm based on the described viscoelastic model.

3.2 Velocity profile relaxation in a 2D channel

In order to verify the viscoelastic properties of this SPH fluid, which contains the corotational Maxwell model as a prototype, we consider a case for which a simple analytical solution exists. We consider a 2D channel and impose periodic boundary conditions in the x -direction in exactly the same way as previously discussed in sections 2.6 and 2.8. A particular simple time-dependent solution is represented by the viscoelastic characteristic relaxation of an initial sinusoidal 2D velocity profile. We start with the following velocity field

$$V^x(y, t_0 = 0) = \sin(\pi y). \quad (3.11)$$

A peculiarity of a viscoelastic flow is its ability to show oscillatory behaviour during the relaxation process. This behaviour is intimately connected with the fluids transient response when subject to unsteady shear flows.

For simple Newtonian flows, the initial profile decays monotonically to the stationary rest state. If elasticity is considered, oscillations around this final profile appear. In order to compare the numerical solution with the analytical one, we consider the linearised version of the Jaumann-Maxwell model [51], where the corotational derivative is replaced by a partial one. This corresponds to linearising around the stationary

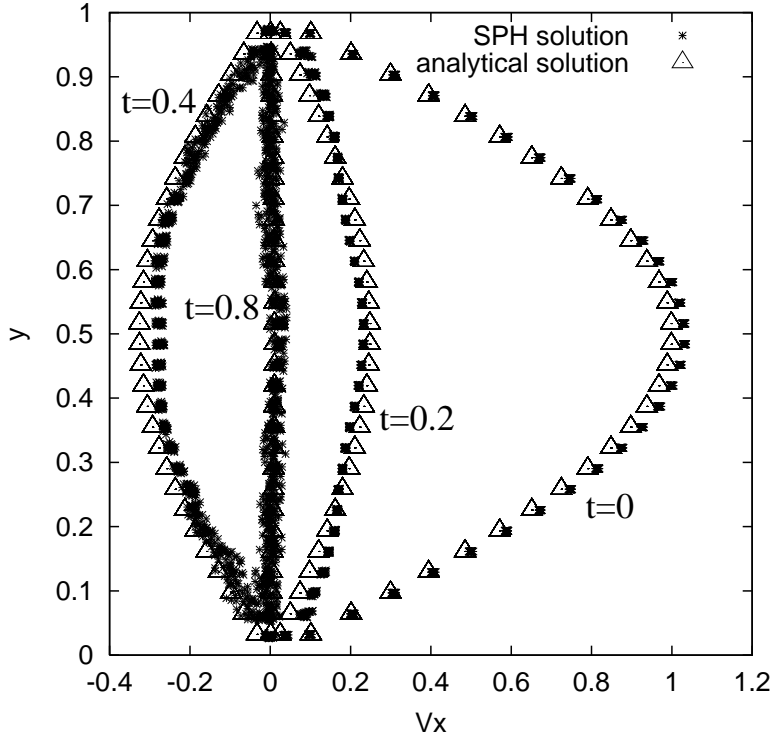


Figure 3.1: The x -component of the velocity field vs. the position y at four different times, where the flow parameters are $Re = 1.0$ and $De = 0.25$. The initial profile has sinusoidal shape. 992 particles are contained in the simulation box (unit length $L = 1$). The cutoff radius for the Lucy function is set to $h = 0.08$. This implies an average of 20 neighbours per particle. An appropriate time step chosen is $\Delta t = 0.0001$, The analytical solution is for the linearised model and serves as a reference. Differences are discussed in Fig.3.3.

state and neglecting advective and rotational terms. After suitable dimensionalization, the linearised equation for the components of the anisotropic stress tensor reads

$$\frac{\partial}{\partial t} \overline{\sigma}^{\alpha\beta} = \frac{1}{De} \left(2 \dot{\overline{\epsilon}}^{\alpha\beta} - \overline{\sigma}^{\alpha\beta} \right). \quad (3.12)$$

Now, remembering the definition of $\dot{\overline{\epsilon}}$ given in eq.(4.69) and substituting the previous expression in the dimensionless form of the momentum equation, we obtain the following equation for the x -component of the velocity field

$$\frac{\partial^2}{\partial t^2} V^x(y, t) + \frac{1}{De} \frac{\partial}{\partial t} V^x(y, t) = \frac{1}{De Re} \frac{\partial^2}{\partial y^2} V^x(y, t), \quad (3.13)$$

where we assumed a constant pressure field $p = p_0$ and a zero y -component of the velocity field $V^y = 0$. In addition, in order to recover eq. (3.13), we consider negligible the contribution coming from the gradient of the velocity in the x -direction as well as the two normal stress coefficients. This permits to eliminate the pressure force and the

advective term in the momentum equation. A particular solution has the following form

$$V^x(y, t) = A(y) \exp(-\beta t) \sin(\omega t + \phi), \quad (3.14)$$

where

$$\beta = \frac{1}{2De}, \quad \omega = \sqrt{\frac{\pi^2}{DeRe} - \frac{1}{4De^2}}, \quad (3.15)$$

where $A(y) = \sin(\pi y)$ and $\phi = \pi/2$ corresponding to our initial conditions.

The solution (3.15) exhibits different behaviours depending of the combination of the two dimensionless numbers De and Re . In the limiting case of $De \rightarrow 0$, the frequency becomes imaginary and the relaxation process is characterised by a strong exponential overdamped decay similar to the ideal Newtonian case. In this regime the flow is dominated by the shear viscosity and the elasticity has almost neglectable effects on the dynamics. In the opposite regime, if the ratio De/Re is not so small, elastic effects become comparable with the inertial ones and a characteristic underdamped decay exhibiting oscillations in the velocity profile around the stationary rest state is observed.

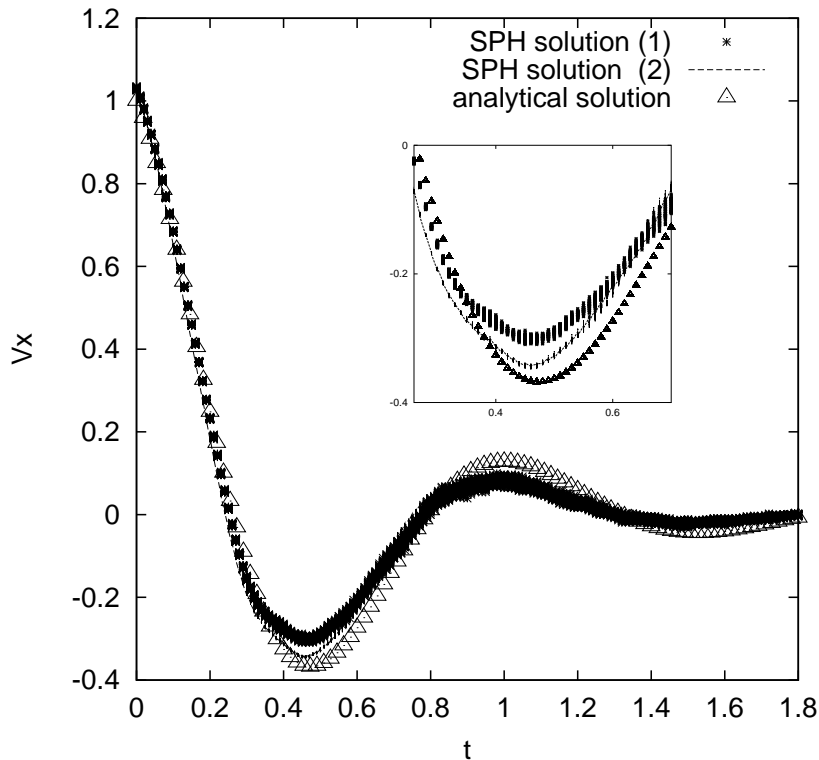


Figure 3.2: Relaxation of the x -component of the velocity at the centre of the channel for the cases where rotational terms are included (1) or disregarded (2) in the SPH simulations. The latter one is to be compared with the analytical solution of the linearised model (triangles). The flow corresponds in all cases to $Re = 1.0$ and $De = 0.25$. The inset provides a zoom into the region where deviations between the three curves are significant.

Next we present numerical simulations corresponding to two typical decay processes. First, we consider a viscoelastic flow with $Re = 1.0$ and $De = 0.25$ (Fig. 3.3). Values of the velocities of the SPH particles in the centre of the channel are here reported and compared with the analytical solution, Eqs. (3.14,3.15). The frequency in (3.15) is real and quite strong oscillations due to elastic effects are observed. The velocity profile still remains sinusoidal but its amplitude becomes sometimes negative. Irrelevant deviations between the analytical and the numerical solution already at $t = 0$ are due to the fact that we do not account for a small correction concerning proper normalisation of the continuous weight function with regard to the finite number of neighbours.

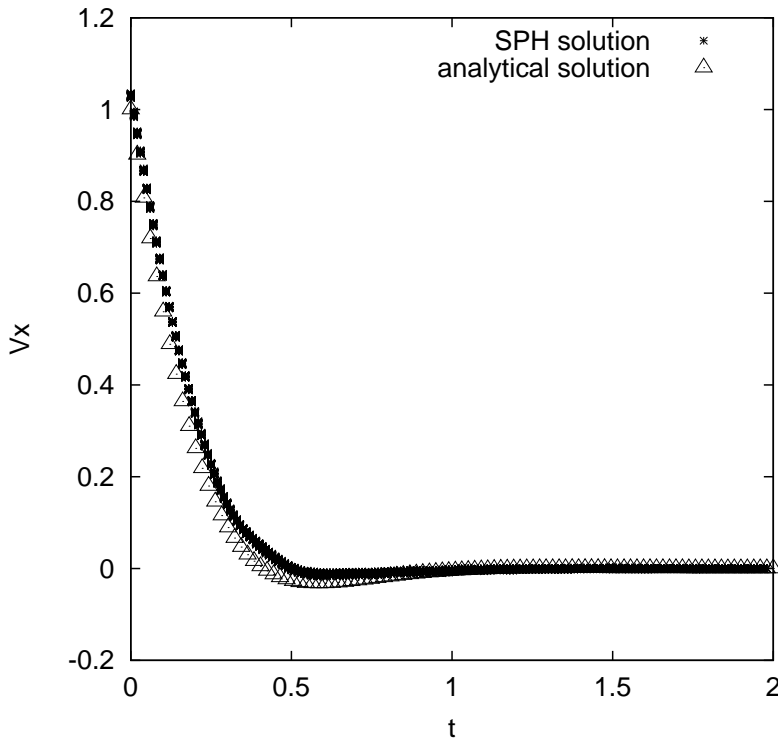


Figure 3.3: Relaxation of the x -component of the velocity field at the centre of the channel vs. time. Flow parameters are $De = 0.1$ and $Re = 2.5$, otherwise same conditions as in fig.3.1. The SPH values for the velocity were sampled from particles whose coordinates were within a range of $h/2$ apart from the centre of the channel: $y = L/2$. Time and velocity are both expressed in dimensionless units.

In order to quantify the approximation made by linearising the Jaumann-Maxwell model, and to test the validity of the foregoing analysis we present an additional result for $Re = 1.0$ and $De = 0.25$ which enables us to identify the origin of the deviations between analytical and simulations results, (Fig. 3.2). The reference run named SPH1 corresponds to the general constitutive equation based on the Jaumann-Maxwell model. For another run SPH2 the rotational terms, corresponding to the second and third one in the lhs of Eq. 4.70, are omitted. The latter is expected to mostly reproduce the given analytical solution, the former is the numerical result of the full model. Small

deviations between the analytical solution and the corresponding numerical solution SPH 2 should be assigned to the finite ‘diameter’ of fluid particles (therefore irrelevant) and to the advective term which is still present in the numerical solution and which is inherent to the Lagrangian nature of SPH. The velocity profiles along the transversal length of the channel at different times are plotted in Fig. 3.2 for all three cases. As expected, SPH2 is closer to the analytical solution than SPH1. We attribute the small differences still present to the approximation of negligible normal stress coefficients which for $De = 0.25$ should be not completely satisfied (see next section).

Finally, the results of a simulation corresponding to $Re = 2.5$ and $De = 0.1$ are presented in Fig. 3.3. As already discussed, here the ratio De/Re becomes roughly 6 times smaller than in the previous case and effects due to elasticity are less evident but still present. Indeed, the x component of the velocity profile becomes still negative even if its value now is very small. This is because in (3.14,3.15) the exponential decay factor β is inversely proportional to De and therefore the relaxation time for the elastic effects is much smaller. On the other side, the frequency is still positive and oscillations are still present. Given dimensionless numbers whose the ratio is further reduced, the frequency becomes imaginary and a form different from (3.14) must be considered for the solution. An overdamped decay is then obtained in which the velocity profile relaxes monotonically as for the limiting Newtonian case.

3.3 Viscoelastic fluid under a steady shear flow

In this section we present a numerical study of the viscometric properties of our fluid model under steady shear flow. Let us assume to have a bulk fluid defined over an unbounded domain. As discussed in the previous chapter (sec. 2.6.1), it is possible to consider only one portion of fluid simulated on a sampling volume (“primary box”), and to remove the unwanted surface effects by using the so called *periodic boundary condition* (PBC). This permits to simulate the fluid at the equilibrium, nevertheless, if we want to extract effective transport coefficients, it is necessary to induce a thermodynamics flux in the system. The usual approach is that one adopted in Non-Equilibrium-Molecular Dynamics (NEMD) simulations and consists into introduce a perturbation in the equation of motion in a way consistent with the PBC, that is, preserving translational invariance and periodicity. There are many attempt to do that: in order to study shear flow response for example, one possibility is to apply a spatially periodic force to the bulk system able to produce an oscillatory velocity profile. Shear rate viscosity of the simulated fluid can be therefore estimated with high accuracy [36].

In the present case, we consider an alternative techniques consisting in a modification of the PBC as proposed originally by Lees and Edwards [52]. The goal here is to induce a steady shear flow in the infinite periodic system by moving in an appropriate way the periodic boxes, i.e. the primary box with all its image boxes on the same layer are assumed to be stationary, while the image boxes lying on the upper and lower layers are moved respectively with velocity $+\dot{\gamma}L$ and $-\dot{\gamma}L$, where L is the size of one box and $\dot{\gamma} \equiv dV_x/dy$ is the *shear rate*. This is shown schematically in fig. 3.4.

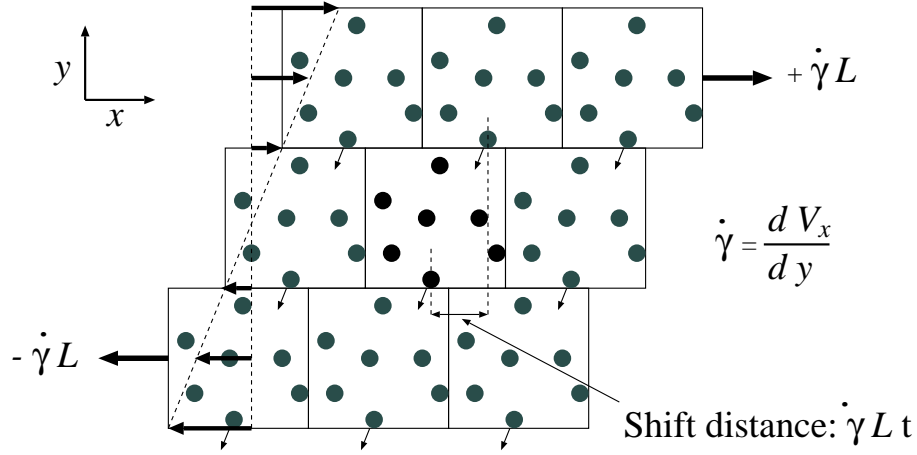


Figure 3.4: Lees-Edwards periodic boundary conditions for a system underlying a steady shear flow.

Numerically, the previous idea is implemented simply by modifying the rule for a particle crossing an upper or lower edge in the main box. Indeed, as shown in fig. 3.4, the particle crossing the lower border will be re-inserted at the top, consistently with the PBC, but now also its x -component of the position will be modified consistently with the underlying shear flow, that is translated of a quantity $\Delta x = \dot{\gamma} L t$ which represents the overall displacement at the time t . A stable linear velocity profile is obtained, which is compatible with the PBC. A detailed discussion on the Lees-Edwards boundary condition can be found in [36].

In order to test our model in this situation, it is helpful to give some theoretical results characterizing the specific behaviour of the corotational Maxwell model under steady shear flow. First, we define the *material functions* which describe the response of the viscoelastic flow under perturbation. In steady simple shear flow, is common to define the *non-Newtonian viscosity* in the following way

$$\eta(\dot{\gamma}) = \frac{\bar{\sigma}_{xy}}{\dot{\gamma}_{xy}}, \quad (3.16)$$

and analogously, the normal stress coefficients Ψ_1 and Ψ_2 as

$$\Psi_1(\dot{\gamma}) = \frac{\bar{\sigma}_{xx} - \bar{\sigma}_{yy}}{\dot{\gamma}_{xy}^2}, \quad \Psi_2(\dot{\gamma}) = \frac{\bar{\sigma}_{yy} - \bar{\sigma}_{zz}}{\dot{\gamma}_{xy}^2}, \quad (3.17)$$

where the macro stress tensor $\bar{\sigma}_{\alpha\beta}$ is now intended as an average quantity over a volume Ω . Numerically, we evaluate it as average over its N values $\sigma_i^{\alpha\beta}$ corresponding to every SPH particle contained in the simulation box

$$\bar{\sigma}_{\alpha\beta} = \langle \sigma^{\alpha\beta} \rangle_{\Omega} = \frac{1}{V} \int_{\Omega} \sigma^{\alpha\beta}(\mathbf{x}') d\mathbf{x}' \approx \frac{1}{N} \sum_{i=1}^N \sigma_i^{\alpha\beta}. \quad (3.18)$$

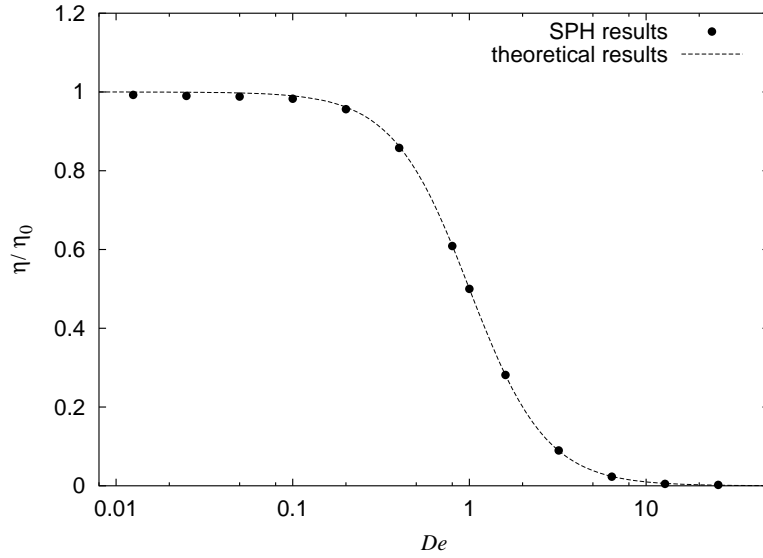


Figure 3.5: Comparisons between the analytical and the numerical non-Newtonian viscosity η versus Deborah number for the corotational Maxwell model in steady-state shearing.

Let us point out that one peculiarity characterizing a viscoelastic fluid, differently to the Newtonian one, is to exhibit a $\dot{\gamma}$ -dependent viscosity and non-zero first normal stress coefficients. In this sense the corotational Maxwell equation (4.70), showing shear thinning, is a “good” model to describe complex rheological behaviours.

An analytical solution for the dependence of the material functions upon the shear rate $\dot{\gamma}$ and elastic relaxation time λ is found to be [7]

$$\eta(\dot{\gamma}, \lambda) = \frac{\eta_0}{1 + \lambda^2 \dot{\gamma}^2} \quad (3.19)$$

for the non-Newtonian viscosity, and

$$\Psi_1(\dot{\gamma}, \lambda) = \frac{2\lambda\eta_0}{1 + \lambda^2 \dot{\gamma}^2}, \quad (3.20)$$

for the first normal stress coefficient, where λ is the relaxation time and η_0 is the viscosity constant appearing in equation (4.70).

For the simulations presented in this chapter, we considered the same dimensional formulation presented in sec. 3.2.3, where now L_0 represents the size of the simulation box and V_0 is velocity difference between two layers of periodic boxes. This corresponds to choose the reference time $t_0 \equiv L_0/V_0 = 1/\dot{\gamma}$, with the shear rate $\dot{\gamma}$ kept constant.

We should point out that in this problem neither L_0 nor V_0 are physically specified: the only parameter uniquely determined is given by their ratio $\dot{\gamma}$. Assuming this, we can rewrite the Reynolds and Mach numbers as $Re = \tau_v \dot{\gamma}$ and $M = \tau_s \dot{\gamma}$, where τ_v and τ_s are, respectively, two typical times characterizing viscous relaxation and sound propagation. Next, we will choose $Re = 0.1$ and $M = 0.1$ (very viscous incompressible fluid) and keep them constant, while we will study the effect of variation of the elastic parameter De on the results.

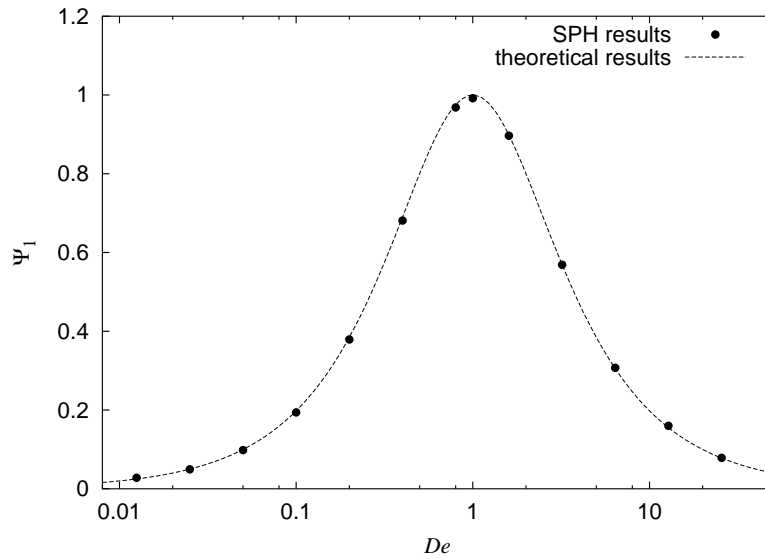


Figure 3.6: Comparisons between the analytical and the numerical non-Newtonian first normal stress coefficient Ψ_1 versus Deborah number for the corotational Maxwell model in steady-state shearing.

In the following we present numerical SPH results of a parametric study in the parameter De and compare them with the analytical solutions properly dimensionalised. For these simulations we considered 2500 SPH particles distributed over a square simulation box and we applied the Lees-Edwards periodic boundary conditions as shown in fig. 3.4. The kernel used was the the Lucy function with a cutoff radius $h = 0.06$, which involves approximately 28 neighbours pro SPH particle. Consistent with the constrains described in Sec. 2.7, the time-step chosen was $\Delta t = 0.001$. We performed 12 different runs corresponding to values of the Deborah number $De = 0.0125, 0.025, 0.05, 0.1, 0.2, 0.4, 0.8, 1.0, 1.6, 3.2, 6.4, 12.8$. In order to extract reliable averages, the final time step was set up to $T_f = 40.0$. This choice involved 40000 time steps for which the systems has safely achieved its steady-state also in the large Deborah number regime, where the relaxation is quite slow.

Figure 3.5 shows the comparison between the predicted non-Newtonian viscosities (3.19) and that ones extracted from the SPH runs for many values of the dimensionless relaxation time, i.e. De . The SPH results fit very well the theory and show the typical shear thinning behaviour characterised by a decreasing viscosity with increased relaxation time. Nevertheless, it can be show that, by modifying Re (i.e. shear rate) the shear stress goes through a maximum before to exhibit shear thinning: this is a lack of the model because such behaviour is never seen experimentally. However, this drawback can be corrected by adding an high shear rate viscosity to the constitutive equation (corotational Jeffreys model) [7]. Figure 3.6 shows numerical comparisons for the first normal stress coefficient Ψ_1 , indicating again a satisfactory accordance with the theory.

Concerning the unrealistic predictions of the model, as already mentioned, we do

not want to discuss its suitability upon other constitutive relations. Our goal here is to validate the SPH algorithm for some “simple” rheological model, while realistic fluid behaviour can be described by replacing equation (4.70) with some more refined models [7,6]. This requires only minor modifications in the coding.

3.4 Viscoelastic matrix with solid inclusions

The analysis of the rheological behaviour of a viscoelastic matrix contaminated with rigid inclusions and underlying a steady shearing is of great importance for many engineering applications. We do not want to give here a complete list of the physical problems encountered in real applications, but for pure illustrative purpose we just mention some of them.

One particular related subject is the problem of wear and deterioration in rail-wheel contact areas [53,54]. During practical use (e.g., wheel-rail slide, load pulsating) the physical properties of the originally pearlite-composed steel forming the rail can change significantly. Indeed, although at the beginning the material is characterised predominantly by a visco-plastic behaviour, after a run-in-time (usually few months) modifications of its microstructure emerge, i.e higher-density layers, creation of hard grains and defects near the contact surface [55].

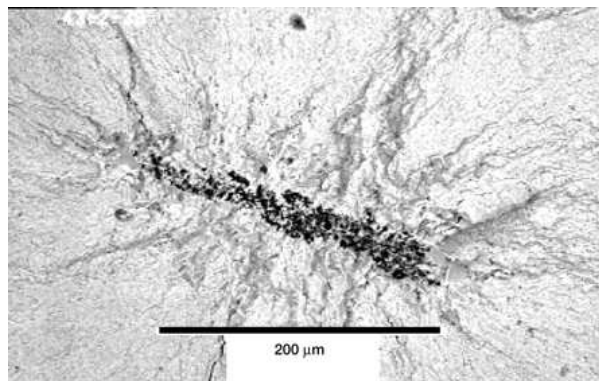


Figure 3.7: Inherent alumina nonmetallic inclusions in a nickel-based superalloy matrix. The propagating cracks are visible, most of them initialising at the specimen surface where the stress concentration assume very high values.

These non-metallic inclusions have been recognized to be the first responsible of hardening in the near-surface regions removing the originally ductile flow behaviour typical of steel [56,57]. The principal cause of this can be attributed to the fact that such defects alter the bulk properties of the steel matrix, producing high stress concentrations at the interfaces with consequent cracks initiations (see fig. 3.7). The resulting composite steel becomes therefore very brittle leading to very high wear rates at the surface. The understanding of wear and friction in composite materials is therefore of main importance in the attempt to reduce such undesirable material deterioration.

If at one side, the presence of non-metallic inclusions can be seen as a undesirable defect characterizing a material, from the other side, it can be regarded in particular cases as an advantage. Under certain conditions, two-phase composite materials possess improved thermo-mechanical properties which make them attractive to use in many industrial applications. Consequently the study of the rheological-mechanical behaviour of complex materials, as for example particulate-reinforced metal-matrix composites, have been investigated experimentally and numerically [58, 59, 60, 61, 62].

In this section, we present the study of the rheological behaviour of a viscoelastic material, modelled via the J-M model presented above, containing rigid non-rotating inclusions and underlying a steady-state shearing. Such a problem has been widely studied from an analytical point of view, nevertheless, the absence of an exact solution in the case of complex matrix behaviour and/or complex geometries makes the numerical approach necessary. In order to give confidence to the model also for complex flow geometries, the case of a Newtonian matrix will be investigated and compared with available analytical solutions. After that, the mechanical analysis of the viscoelastic model will be carried out, discussing qualitative dynamic behaviours and the effect of the inclusion's size on the global rheological properties.

3.4.1 SPH implementation for the inclusion problem

We modify the SPH algorithm described in the previous section in order to handle the inclusion problem. The system is analogous to that one described in fig. 3.4, but here we consider a non-rotating circular object immersed in the fluid and placed at the centre of the simulation box. The periodic boundary conditions produce infinite replicas of it as shown in fig. 3.8 where the usual Lees-Edward boundary conditions are applied in order to produce an homogeneous shear flow along the y -axis.

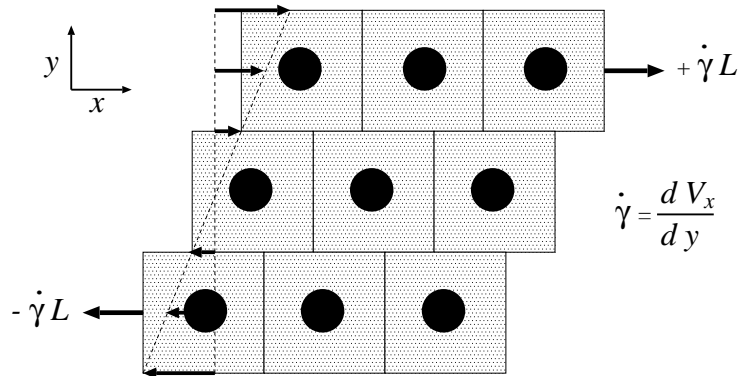


Figure 3.8: Lees-Edwards periodic boundary conditions for a multi-inclusion system underlying a steady shear flow.

The resulting system under study is an infinite two-phase composite containing periodically distributed inhomogeneities (multi-inclusions system) immersed in a viscoelastic matrix modelled by the corotational Maxwell model. This choice corresponds to the Representative Volume Element model (RVE), widely applied in the analysis of

composite materials with microstructure [63, 64]. The assumption which is made here is that the volume simulated is statistically representative of the two-phase composite, in particular, if not specifically dealing with structured materials with a regular distribution of interacting inhomogeneities, the characteristic distance between inclusions should be taken much larger than the typical inclusion size. The boundary conditions at the matrix-inclusion interface are taken into account by considering the Morris image particles as described in sec. 2.6. This assures incompressibility, no-slip tangential velocity and correct gradient interpolations at the interface. In addition a von Neumann boundary condition is considered for the pressure and the friction stress tensor through the boundary.

In the next sections we will perform a flow analysis for the Newtonian case where some analytical comparisons can be performed. This will help us to estimate the level of accuracy of our method for this particular geometry and, on the other hand, provide a reference Newtonian solution for the further comparisons in the viscoelastic case.

3.4.2 Flow analysis: Newtonian matrix

To evaluate the accuracy of the SPH method for the multi-inclusion problem, we present first some results in the case of a Newtonian matrix. We solve the usual SPH equations for Newtonian quasi-incompressible fluids (already tested for the Couette and Poiseuille flows in sec. 2.8) coupled with the boundary conditions associated to the rigid inclusion.

The geometry of the problem is sketched in fig. 3.9 and it corresponds to a Newtonian fluid under shear flow in which numerous fine solid particles are suspended. The hydrodynamic fields are therefore perturbed by the presence of these solid particles and, as a consequence, the viscosity η of the two-phase medium will slightly differ from the Newtonian solvent viscosity η_0 .

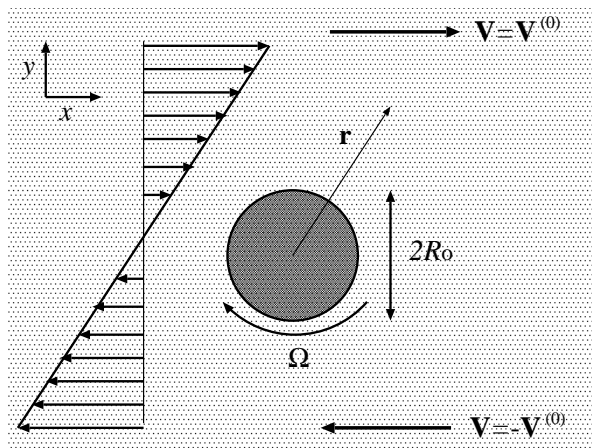


Figure 3.9: Geometry for the inclusion problem.

An analytical solution for the hydrodynamic fields is available in the literature for

the 3D case where rotating suspended particles are considered [40]. Here we present a calculation for the general case where a particle is allowed to possess a suitable angular velocity $\boldsymbol{\Omega}$, see fig. 3.9. For the sake of simplicity, in this section the common vectorial notation will be used. We split the velocity field \mathbf{V} in two parts $\mathbf{V} = \mathbf{V}^0 + \mathbf{V}^1$, where $\mathbf{V}^0 = \dot{\gamma} \mathbf{r}$ is the unperturbed flow represented by the linear velocity profile, while \mathbf{V}^1 is the unknown perturbation. Now, let us assume that, for $r \rightarrow \infty$, the velocity field can be assumed unperturbed and we write it as $\mathbf{V} = \mathbf{V}^0 = \boldsymbol{\Gamma} \cdot \mathbf{r} + \boldsymbol{\omega} \times \mathbf{r}$, where $\boldsymbol{\Gamma} = \overline{\nabla \mathbf{V}^0}$ is the traceless strain rate tensor and $\boldsymbol{\omega} = (1/2)(\nabla \times \mathbf{V}^0)$ is the vorticity. With these substitutions we solve the Navier-Stokes equations for a stationary flow $\nabla p = \eta \Delta \mathbf{V}$ coupled with the condition $\nabla \cdot \mathbf{V} = 0$ for the incompressibility and appropriate boundary conditions at the inclusion-fluid interface which we assumed here to be $\mathbf{V} = \boldsymbol{\Omega} \times \mathbf{r}$ for $r = R_0$. We search for solutions of the following form

$$p = c \eta \boldsymbol{\chi}^{(2)} : \boldsymbol{\Gamma}, \quad \mathbf{V}^1 = a_1(r) \boldsymbol{\Gamma} \cdot \boldsymbol{\chi}^{(1)} + a_2(r) \boldsymbol{\chi}^{(3)} : \boldsymbol{\Gamma} + b(\boldsymbol{\Omega} - \boldsymbol{\omega}) \times \boldsymbol{\chi}^{(2)} \quad (3.21)$$

where, for $D = 3$, $\boldsymbol{\chi}^{(k)} = (-1)^k \nabla \cdot \nabla_k r^{-1}$, while $\boldsymbol{\chi}^{(k)} = (-1)^k \nabla \cdot \nabla_k \ln(r^{-1})$ for $D = 2$, and $c = -(2 + D)/D$ where D is the dimensionality. By substituting these expressions in the NS equation, for $D = 2$ we obtain finally

$$p(\mathbf{r}) = -4\eta \frac{R_0^2}{r^2} \hat{\mathbf{r}} \cdot \boldsymbol{\Gamma} \cdot \hat{\mathbf{r}} \quad (3.22)$$

for the pressure field while

$$\mathbf{V}(\mathbf{r}) = \left(1 - \frac{R_0^4}{r^4}\right) \boldsymbol{\Gamma} \cdot \mathbf{r} + \left(1 - \frac{R_0^2}{r^2}\right) \boldsymbol{\omega} \times \mathbf{r} + \frac{R_0^2}{r^2} \boldsymbol{\Omega} \times \mathbf{r} + 2 \left(\frac{R_0^4}{r^4} - \frac{R_0^2}{r^2}\right) \mathbf{r} \hat{\mathbf{r}} \cdot \boldsymbol{\Gamma} \cdot \hat{\mathbf{r}} \quad (3.23)$$

represents the exact steady-state solution for the velocity field.

In the remaining of this section we will discuss the SPH results for the problem presented above and compare them with the analytical expression previously calculated. In order to consider an infinite medium we apply the Lees-Edward periodic boundary condition and we solve the dimensionless equation corresponding to eq. (2.52) where the dimensionless control parameters, Re and M , are defined in the same way as in eq. (2.56). We should notice that here, differently to the case considered in Sec. 3.4, L_0 represents a characteristic length of the problem which quantifies the distance between the inclusions. Based on the choice of L_0 , we choose $V_0 = L_0$ in order to have a dimensionless shear rate $\dot{\gamma} = 1$. In order to compare our numerical results with the analytical expressions, we consider a rigid non-rotating ($\boldsymbol{\Omega} = \mathbf{0}$) circular inclusion with radius $R_0 = 0.1$ in dimensionless box units. The dimensionless numbers considered here are $Re = 0.1$ and $M = 0.1$. Boundary conditions are treated with boundary images particles completely filling the area occupied by the inclusions and interacting hydrodynamically with the fluid particles. We should point out that the problem under study is characterised by a strong perturbation of the particle paths around the inclusion. This produces a very disordered particle distribution in its surrounding (fig. 3.10: left) and introduces a large amount of noise in the numerical results. As a consequence, the

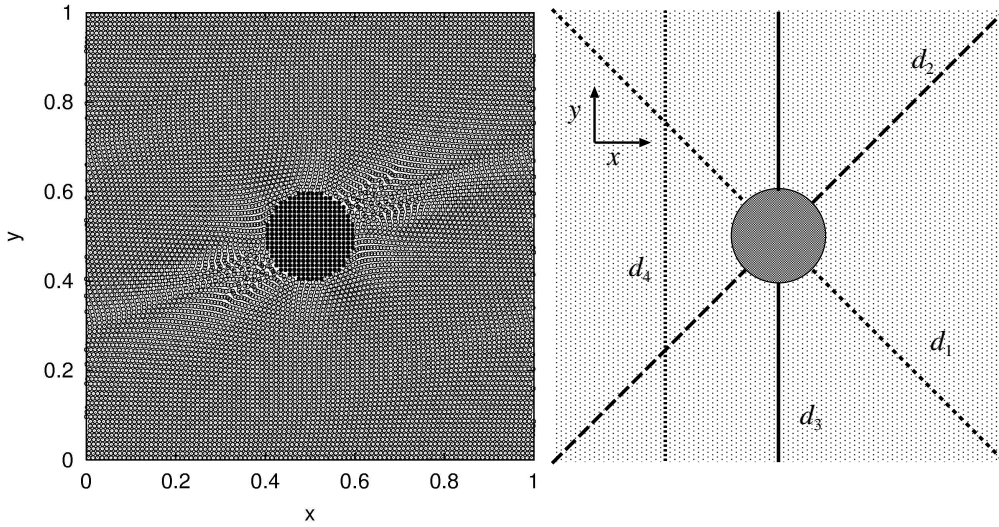


Figure 3.10: Left: numerical SPH discretisation for the primary box. SPH bulk particles (white) and fixed boundary particles (black) are shown. The total system is sheared as shown in fig.3.8, while Lees-Edwards periodic boundary condition are imposed for particles approaching the borders of the box. Right: paths for comparisons of SPH and analytical solutions.

SPH runs were found to be very unstable and small fluctuations in the velocity field were observed to increase rapidly in time eventually causing the code to crash. From a numerical point of view, we found that better results could be obtained by using the XSPH variation for the equations of motion, eq. (2.33), with an higher-order kernel function. In the present work we choose $\epsilon = 1$ in eq. (2.33) and we adopt for the kernel function the quintic spline kernel (2.46) discussed in sec. 2.5. As already mentioned, the XSPH equation results in a smoother velocity field cutting out some of the subgrid velocity fluctuations. Additionally, according to Morris [42], the quintic spline kernel, although a little more expensive, has been found to be much less sensitive of particle disorder in comparison with the usual Lucy kernel.

For the simulation presented in the following we used 10000 SPH particles, more precisely, 9864 bulk and 136 boundary particles. The SPH implementation of this problem is sketched in fig. 3.10. The cutoff radius for the kernel function was $r_c = 3h = 0.031$ which involves an average number of neighbours equal approximately to 30.

We notice that the analytical solutions (3.22) and (3.23) correspond to the limiting case of an unique inclusion immersed in a bulk fluid. In the limiting dilute regime, that is $R_0 \ll L_0$, this solution can be still considered reliable but the numerical realization of this condition can be very CPU-demanding because it involves the discretisation of an area much bigger than the interesting one, near the inclusion, where the important physical effects take place. In the present case we considered $R_0 = 0.1 L_0$ which is small but still comparable with the mean inter-inclusions distance. Effects due to their interactions should therefore be expected in the numerical results.

Solutions of the type (3.22) and (3.23) are time-independent, nevertheless, if as already mentioned, contributions from interacting inclusions should come into play, the problem becomes clearly time-dependent and the previous expressions are not able to represent the unsteady evolution of the system.

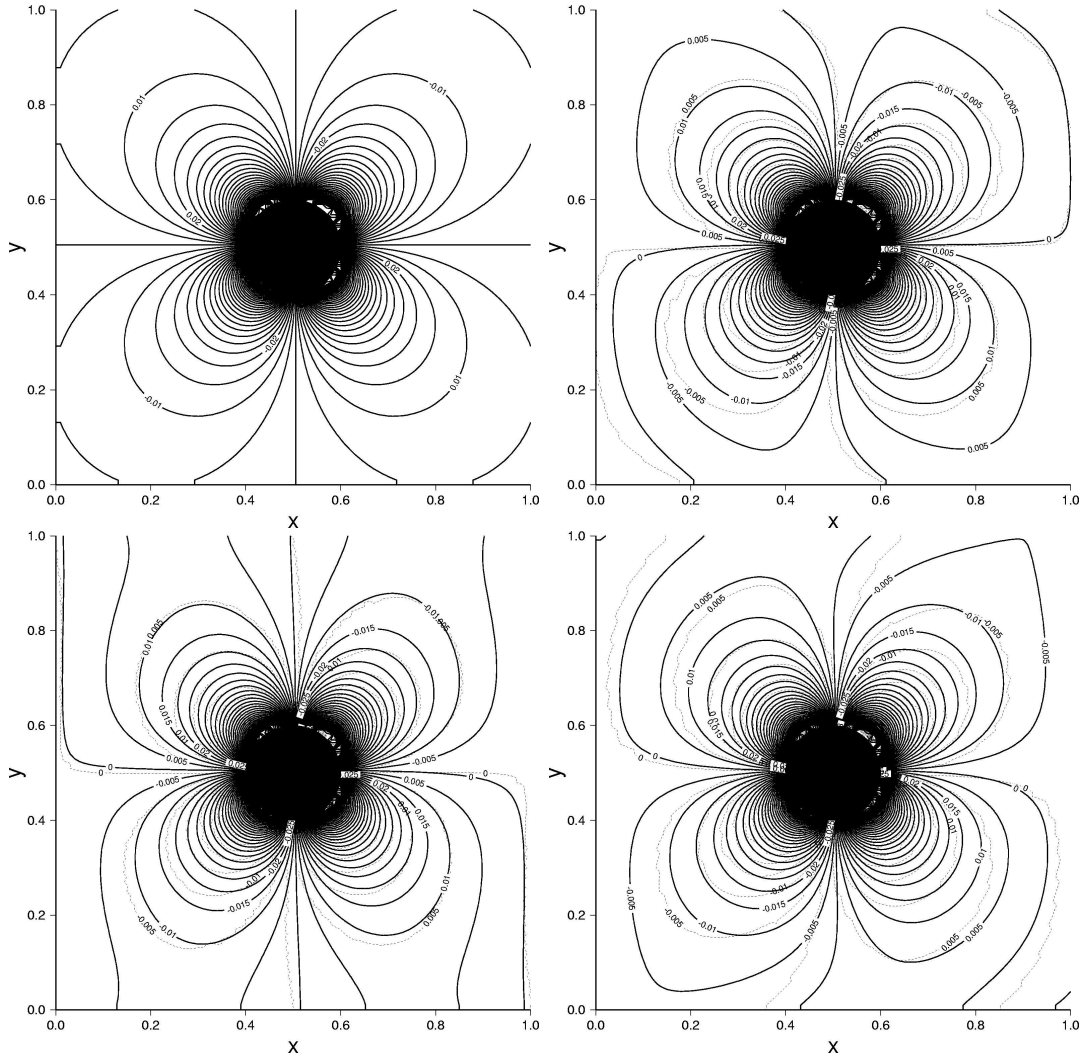


Figure 3.11: Top-left: steady-state solution for the pressure field corresponding to eq. (3.22). The remaining pictures show snapshots compared between the SPH and the theoretical solution, eq. (3.24), for $T = 0.2, 0.5, 0.8$, respectively from left to right, top to bottom. Solid lines correspond to the theoretical solutions, while the dotted lines are the SPH results.

In order to do a comparison with the analytical expressions previously evaluated, we assume that the theoretical solution at one particular location of the domain can be in first approximation estimated as superposition of expressions respectively of type (3.22) and (3.23). In more exact terms, the value of an hydrodynamic field at the position \mathbf{x} is due to the contribution of terms corresponding to the analytical fields for inclusions placed at the centres of neighbouring boxes. The final solution for the pressure field is

evaluated as

$$p(\mathbf{x}) = \sum_i p_i(\mathbf{x}) \quad (3.24)$$

where $p_i(\mathbf{x})$ are the theoretical solutions evaluated at the positions $(x_0 - L_0, y_0)$, $(x_0 + L_0, y_0)$, $(x_0 - \dot{\gamma}L_0\Delta t, y_0 - L_0)$, \dots , $(x_0 + \dot{\gamma}L_0\Delta t, y_0 + L_0)$ and (x_0, y_0) is the position of the inclusion in the main box. It should be also noticed that, due to the Lees-Edwards boundary conditions, the positions of the inclusions corresponding to the higher and lower boxes change in time. As a consequence, the problem can no longer achieve a stationary configuration but time periodic contributions of the images boxes will be added to the hydrodynamic fields.

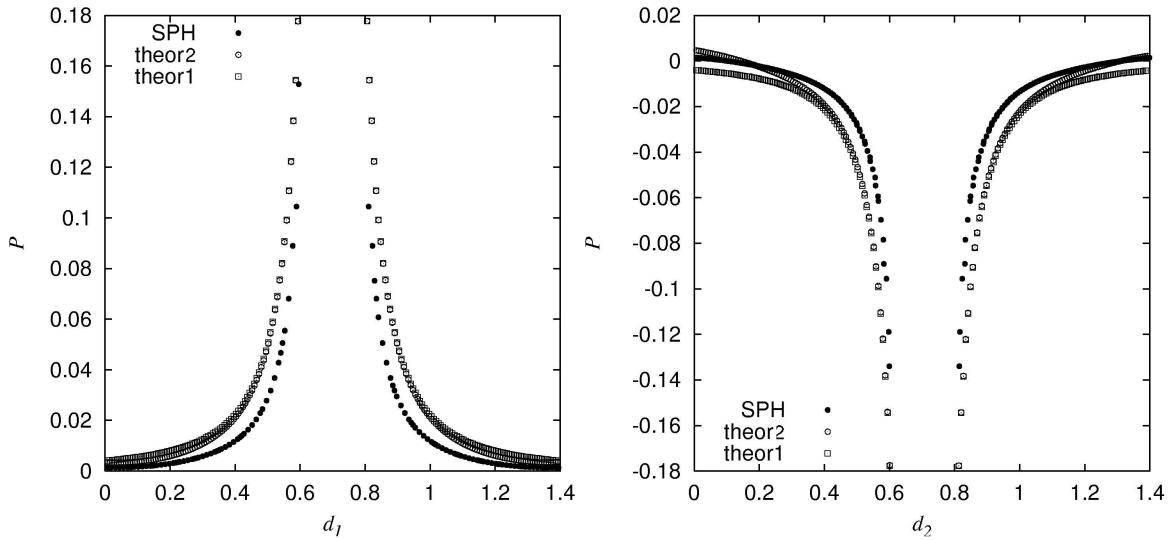


Figure 3.12: Comparisons between the pressure evaluated by SPH (●), by eq. (3.22) (□) and by superposition (3.24)(○) .

Let us start considering the pressure field $p(\mathbf{x})$. Fig. 3.11 shows four different configurations. The first figure, top-left corner, shows the steady state solution corresponding to equation (3.22) while the remaining pictures illustrate the comparison between the SPH results and the superposed analytical solutions previously discussed. The comparisons are made for three different configurations corresponding to time $T = 0.2, 0.5, 0.8$. The theoretical solutions are obtained by the superposition (3.24) for the 8 first image boxes. It is clear that the first steady-state solution is not able to represent the pressure field, while a time-dependent superposition of them, at least qualitatively, captures its unsteady evolution.

The previous arguments shows that a choice of $R_0 = 0.1$ is not appropriate to consider the two-phase system as a dilute suspension of rigid particles, but interactions between them are relevant. In order to quantify the deviations of our results, let us consider the two paths corresponding to the diagonals d_1 and d_2 plotted in fig. 3.10 and compare quantitatively the respective numerical and analytical pressure field sections along them. They are shown in fig. 3.12 where the constant equilibrium pressure was subtracted from the numerical one for comparisons.

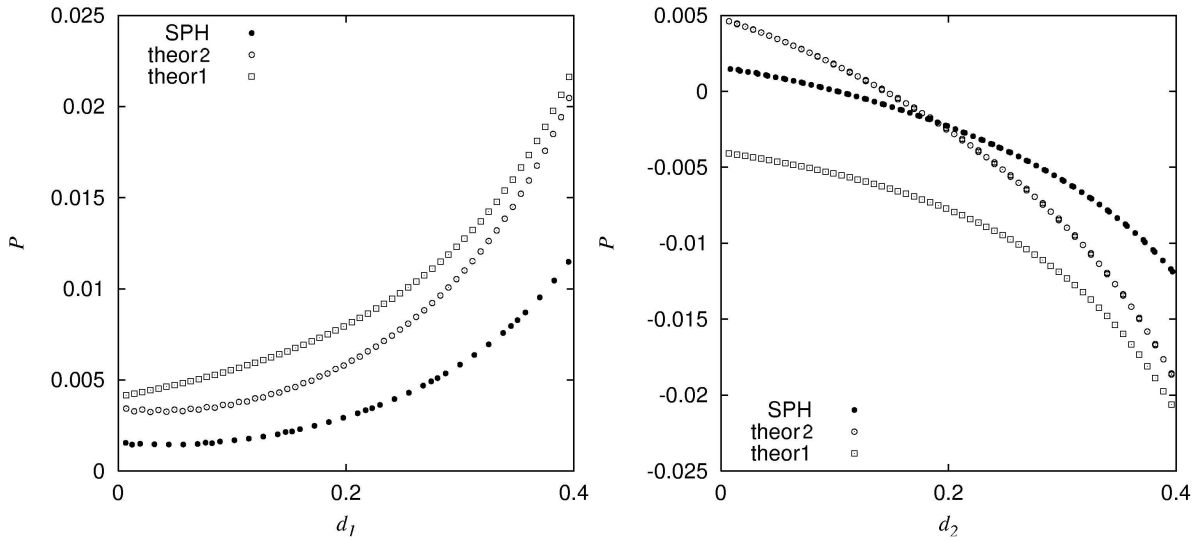


Figure 3.13: Inspection of the pressure profiles evaluated by SPH (\square), by eq. (3.22) (\circ) and by superposition (3.24) (\bullet) in the range $[0:0.4]$ along d_1 and d_2 .

In the figure 3.12 the SPH pressure with the two analytical solutions above discussed are plotted. The pressure variation exhibits in all cases the expected profile corresponding to an increase along the path d_1 approaching the inclusion. This effect is due to the imposed velocity field which forces the fluid particles (in that region) to proceed toward the obstacle increasing the mass density and, via the equation of state, the pressure. On the other side, the symmetric decrease is observable along d_2 . Although the qualitative pressure behaviour has been captured, a good quantitative agreement has not been achieved.

Fig. 3.13 shows a zoom in the range of d_1 and d_2 between 0 and 0.4. Differences between the three curves are visible. The departures from the SPH solution in both the two analytical cases seem to be quantified by a factor 2 near the rigid wall. On the other hand, in the far region ($d_1, d_2 \rightarrow 0$), the superposition solution (3.24) seems to represent better the pressure field, giving a positive contribution in accord with the numerical results, while eq. (3.22) predicts an unrealistic negative pressure (fig. 3.13: right). We associate the departures between the SPH and the theoretical solution to the absence of interacting hydrodynamics contributions in the analytical description. An exact treatment should be done by considering the full multi-component inclusions problem in the solution of the Navier-Stokes equations.

We should also point out that the small numerical values obtained in the pressure fields in comparison with the theoretical solution could be also due to the quasi-incompressible equation of state adopted. This involves a still large but finite speed of sound in contrast with the exact incompressibility assumption, $\nabla \cdot \mathbf{V} = 0$, which prescribes an infinite value.

In order to get more confidence with the SPH method for this particular problem, next we try to compare the velocity field with a superposed solution of (3.23). Fig. 3.14 shows a comparison between the analytical and numerical solutions at time $T = 0.1$.

Here we compare the two velocity fields along the two paths shown in fig. 3.10 and corresponding to $d_3 : x = 0.5$ and $d_4 : x = 0.25$. The V_x components of the velocity field are plotted vs. the y -coordinate spanning the two paths, showing a very satisfactory agreement.

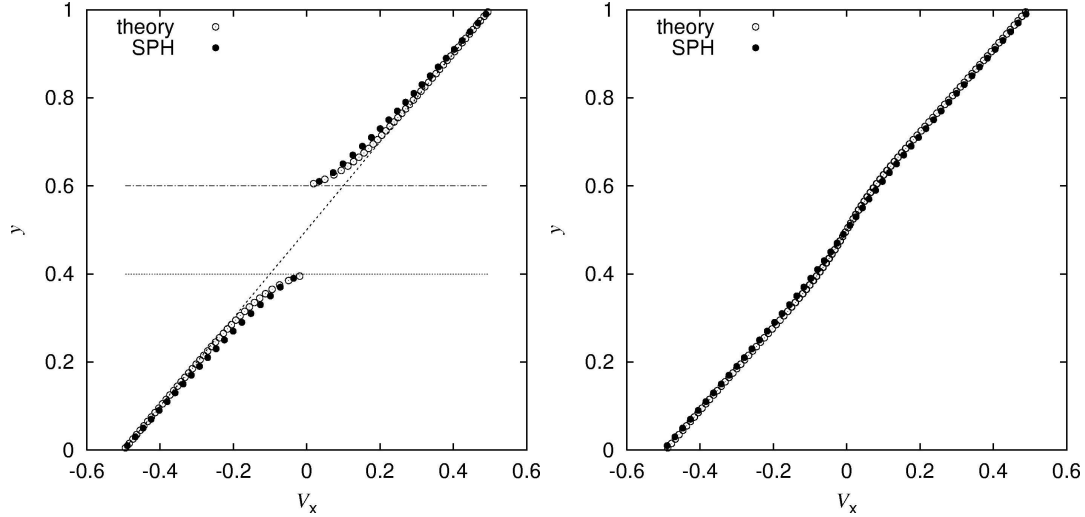


Figure 3.14: Comparisons of SPH (●) and theoretical (○) velocity profiles along path d_3 (left) and d_4 (right).

It can be easily seen that the velocity field, although almost linear in the far region, it is highly distorted in vicinity of the inclusion (fig. 3.14: left). This perturbation is due to the imposition of a no-slip tangential velocity at the fluid-inclusion interface, and become clearly particularly strong along path d_3 which crosses directly the area of the inhomogeneity. Nevertheless, effects can be observed also in regions not directly approaching the inclusion, as for example along d_4 where deviations from the unperturbed linear profile are visible (fig. 3.14: right). We recognise in these distortions of the velocity field the main cause for the overall stress field variations and the consequent increase in viscosity of the two-phase medium. Indeed, by simply looking at the Newtonian constitutive equation (2.40), we see that the components of the friction stress tensor are locally proportional to the gradients of $\mathbf{V}(\mathbf{x})$. On the other hand, it is clear that the condition of no-slip at the interface forces the fluid particles approaching the inclusion to reduce their speeds, with the consequent production of potentially large velocity gradients in the boundary layers. This is shown in fig. 3.15 where the variation of $\partial_y V_x$ and S_{xy} along the path d_2 are respectively plotted.

As expected, near the inclusion the velocity gradient assumes values much larger than in the bulk (approximately a factor 3) producing, via the Newtonian constitutive equation, proportionally large values of the stress field. To conclude, we associate to these perturbations induced by the inclusions, the increase observed in the effective shear viscosity which in our case takes a value $\eta/\eta_0 = 1.028$. This value was evaluated by the same box average (3.16) described in the previous section, applied here only to the fluid particles. In the next section, we will consider the influence of a viscoelastic

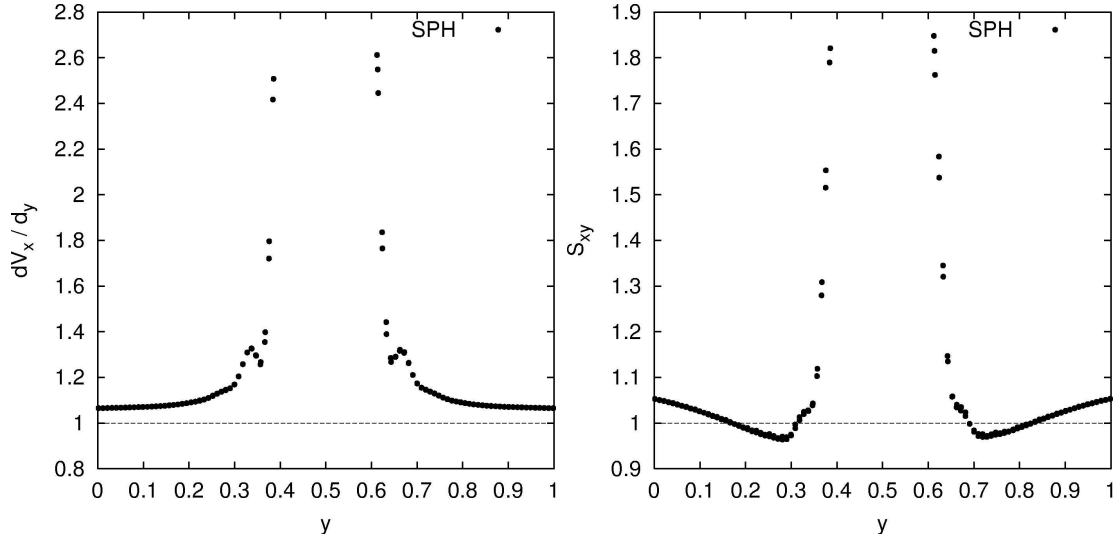


Figure 3.15: Gradient of the velocity field $\partial_y V_x$ (left) and the off-diagonal friction stress component S_{xy} evaluated numerically along the path d_3 .

matrix, described by the corotational Maxwell model, on the specific flow behaviour and overall transport properties.

3.4.3 Rheological analysis: non-Newtonian matrix

In the previous section we applied the SPH method to the multi-inclusion problem consisting of a Newtonian matrix with periodically-distributed suspended objects. We showed that the local dynamics of the matrix is in a substantial good agreement with the theoretical expressions based on a superposition of independent solutions for the single-inclusion problem.

In this section we consider the case of a viscoelastic matrix, described by the JM model, and present some results for its global rheological behaviour, i.e. viscoelastic material functions. This problem has been widely investigated numerically modelling the viscoelastic stress tensor mainly via power-law constitutive equations [65, 66, 67]. The goal here is to show how the presence of the inclusions modify the usual rheological behaviour of the free viscoelastic matrix under constant shear flow. The functions which characterise the two-phase composite, i.e. non-Newtonian shear viscosity η and first normal stress coefficient ψ_1 , are still defined here following equations (3.16)-(3.18), but the global stresses are evaluated by averaging only over the values corresponding to those fluid particles lying in the inner domain (without boundary particles).

Figure 3.16 shows the deviations which take place in the non-Newtonian shear viscosity η (top) and first normal stress coefficient ψ_1 (bottom) depending on the elastic parameter De . Here, three curves are plotted corresponding to different values of the inclusion radius in dimensionless box units. The case $R = 0$ corresponds to the shear flow without inclusion already showed in fig. 3.5 and 3.6 and it is included only for comparisons. An effective increase over all the range of De is clearly visible indicating,

as prescribed by the Landau theory in the Newtonian case, a certain dependence for the viscosity of the two-phase material on the dimensions of the inclusions.

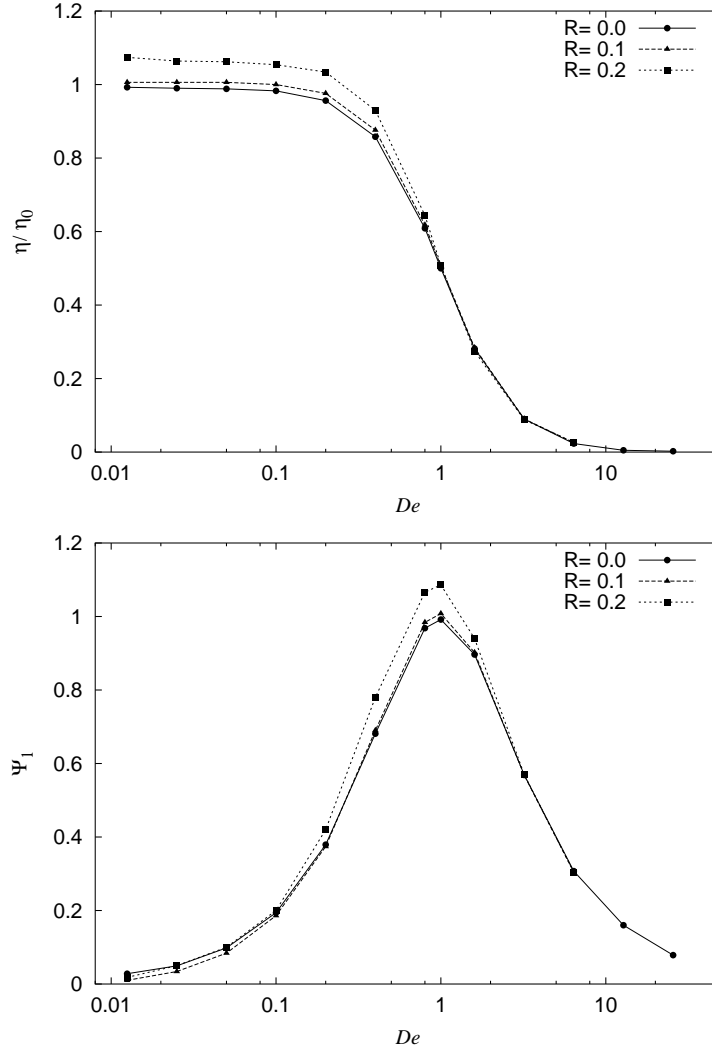


Figure 3.16: Non-Newtonian shear viscosity (top) and first normal stress coefficient (bottom) vs. De for different values of inclusion's radius. The curve for $R=0$ corresponds to the shear flow without inclusions (for reference).

The previous results show that the two-phase medium exhibits qualitatively the same rheological behaviour as its solvent matrix and therefore, it could be described in principle by the same constitutive equation but characterised by some slightly modified viscometric parameters. Indeed, figures 3.16 suggest to consider an *effective* non-Newtonian shear viscosity η^{eff} defined in the following way

$$\eta^{eff}(\dot{\gamma}) = \eta(\dot{\gamma})(1 + \phi(R)) \quad (3.25)$$

and *effective* first normal stress coefficient Ψ_1^{eff}

$$\Psi_1^{eff}(\dot{\gamma}) = \Psi_1(\dot{\gamma})(1 + \phi(R)) \quad (3.26)$$

where now the parameter ϕ depends on the radius R of the inclusions or, in other words, on their volume concentration. This is defined as the ratio between the volume occupied by the inclusions and the total volume occupied by the composite materials.

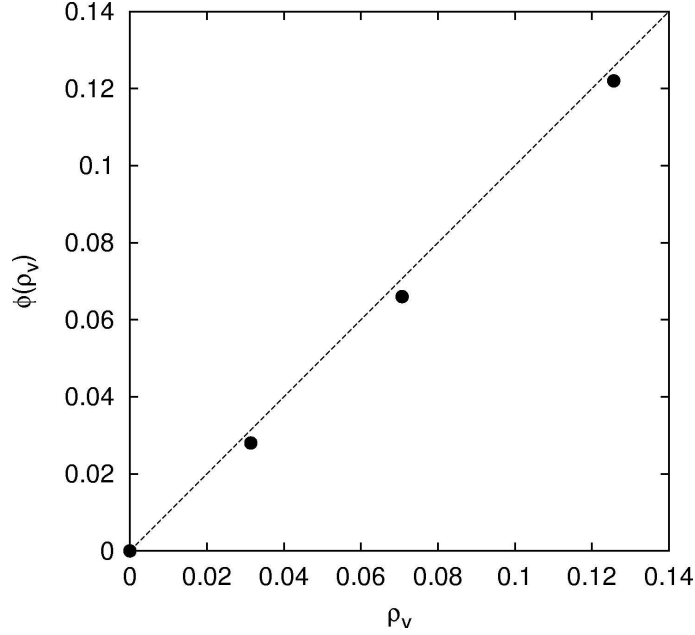


Figure 3.17: Dependence of the parameter ϕ on the volume concentration of inclusions $\rho_v = \pi R^2$. The points correspond to steady-state values for the shear viscosity of a non-Newtonian composite obtained for different values of R , underlying a constant shear rate and characterised by an elasticity $De = 0.01$.

It is interesting to notice that the value of effective viscosity tends, in the limit of small De , exactly to that one evaluated for the Newtonian fluid, that is 1.028. In such limiting case, fortunately it is possible to compare such value with a theoretical estimate calculated under the hypothesis of dilute suspensions of inclusions [40]. In the 2D case it reads

$$\eta^{eff} = \eta_0 (1 + 2\rho_v) \quad (3.27)$$

where ρ_v represent the volume concentration, which in our dimensionless box units corresponds exactly to the 2D volume of the inclusion πR^2 . The theoretical analysis prescribes therefore a linear dependence of ϕ on ρ_v with proportionality factor equal to 2. In figure 3.17, we interpolate the results for the function $\phi(\rho_v)$ extracted from 3 different numerical runs corresponding to inclusions of radius respectively $R = 0.1, 0.15, 0.2$.

From fig. 3.17 it is clearly visibly that the SPH runs predicts a linear behaviour for the function ϕ in the range of ρ_v considered. Nevertheless, the factor of proportionality

seems to be nearly 1 while that one predicted analytically in eq. (3.27) is 2. The difference between the two curves could be assigned to the different way to evaluate the global averages. Indeed, numerically we perform volume integrals but analytically we evaluate surface fluxes. It is possible that in such derivation some terms have been neglected giving an overestimate of the viscosity, nevertheless a rigorous explanation still lacks. It should be finally noticed that such a simple linear relation is not ensured for larger values of ρ_v (larger than 0.3 in 3D) where more complex non-linear contributions could appear [68].

3.4.4 Flow analysis: non-Newtonian matrix

As previously done for the Newtonian case, also in this section we present some results for the local dynamics, flow patterns and deformations features around the inclusions. Unfortunately, there are no theoretical solution available for the non-Newtonian case, nevertheless it is interesting to have a look inside the system in order to have a better understanding of its dynamical properties.

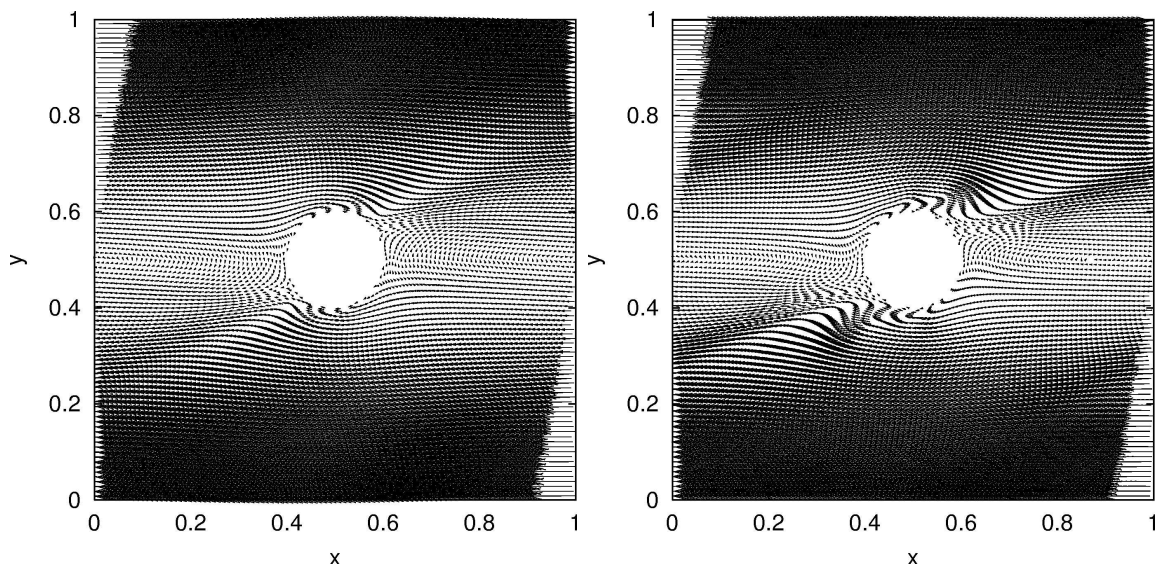


Figure 3.18: Velocity fields in the case of a Newtonian (left) and Non-Newtonian matrix (right) characterised by an elastic parameter $De=0.1$ in the JM model and underlying a constant shear rate $\dot{\gamma}$ corresponding to $Re = 0.1$.

Figure 3.18 shows a snapshot of the velocity fields at time $T=2$ in the case of a Newtonian matrix (left) and for a viscoelastic matrix characterised by $De = 0.1$ (right). The snapshot was chosen at a certain arbitrary time when all the material functions achieved their steady-state values. It is clearly visible as the presence of the inclusion deforms the flow patterns around it. In particular the distortions are more evident on the top and bottom regions near the surface, where the particle paths exhibit a curved profile. Such effect increases by considering, instead of a Newtonian, a viscoelastic matrix as shown in the right part of figure 3.18. In addition, by increasing the Deborah

number, it seems that such structures assume deeper convex arrangements eventually perturbing the flow field in regions far from the inclusion. This fact suggests that the Deborah number, which characterises the relative contribution to the elastic effects over the inertial ones, is a crucial parameter determining the topology of the flow patterns in composite materials.

Such distortions in a multi-inclusion problems have strong resemblance with those ones observed by Samanta et al. in the case of a Newtonian matrix with rotating inclusions [68]. Nevertheless, in that case the role played by the Deborah number here, seems to be assumed from the concentration parameter ρ_v . Indeed, similar qualitative behaviours are obtained by increasing the concentration volume (from 0.01 to 0.4 in 3D), which, contrary, in our case has been kept constant equal to about 0.03.

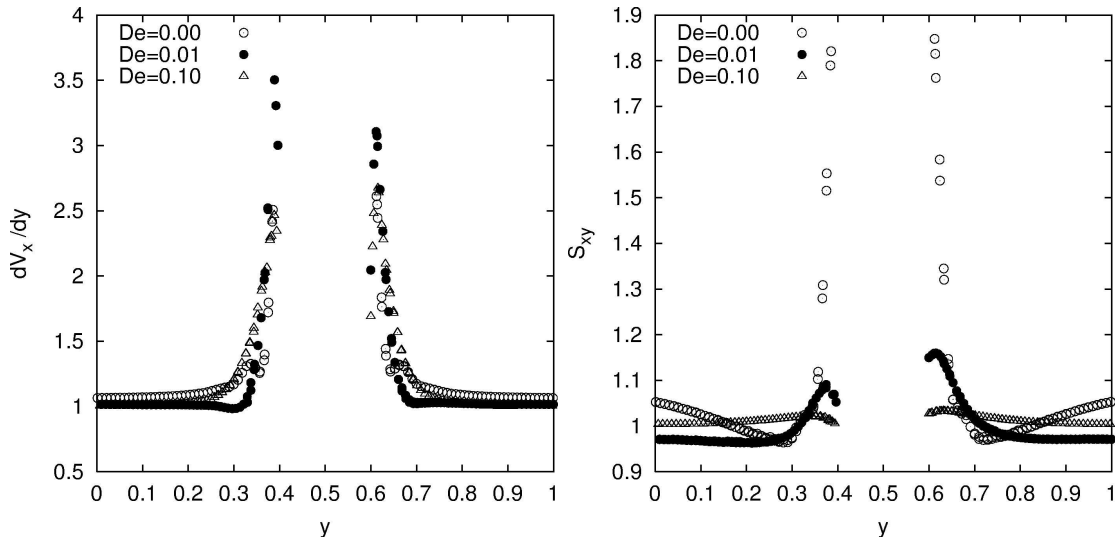


Figure 3.19: Gradient of the velocity field $\partial_y V_x$ (left) and the off-diagonal friction stress component S_{xy} evaluated numerically along the path d_3 for $De = 0.01, 0.1$. The results for $De=0$ correspond to the Newtonian case, here shown as reference.

Figure 3.19 shows some cross section for the gradient of the velocity field $\partial V_x / \partial y$ and off diagonal component of the stress field S_{xy} along the path d_3 for different values of De . The results for $De=0$ correspond to the Newtonian case, here shown for comparison. Although the velocity gradients do not vary too much for different De , oppositely, appreciable changes in the stress field can be observed. Indeed, for increasing values of the elastic parameter De , the correspondent stress fields change in a much smoother fashion over the domain (see the maximum values for the stress at the interface). This can be in principle explained in terms of the rheological behaviour of the JM model depending on the elastic parameter De . Indeed fig 3.19 (right) indicates that by reducing De , proportionally smaller will be the shear response of the system to a given fixed shear rate $\dot{\gamma}$. In this sense, the Deborah number has a sort of *smoothing* control over the stress field.

This can be also observed in fig. 3.20 where we showed different snapshots of the stress field $S_{xy}(\mathbf{x})$. In particular, fig. 3.20 (a) represents the steady-state stress configuration in

the Newtonian case. As mentioned above, here the stress field change remarkably over the domain exhibiting very low concentrations (≈ 0.14) in the vicinity of the inclusion along the x -axis (see the two violet symmetric areas lying at the left and right side of the inclusion, corresponding to low-shear, high-vorticity recirculating regions) and, at the same time, very high concentration (≈ 1) in the fluid near the top and bottom interface. Fig. 3.20 (b,c,d) represent snapshots for a viscoelastic matrix characterised by $De=0.1$.

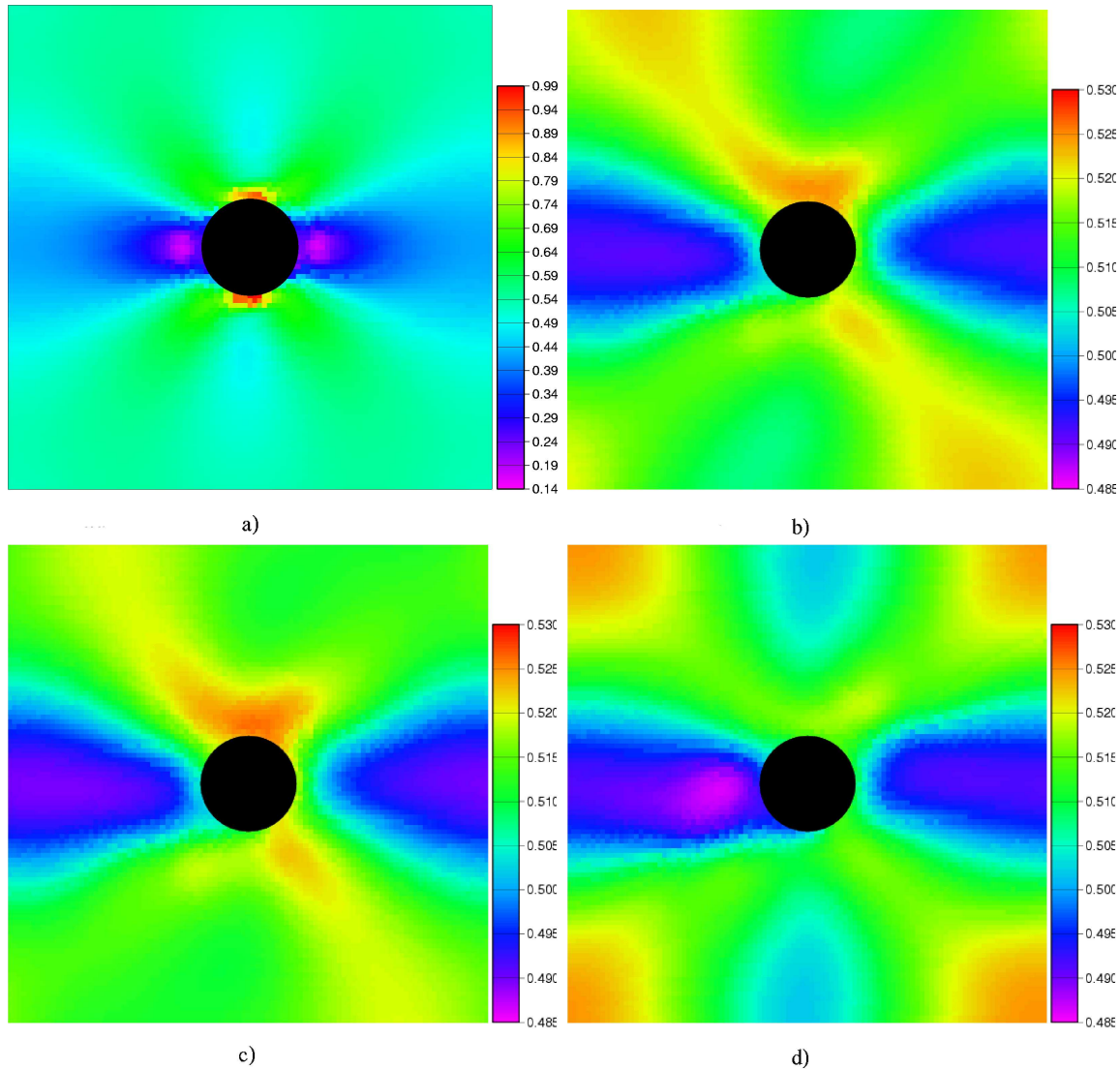


Figure 3.20: (a) Steady-state configuration for $S_{xy}(\mathbf{x})$ in the Newtonian case. (b)-(d) Snapshots of the stress configurations at time $T = 2, 2.25, 2.5, 2.75$ for a viscoelastic matrix ($De=0.1$).

First, we notice that, contrary to the Newtonian case, here there is no steady-state stress configuration but it change over the domain in a very complex time-periodic fashion. Indeed, it can be seen as the region of higher stress concentration have a certain

directionality, which corresponds exactly to the line connecting periodic inclusions. In addition, coming back to the smoothing effect discussed above, even if the powerful colours of the images corresponding to $De=0.1$ could trick the reader, it is clear from the scale reported on the right columns that the viscoelastic dynamics is much more continuous than for a Newtonian matrix.

The previous pictures indicate that the interactions between periodic inclusions should play an important role in the case of a viscoelastic matrix (more than for a Newtonian one). On the other hand, this can be understood considering the fact that here, different to a Newtonian fluid, perturbations of the stress fields decay to zero over a finite time quantified by De . If De is large enough, stress waves can persist longer in time and eventually propagate to the next periodic inclusion. If this would be the case, we should expect stronger interactions for increasing De or, alternatively for decreasing distance between inclusion (i.e. increasing R).

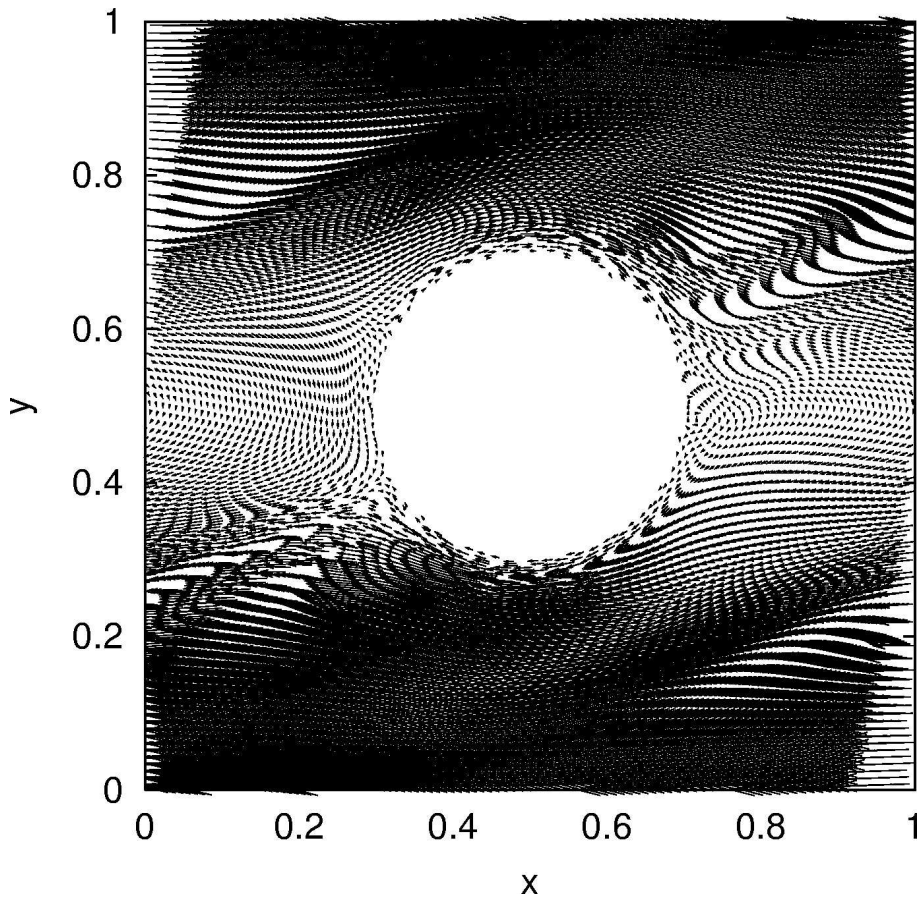


Figure 3.21: Velocity field for a viscoelastic matrix characterised by $De = 0.01$. The radius of the inclusion is in this case $R = 0.2$ in box units.

This is indeed what has been observed, at least qualitatively, in the next results. There, we performed another simulation considering a viscoelastic matrix, $De = 0.01$, with inclusions of radius $R = 0.2$ in box units. From fig. 3.21, which shows the corresponding velocity field, it is evident that the flow perturbations can reach now easily the

next periodic inclusion and are extended to almost all the space covered by the fluid: compare this picture with the flow field showed in fig. 3.18 where the velocity field is distorted only in a region near the inclusion.

Finally, in fig. 3.22 we present four snapshots for the time evolution of $S_{xy}(\mathbf{x})$. Even if the Deborah number here is not so large (0.01), the dynamics indicate very strong interaction areas, which now cover almost the entire domain. The times are respectively $T = 2, 2.25, 2.5, 2.75$ for the pictures (a)-(d).

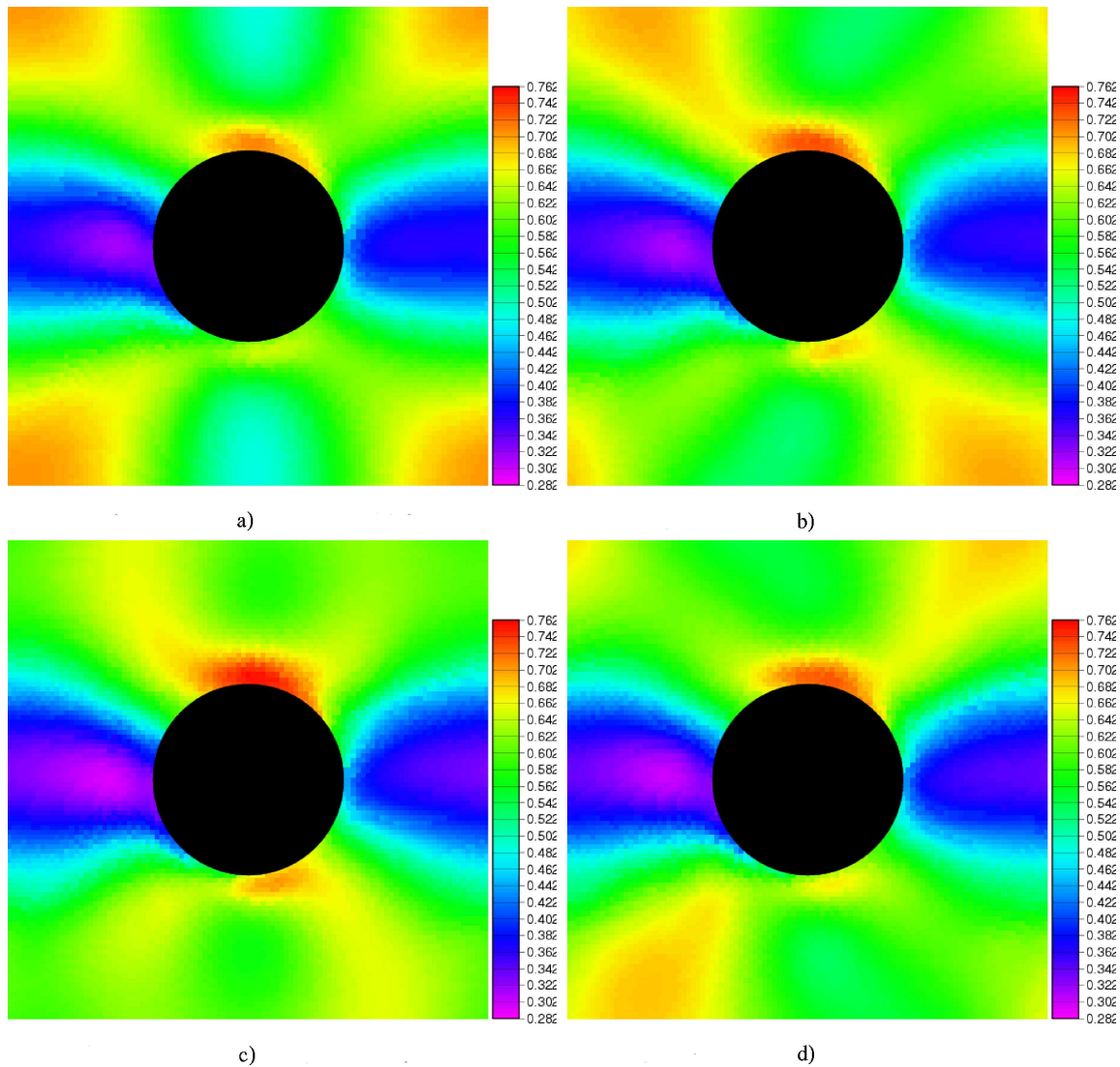


Figure 3.22: Snapshots of the evolution of $S_{xy}(\mathbf{x})$ at time $T = 2, 2.25, 2.5, 2.75$. The solvent matrix is characterised by $De=0.01$.

The dynamics exhibits an increasing complex evolution, characterised by structures in the stress field which are periodically generated and destroyed depending on the relative position of the neighbouring inclusions. At such large volume concentration the

dynamics of the system is definitely influenced by the mutual interactions between the rigid objects defining the microstructured network. At such level, the isotropy of the system, assumed valid in the limiting case of dilute concentration, is clearly not satisfied but very complex directional-preferred macroscopic properties could be showed by the resulting composite material. Further investigations in this direction are a must.

To conclude, we would like to point out that, even if not rigorous, the qualitatively analysis carried out in this section has been useful to explain some global properties exhibited by the material functions characterizing two-phase composite. The dynamics of the flow fields showed very exotic behaviours which can be partially understood as an interplay between two crucial parameters: the Deborah number De , which controls the magnitude of the elastic effects in the matrix, and the volume concentration ρ_v which estimates the relative space occupied by the inclusions in the systems. The problem studied here is not at all closed, inversely, there are still many open questions related to the connection between macroscopic material properties and microstructural dynamics. In this sense, the results presented in this section should be intended not as definitive, rather as a starting point for new stimulating theoretical and numerical explorations.

Chapter 4

Smoothed Particle Dynamics for mesoscopic problems

The modelling of a fluid by a direct discretisation of a deterministic set of partial differential equations is valid, basically, under two ansatz: the continuum hypothesis and the assumptions that thermal fluctuations can be neglected. The first one tells us that the length and time scales of variation for the variables, which we choose to describe the problem, are much larger than the typical atomistic scales characterizing the underlying physics: that is, the system can be seen as a “continuum”.

The second assumption is much more strict than the first one. Indeed, a coarse-grained system where fluctuations can be neglected represents a subclass of a continuous system. In that case, the only effect coming from the elimination of freedom degrees show up as dissipation which can be described deterministically. Systems which satisfy the previous two requirements will be called *macroscopic*. On the other hand, systems which can be still described continuously but in which fluctuations play a crucial role will be referred later on as *mesoscopic*.

In this chapter we focus on the description of a complex fluid at the mesoscopic scale. After a brief overview in section 4.1 on the existing numerical techniques, we recall in sec. 4.2 the so-called Dissipative Particle Dynamics method for the description of complex fluids. Sec. 4.3, 4.4 and 4.5 are devoted to the formulation of a thermodynamically consistent fluid particle model for non-isothermal polymeric solutions. Its structure follows the rigid prescriptions of the GENERIC formalism for the construction of physical models consistent with the First and Second Law of Thermodynamics. In sec. 4.6 the polymeric diffusivity is considered and introduced in the previous formalism. Finally, numerical results for the isothermal case are presented in sec. 4.8, while in sec. 4.9 we discuss good aspects and drawbacks of this model.

4.1 Modelling mesoscopic flow problems

The Smoothed Particle methods presented in the first two chapters make the implicit assumption that the macroscopic equations of motion are known on theoretical or phenomenological grounds and that they model at a certain level of accuracy the physical

problem under investigation. This is the case of a simple Newtonian fluid, where the Navier-Stokes equations are an established tool of description. Indeed, for this particular problem, a consistent derivation from the microscopic “atomistic” picture can be obtained using a kinetic theory [69]. On the other hand, exact coarse-graining procedures applied to fluids characterised by a complex microstructure are usually not available and approximated constitutive equations must be used. The problem of deriving “consistent” (microscopically) macroscopic constitutive equations for complex fluids will be discussed in great details in the next chapter.

Here, we would like to focus the attention on the mesoscopic level of description of a particular fluid. In fact, it is well-known that, if the physical scales of the problem become smaller than a typical length, thermal fluctuations arise naturally in the system. Evidently, physical problems for which such fluctuations are important can not be described on the basis of the traditional numerical methods based on a simple discretisation of macroscopic equations. At the same time such problems, involving scales much larger than typical atomistic size, can be numerically very demanding when modelled by microscopic techniques, i.e. Molecular Dynamics methods. The presence of a extraordinary variety of complex phenomena at the mesoscopic scales, ranging from colloidal fluids, polymer dynamics to porous systems to mention but a few, creates a great demand of adequate numerical methods able to capture the physics occurring in such systems. It is not the goal of this section to give a complete list of the methods which have been developed in the last fifty years, however a very schematic overview of the most popular ones is in order. We can distinguish two basic directions in which such methodologies have been carried on: grid-based techniques and grid-off particle methods. In the first group enter the well-known Cellular Automata (CA), Lattice Gas (LG) and Lattice Boltzmann (LB) methods. These techniques gained popularity in the computational community due to their very simple structure which allows for very efficient numerical algorithms. An overview on the basis of such approaches can be found for example in [70]. On the other hand the presence of some difficulties in the grid-based methods, mostly associated to lattice artifacts due to the lack of rotational invariance, has carried to the development of a large number of off-grid methods which involve the basic, and maybe more physical, concept of “particle” against that one of grid node. In this class, maybe the most popular is the so called Dissipative Particle Dynamics method (DPD) and therefore we will spend here some words about. DPD, as originally invented by Hoogerbrugge and Koelman, is a stochastic particle model for the simulation of Newtonian fluids at mesoscopic scales [71], [72]. In DPD, a Newtonian fluid is represented by a collection of points whose interactions can be defined as a sum of conservative, dissipative and stochastic forces that conserve momentum and produce hydrodynamic behaviour. The Brownian stochastic term introduces fluctuations in the system, mimicking the statistical behaviour of the unresolved scales averaged out in the coarse graining process. The way to introduce it is determined by the fluctuation-dissipation theorem relating the amplitude of the noise to a viscous parameter present in the dissipative force. This condition ensures the correct fluctuating hydrodynamics as prescribed by the Landau and Lifshitz theory [40]. However, there are many problems connecting to this DPD formulation. As it has been recognized by Espanol [73], the

original DPD model cannot specify an arbitrary thermodynamic behaviour (i.e the form of equation of state is dictated by the kinetic theory derivation), it has not a well-defined physical scale and one needs to use kinetic theory to relate the transport coefficients of the fluid with model parameters. Nevertheless, it has been shown that by including in the original DPD model two extra state variables, the internal energy and the volume of the particles, one can solve its conceptual shortcoming, exhuming a *thermodynamically consistent* (TC) version of DPD which has a strong resemblance in the structure with the Smoothed Particle Hydrodynamics method except for the presence of thermal fluctuations. The new method extracts, so to say, the best of the two techniques above mentioned, thermal fluctuations from DPD and connection to Navier-Stokes from SPH: the resulting formulation can be also seen as a TC version of SPH which should be use in place of the usual SPH equations as far as the length scale characterizing the problem is so small that the fluid feels effects of its microstructure. The connection between DPD and SPH with its relative TC version has been deeply investigate in [73] in the case of simple Newtonian fluids. The generalisation of this model for the study of more complex viscoelastic fluids will be the subject of this chapter [74].

4.2 Mesoscopic simulations of complex fluids

The primary objective of DPD research has been to use this stochastic fluid solver for the study of Non-Newtonian fluids displaying interesting and complex rheological behaviour like, for example, colloidal suspensions and polymeric solutions. The simple Newtonian fluid of DPD has been made “complex” by introducing additional interactions between the dissipative particles. For example, the complex rheological behaviour of colloidal suspensions has been simulated by freezing spheres (i.e. introducing a rigid interaction between particles) of DPD particles that behave like solid suspended objects [75], [76], [77]. Polymer solutions have been simulated by connecting some of the dissipative particles with springs [78], [79]. Binary mixtures have been also modelled by considering two types of particles that interact with different interaction parameters [80], [81], [82]. In this respect, DPD turns out to be a versatile method for the simulation of complex fluids. A couple of recent reviews on applications of DPD to the simulation of complex fluids can be found in Refs. [83], [84].

A very interesting generalisation of the Dissipative Particle Dynamics model has been recently introduced by ten Bosch in order to study polymer flows [30]. The idea is to capture the complex behaviour of polymeric fluids by introducing an additional variable \mathbf{Q} associated to each particle [30]. The vector \mathbf{Q} collects the elastic information about the fluid at scales “within” the dissipative particles. The introduction of the additional internal variable \mathbf{Q} is a radically different way of introducing complexity in the DPD model. It actually changes the scale of the technique with respect to those DPD simulations in which elasticity is modelled through springs connecting dissipative particles. A particle in the ten Bosch model would represent large portions of particles in previous DPD simulations of polymers. It represents, therefore, a serious computational advantage. Of course, the price to pay for this advantage is the required deep knowledge of the physics of the mesoscopic viscoelasticity in order to formulate

the suitable equations of motion for \mathbf{Q} . Because the ten Bosch model is a more coarse grained model than the usual DPD models for polymers, molecular details are hidden in the phenomenological parameters of the model. However, from the point of view of applications and computer time saving, this might be regarded in some cases as a benefit.

The ten Bosch model suffers from the same conceptual shortcomings of the original DPD model: it is not thermodynamically consistent, it is not possible to specify arbitrary thermodynamic behaviour, has not a well-defined physical scale, and one needs to use kinetic theory to relate the transport coefficients of the fluid with the parameters of the model. The aim of this chapter is to formulate in a thermodynamically consistent way a generalisation of the ten Bosch model to non-isothermal situations. To this end we first formulate a model in which each fluid particle contains a fixed number of dumbbells. This model can be understood as a Lagrangian SPH version of the CONNFESSIT approach [11], [85]. Inspired by this model, in a second step we consider only one elongation variable per fluid particle, as in the ten Bosch model. This second model is much faster to simulate because of the large reduction of dumbbell variables in the system. In addition, this second model incorporates the number of dumbbells in the cell as an additional variable and allows one to study polymer diffusivity problems. The model is essentially a version of the smoothed particle hydrodynamic model like the one presented in Ref. [73], with additional elastic variables. As a final remark, we note that this approach is radically different to that one presented in the previous chapter. Indeed, here the viscoelasticity is introduced by modelling mechanically the behaviour of model springs, without assuming the validity of suitable macroscopic constitutive equations. As it will be clear later, as far as this model will be used at macroscopic scale, the price to pay will be memory and CPU-time requirements for the numerical algorithm.

4.3 TC fluid particle model of polymer solutions

A very convenient way to construct new discrete models for fluid dynamics which are consistent with Thermodynamics is by using the GENERIC framework [86] which we summarise in Appendix A. This framework, introduced by Öttinger and Grmela, captures in a very synthetic way all the required constraints that a model should satisfy in order to comply with the First and Second Law. It also describes how to introduce thermal fluctuations in a consistent way through the Fluctuation-Dissipation theorem. No additional physics is introduced in GENERIC further than the First and Second Laws and the Fluctuation-Dissipation theorem. However, it facilitates enormously the task of constructing new models which are compatible with these physical laws. This approach has been successfully used in Refs. [73], [28], [87], where mesoscale fluid particle models for Newtonian fluids have been constructed.

Here we model a polymeric solution through a collection of M *fluid particles* with positions \mathbf{r}_i and velocities \mathbf{v}_i which are understood as representing real portions of the material. They are regarded actually as small thermodynamic subsystems that move following the flow. Each thermodynamic subsystem is composed by N_i^s molecules of the solvent plus the N_i^d polymer molecules. We will assume initially that the numbers N_i^s ,

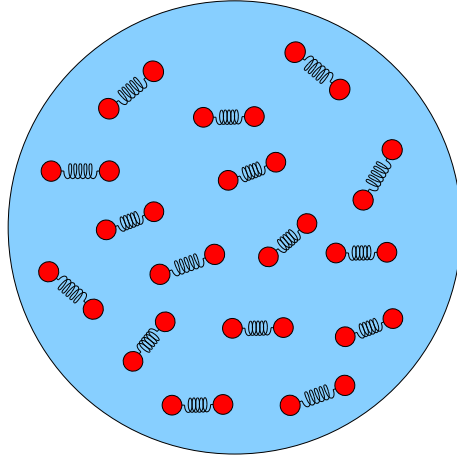


Figure 4.1: A schematic representation of a fluid particle containing N_i^d dumbbells. The set of the elongations of the dumbbell within the fluid particle i is denoted by \mathbf{Q}_i .

N_i^d are fixed, and, therefore, the mass of each fluid particle is constant. In section 4.7 we will relax the condition of constant number of dumbbells N_i^d per fluid particle. The simplest model for a polymer molecule is a dumbbell, where two beads are connected with a spring, and for the sake of presentation we will focus on this simple model. Every dumbbell in the fluid particle is characterised by its end-to-end vector or elongation \mathbf{Q}_i^α , where $\alpha = 1, \dots, N_i^d$ runs over the different dumbbells of the fluid particle i . We show schematically a fluid particle in Fig. 4.3.

Every fluid particle has two additional thermodynamic variables, which are the internal energy E_i and the volume \mathcal{V}_i . The internal energy E_i represents the contributions of kinetic energy of the solvent and bead particles with respect to the centre of mass of the fluid particle plus the potential energy of interaction (including solvent-solvent, solvent-bead, and bead-bead interactions). The volume of a fluid particle is not an independent variable but rather depends on the positions of the given particle and its neighbours. In some recent works [88], [87] the partitioning of the space occupied by the fluid has been done through the Voronoi tessellation. In this case, each particle has associated a cell around it with a given volume that depends on the location of the neighbouring particles. In the SPH philosophy [73], one rather provides a volume \mathcal{V}_i to each particle through the inverse of a density d_i which is defined by

$$\frac{1}{\mathcal{V}_i} = d_i = \sum_j W(r_{ij}). \quad (4.1)$$

Here, $r_{ij} = |\mathbf{r}_i - \mathbf{r}_j|$ and $W(r)$ is a bell-shaped function of finite support r_c and which is normalised to unity

$$\int d\mathbf{r} W(r) = 1. \quad (4.2)$$

Note that this way to introduce a volume variable is consistent with the SPH formalism described in Chapter 2. Consequently, also the kernel functions can be assumed to be

one of those ones discussed in section 2.5.

Finally, every fluid particle, that is, every thermodynamic subsystem, has associated an entropy function $S_i(E_i, \mathbf{Q}_i)$. The microscopic definition of this entropy function is given by the logarithm of the “number of microstates” which are compatible with prescribed values of E_i, \mathbf{Q}_i [89]. In more precise terms,

$$S(E_i, \mathbf{Q}_i) = k_B \ln \int dz \delta(H(z) - E_i) \delta(\mathbf{Q}_i(z) - \mathbf{Q}_i), \quad (4.3)$$

where z is the set of microscopic degrees of freedom (positions and velocities of the solvent molecules and beads), $H(z)$ is the Hamiltonian of the fluid particle. If the Dirac delta functions containing \mathbf{Q}_i were not present, (4.3) would be the equilibrium thermodynamic entropy of the fluid particle. The introduction of these delta functions arises from our requirement of describing the system at a more refined level of description, through the \mathbf{Q} variables.

We compute the entropy of a fluid particle through Eq. (4.3) in the Appendix B under the basic assumption that the suspension is dilute (so we may neglect the interactions among the dumbbells and between the dumbbells and the solvent). The result is

$$S(E, \mathbf{Q}) = S^s(E) - \frac{V(\mathbf{Q})}{T^s(E)} + k_B N^d (1 + \ln n^d \lambda_d^D), \quad (4.4)$$

where the dumbbell density number is $n^d = N^d/\mathcal{V}$. In obtaining this equation, we have neglected terms that scale as the inverse $1/N^s$ of the number of solvent molecules. We have introduced the solvent entropy $S^s(E)$ which is assumed to be a known function of its arguments. The generalised entropy depends on the dumbbell potential

$$V(\mathbf{Q}) = \sum_{\alpha}^{N^d} V^d(\mathbf{Q}^{\alpha}), \quad (4.5)$$

where $V^d(\mathbf{Q})$ is the spring potential of a single dumbbell. It is possible to show that for multi-bead-spring models, the entropy has a form identical to (4.4) except that an effective potential appears instead of $V^d(\mathbf{Q})$. The solvent temperature introduced in Eq. (4.4) is defined by

$$\frac{1}{T^s(E)} = \frac{\partial S^s(E)}{\partial E}, \quad (4.6)$$

whereas the thermal wavelength λ_d of the dumbbells is

$$\lambda_d = \left(\frac{h^2}{2\pi m_d k_B T^s(E)} \right)^{1/2}. \quad (4.7)$$

The constants k_B, h, m_d and D are the Boltzmann constant, the Planck constant, the mass of one bead of the dumbbell, and the dimension of physical space, respectively.

4.4 GENERIC formulation

We will denote by $x = \{\mathbf{r}_i, \mathbf{v}_i, E_i, \mathbf{Q}_i, \quad i = 1, \dots, M\}$, the full state of the system, where $\mathbf{Q}_i = \{\mathbf{Q}_i^\alpha, \alpha = 1, \dots, N_i^d\}$ is the collection of the elongations of the dumbbells of particle i . The total energy of the system is given by

$$E(x) = \sum_i^M \frac{m}{2} \mathbf{v}_i^2 + E_i. \quad (4.8)$$

Here, E_i must be understood as the total internal energy of the fluid particle, including elastic contributions from the suspended dumbbells. The total entropy of the system will be

$$S(x) = \sum_i S(E_i, \mathbf{Q}_i, \mathcal{V}_i). \quad (4.9)$$

Note that the entropy of the full system is defined as the sum of the entropies of each cell taken as thermodynamic sub-systems, that is, by the sum of the function (4.3) evaluated at $E_i, \mathbf{Q}_i, \mathcal{V}_i$. This is the well-known *local equilibrium assumption*.

For future reference we present here the derivatives of the energy and entropy functions (computed in the appendix B) with respect to the state variables,

$$\frac{\partial E}{\partial x} = \begin{pmatrix} \frac{\partial E}{\partial \mathbf{r}_i} \\ \frac{\partial E}{\partial \mathbf{v}_i} \\ \frac{\partial E}{\partial E_i} \\ \frac{\partial E}{\partial \mathbf{Q}_i^\beta} \end{pmatrix} = \begin{pmatrix} \mathbf{0} \\ m\mathbf{v}_i \\ 1 \\ \mathbf{0} \end{pmatrix}, \quad (4.10)$$

$$\frac{\partial S}{\partial x} = \begin{pmatrix} \frac{\partial S}{\partial \mathbf{r}_i} \\ \frac{\partial S}{\partial \mathbf{v}_i} \\ \frac{\partial S}{\partial E_i} \\ \frac{\partial S}{\partial \mathbf{Q}_i^\beta} \end{pmatrix} = \begin{pmatrix} \sum_k \boldsymbol{\Omega}_{ik} \frac{P_k}{d_k^2 T_k} \\ 0 \\ \frac{1}{T_i} \\ \frac{\mathbf{F}_i^\beta}{T_i} \end{pmatrix}, \quad (4.11)$$

where we have introduced the following vector that depends only on the position of the particles

$$\boldsymbol{\Omega}_{ij} = -\frac{\partial d_j}{\partial \mathbf{r}_i} = -\left[\omega_{ij} + \delta_{ij} \sum_k \omega_{ik} \right] \quad (4.12)$$

where

$$\overline{\omega}_{ij} = -W'(r_{ij}) \mathbf{e}_{ij}. \quad (4.13)$$

Here, the prime denotes the derivative and $\mathbf{e}_{ij} = \frac{\mathbf{r}_i - \mathbf{r}_j}{|\mathbf{r}_i - \mathbf{r}_j|}$ is the unit vector joining particles i, j .

The temperature appearing in Eq. (4.11) is given by the derivative of the entropy (4.4) with respect to the energy, this is,

$$\frac{1}{T} = \frac{\partial S(E, \mathbf{Q})}{\partial E} = \frac{1}{T^s(E)} + \mathcal{O}(1/N^s). \quad (4.14)$$

The temperature is given, therefore, by the solvent temperature, because we are neglecting terms that are inversely proportional to the size of the fluid particles.

The pressure P_k of the fluid particle k is given by the usual thermodynamic definition

$$\frac{P}{T} = \frac{\partial S(E, \mathbf{Q})}{\partial \mathcal{V}}. \quad (4.15)$$

By taking the volume derivative of (4.4) we obtain

$$P = P^s + k_B T^s n^d, \quad (4.16)$$

where P^s is the solvent pressure and the last term is the osmotic pressure of the dumbbells.

Finally, we have introduced in (4.11) the dumbbell force

$$\mathbf{F}_j^\beta = -\frac{\partial V^d(\mathbf{Q}_j^\beta)}{\partial \mathbf{Q}_j^\beta}. \quad (4.17)$$

The physics that we want to introduce in this model can be summarised in rather simple terms. The fluid solvent moves hydrodynamically and a fixed number of dumbbells N_i^d are transported by each fluid particle in its overall motion. If the fluid is in an extensional state, the elongation vector \mathbf{Q}_i^α of the dumbbell α within the i -th fluid particle should increase, as if it both ends of the dumbbell were ‘‘anchored’’ in the flow field. To this elongation due to the flow field there is an opposite relaxation effect due to the underlying spring that tries to reduce as much as possible the magnitude of \mathbf{Q}_i . Our aim in the next sections is to translate in mathematical terms this physical picture.

4.5 Reversible part of the dynamics

In this section, we formulate the reversible part of the dynamics for the set of variables x . According to GENERIC, the reversible part of the dynamics represents purely kinematic effects on the evolution of the variables and it is given by (see Eq. (A.1) in the appendix A)

$$\dot{x}|_{\text{rev}} = L \frac{\partial E}{\partial x}, \quad (4.18)$$

where L is an antisymmetric matrix. We wish that the reversible part of the dynamics produces the following equations of motion for the positions of the fluid particles

$$\dot{\mathbf{r}}_i = \mathbf{v}_i. \quad (4.19)$$

The simplest non-trivial reversible part $L \frac{\partial}{\partial x} E$ that produces the above Eq. (4.19) has the following form

$$\begin{pmatrix} \dot{\mathbf{r}}_i \\ \dot{\mathbf{v}}_i \\ \dot{E}_i \\ \dot{\mathbf{Q}}_i^\alpha \end{pmatrix}_{\text{rev}} = \sum_j \mathbf{L}_{ij} \begin{pmatrix} \mathbf{0} \\ m\mathbf{v}_j \\ 1 \\ 0 \end{pmatrix}, \quad (4.20)$$

where the block \mathbf{L}_{ij} has the structure

$$\mathbf{L}_{ij} = \frac{1}{m} \begin{pmatrix} \mathbf{0} & \mathbf{1}\delta_{ij} & \mathbf{0} & \mathbf{0} \\ -\mathbf{1}\delta_{ij} & \mathbf{0} & \Delta_{ij} & \Lambda_{i\beta_j} \\ \mathbf{0} & -\Delta_{ji} & 0 & \mathbf{0} \\ \mathbf{0} & -\Lambda_{j\alpha_i}^T & \mathbf{0} & \mathbf{0} \end{pmatrix}. \quad (4.21)$$

Note that in order to have antisymmetry of L , we must have $\mathbf{L}_{ij} = \mathbf{L}_{ji}^T$ where the superscript T means matrix transposition. The first row of \mathbf{L}_{ij} ensures the equation of motion (4.19). The first column is fixed by antisymmetry of L . We have set to zero the right inferior block in order to satisfy the degeneracy condition $L \frac{\partial}{\partial x} S = 0$ in Eq. (A.2) in Appendix A. The only non-trivial part of this degeneracy condition becomes, after the matrix multiplication of (4.21) with (4.11),

$$-\sum_j \Omega_{ij} \frac{P_j}{d_j^2 T_j} + \Delta_{ij} \frac{1}{T_j} + \sum_{\beta_j} \Lambda_{i\beta_j} \cdot \frac{\mathbf{F}_j^\beta}{T_j} = 0. \quad (4.22)$$

The simplest choice for Δ_{ij} that satisfies Eq. (4.22) is

$$\Delta_{ij} = \Omega_{ij} \frac{P_j}{d_j^2} - \sum_{\beta} \Lambda_{i\beta_j} \cdot \mathbf{F}_j^\beta. \quad (4.23)$$

The final reversible part of the dynamics will be

$$\begin{aligned} \dot{\mathbf{r}}_i|_{\text{rev}} &= \mathbf{v}_i \\ m\dot{\mathbf{v}}_i|_{\text{rev}} &= \sum_j \Delta_{ij} \\ \dot{E}_i|_{\text{rev}} &= -\sum_j \Delta_{ji} \cdot \mathbf{v}_j \\ \dot{\mathbf{Q}}_i^\alpha|_{\text{rev}} &= -\sum_j \Lambda_{j\alpha_i}^T \cdot \mathbf{v}_j. \end{aligned} \quad (4.24)$$

Let us turn, now, to the specification of $\mathbf{\Lambda}_{ij}$ by requiring a particular motion for the vector \mathbf{Q}_i due to the advection of the fluid. From a continuum point of view, an arbitrary vector \mathbf{A} is advected under a velocity field $\mathbf{v}(\mathbf{r})$ according to

$$\dot{\mathbf{A}} = \mathbf{A} \cdot \nabla \mathbf{v}(\mathbf{r}), \quad (4.25)$$

where the dot stands for the substantial derivative (Eq. (E.3) in Appendix E). The physical picture is that the vector \mathbf{A} has its both ends “anchored” in the fluid, as shown heuristically in Appendix C. We want that the elastic vector \mathbf{Q}_i^α evolves in a similar way. We need, therefore, the gradient of the velocity field at the point where particle i is. Following the SPH philosophy, we interpolate the velocity field according to

$$\mathbf{v}(\mathbf{r}) = \frac{\sum_j W(\mathbf{r} - \mathbf{r}_j) \mathbf{v}_j}{\sum_j W(\mathbf{r} - \mathbf{r}_j)}. \quad (4.26)$$

By taking the gradient of this expression we obtain

$$\nabla \mathbf{v}(\mathbf{r}) = \frac{\sum_j \nabla W(\mathbf{r} - \mathbf{r}_j) \mathbf{v}_j}{\sum_j W(\mathbf{r} - \mathbf{r}_j)} - \mathbf{v}(\mathbf{r}) \frac{\sum_j \nabla W(\mathbf{r} - \mathbf{r}_j)}{\sum_j W(\mathbf{r} - \mathbf{r}_j)}. \quad (4.27)$$

Therefore, at particle i we have the approximate expression for the gradient of the velocity field

$$\begin{aligned} \nabla \mathbf{v}(\mathbf{r}_i) &= \frac{\sum_j \nabla W(\mathbf{r}_i - \mathbf{r}_j) \mathbf{v}_j}{d_i} - \mathbf{v}(\mathbf{r}_i) \frac{\sum_j \nabla W(\mathbf{r}_i - \mathbf{r}_j)}{d_i} \\ &\approx \frac{1}{d_i} \sum_j \omega_{ij} \mathbf{v}_{ij}, \end{aligned} \quad (4.28)$$

where $\mathbf{v}_{ij} = \mathbf{v}_i - \mathbf{v}_j$ and ω_{ij} is defined in Eq. (4.13). Therefore, the continuum advection equation (4.25) becomes the discrete equation for the kinematic motion of \mathbf{Q}_i^α

$$\dot{\mathbf{Q}}_i^\alpha = \frac{\mathbf{Q}_i^\alpha}{d_i} \cdot \sum_j \omega_{ij} \mathbf{v}_{ij}. \quad (4.29)$$

By comparing Eq. (4.29) with the last equation in (4.24) we obtain the explicit form for the matrix $-\mathbf{\Lambda}_{ji}^T$, i.e.

$$\begin{aligned} -\mathbf{\Lambda}_{j\alpha i}^T &= \frac{\mathbf{Q}_i^\alpha}{d_i} \cdot \left[-\omega_{ij} + \delta_{ij} \sum_k \omega_{ik} \right] \mathbf{1} \\ \mathbf{\Lambda}_{i\beta j} &= -\frac{\mathbf{Q}_j^\beta}{d_j} \cdot \left[\omega_{ij} + \delta_{ij} \sum_k \omega_{ik} \right] \mathbf{1} \\ &= -\frac{\mathbf{Q}_j^\beta}{d_j} \cdot \mathbf{\Omega}_{ij} \mathbf{1}. \end{aligned} \quad (4.30)$$

With this particular form of the matrix Λ_{ij} we can write the vector Δ_{ij} in Eq. (4.23) as

$$\Delta_{ij} = \frac{1}{d_j^2} \Omega_{ij} \cdot \left[P_j \mathbf{1} + d_j \sum_{\beta} \mathbf{F}_j^{\beta} \mathbf{Q}_j^{\beta} \right]. \quad (4.31)$$

The term in brackets can be understood as the reversible part of the stress tensor of particle j , i.e,

$$\Pi_j = P_j \mathbf{1} + d_j \sum_{\beta} \mathbf{F}_j^{\beta} \mathbf{Q}_j^{\beta}. \quad (4.32)$$

This stress tensor includes an isotropic component given by pressure in Eq. (4.16) and a non-diagonal part. Substitution of (4.12) and (4.32) into Eqs. (4.24) leads to the final *reversible* part of the dynamics for the viscoelastic model

$$\begin{aligned} \dot{\mathbf{r}}_i|_{\text{rev}} &= \mathbf{v}_i \\ m \dot{\mathbf{v}}_i|_{\text{rev}} &= \sum_j \left[\frac{\Pi_i}{d_i^2} + \frac{\Pi_j}{d_j^2} \right] \cdot \omega_{ij} \\ \dot{E}_i|_{\text{rev}} &= -\frac{\Pi_i}{d_i^2} : \sum_j \omega_{ij} \mathbf{v}_{ij} \\ \dot{\mathbf{Q}}_i^{\alpha}|_{\text{rev}} &= \frac{\mathbf{Q}_i^{\alpha}}{d_i} \cdot \sum_j \omega_{ij} \mathbf{v}_{ij}. \end{aligned} \quad (4.33)$$

These equations (4.33) conserve total energy (due to the antisymmetry of L) and leave the entropy unchanged (due to the degeneracy $L \frac{\partial S}{\partial x} = 0$). They also conserve total momentum $\mathbf{P}(x) = \sum_i m \mathbf{v}_i$ due to the symmetries under exchange of the indices i, j in the momentum equation.

Let us summarise now the line of reasoning followed in this section. We have assumed a particular equation of motion for \mathbf{Q}_i^{α} in which this vector is “anchored” in the solvent. This implies a particular form for the matrix $\Lambda_{i\beta_j}$ in Eq. (4.30). The conservation of energy implied by the antisymmetry of the matrix L imposes that this matrix $\Lambda_{i\beta_j}$ should appear in an additional term in the momentum equation. The particular form of this term is dictated by the degeneracy condition $L \frac{\partial S}{\partial x} = 0$, Eq. (4.23) which ensures that there is no entropy production due to the reversible part of the dynamics. As a result, we have been able to identify a reversible part of the stress tensor, which depends on the configuration \mathbf{Q}_i^{α} of the dumbbells. It is quite remarkable that the small physical input given by the “anchoring” of \mathbf{Q}_i^{α} translates, through the GENERIC formalism, into a very specific form for the stress tensor. Finally, the energy equation in (4.33) describes how the mechanical work is transformed into internal energy in a reversible way.

4.6 Irreversible part of the dynamics

As shown in Appendix A, in order to derive the irreversible part of the dynamics of the viscoelastic non-isothermal particle model, a very useful route is to *first* postulate

the thermal noises $d\tilde{x}$ and *afterwards* compute the dissipative matrix M through the fluctuation-dissipation theorem,

$$M = \frac{d\tilde{x}d\tilde{x}^T}{2k_B dt}. \quad (4.34)$$

This procedure ensures that M defined through Eq. (4.34) is automatically symmetric and positive semi-definite.

We postulate the following form for the thermal noises $d\tilde{x} = \{\mathbf{0}, d\tilde{\mathbf{v}}_i, d\tilde{E}_i, d\tilde{\mathbf{Q}}_i^\alpha\}$. Note that we do not assume any thermal noise for the position of the fluid particles, as we want to respect the equation of motion $\dot{\mathbf{r}}_i = \mathbf{v}_i$. In Ref. [73] it has discussed how to introduce the thermal noises $d\tilde{\mathbf{v}}_i, d\tilde{E}_i$ in order to recover a matrix M which produces an irreversible part of the dynamics that can be understood as a smoothed particle hydrodynamics discretisation of the irreversible terms of the Navier-Stokes equations. We only have to postulate now the noise terms $d\tilde{\mathbf{Q}}_i^\alpha$. We discuss in the Appendix D that a reasonable assumption for the stochastic force on \mathbf{Q}_i^α is given by

$$d\tilde{\mathbf{Q}}_i^\alpha = \left(4 \frac{k_B T_i}{6\pi\eta a}\right)^{1/2} d\mathbf{U}_{\alpha_i}, \quad (4.35)$$

where $d\mathbf{U}_{\alpha_i}$ is an independent increment of the Wiener process, satisfying

$$d\mathbf{U}_{\alpha_i} d\mathbf{U}_{\beta_j} = \delta_{\alpha_i \beta_j} \mathbf{1} dt. \quad (4.36)$$

We recognise in the prefactor of (4.35) the diffusion coefficient of the beads of radius a given by the Stokes-Einstein relation. We will assume that the noise $d\tilde{\mathbf{Q}}_i^\alpha$ are statistically independent of $d\tilde{\mathbf{v}}_i, d\tilde{E}_i$.

According to Eq. (4.34), the matrix $M \rightarrow \mathbf{M}_{ij}$ is given by

$$\begin{pmatrix} \mathbf{0} & \mathbf{0} & \mathbf{0} & \mathbf{0} \\ \mathbf{0} & \frac{d\tilde{\mathbf{v}}_i d\tilde{\mathbf{v}}_j^T}{2k_B dt} & \frac{d\tilde{\mathbf{v}}_i d\tilde{E}_j}{2k_B dt} & \mathbf{0} \\ \mathbf{0} & \frac{d\tilde{E}_i d\tilde{\mathbf{v}}_j^T}{2k_B dt} & \frac{d\tilde{E}_i d\tilde{E}_j}{2k_B dt} & \mathbf{0} \\ \mathbf{0} & \mathbf{0} & \mathbf{0} & \frac{d\tilde{\mathbf{Q}}_i^\alpha d\tilde{\mathbf{Q}}_j^\beta}{2k_B dt} \end{pmatrix}. \quad (4.37)$$

The central diagonal block has been computed in Ref. [73] and we have to compute only the last diagonal element, which is

$$\frac{d\tilde{\mathbf{Q}}_i^\alpha d\tilde{\mathbf{Q}}_j^\beta}{2k_B dt} = \frac{2T_i}{\zeta} \delta_{\alpha\beta} \delta_{ij} \mathbf{1}. \quad (4.38)$$

Now we are in position to write the deterministic irreversible part of the dynamics

$\dot{x}|_{\text{irr}} = M \cdot \frac{\partial S}{\partial x}$ which, after use of Eq. (4.11) for the derivative of the entropy, becomes

$$\begin{pmatrix} \dot{r}_i \\ \dot{\mathbf{v}}_i \\ \dot{E}_i \\ \dot{\mathbf{Q}}_i^\alpha \end{pmatrix} \Big|_{\text{irr}} = \sum_j \mathbf{M}_{ij} \begin{pmatrix} \sum_k \Omega_{jk} \frac{P_k}{d_k^2 T_k} \\ 0 \\ \frac{1}{T_j} \\ \frac{\mathbf{F}_j^\beta}{T_j} \end{pmatrix}, \quad (4.39)$$

By collecting the results of [73] (once we neglect, for simplicity, the bulk viscosity) for the diagonal blocks of \mathbf{M}_{ij} together with (4.38) we obtain the following irreversible part of the dynamics

$$\begin{aligned} \dot{\mathbf{r}}_i \Big|_{\text{irr}} &= 0 \\ m \dot{\mathbf{v}}_i \Big|_{\text{irr}} &= -\frac{5\eta}{3} \sum_j \frac{F_{ij}}{d_i d_j} (\mathbf{v}_{ij} + (\mathbf{e}_{ij} \cdot \mathbf{v}_{ij}) \mathbf{e}_{ij}) \\ \dot{E}_i \Big|_{\text{irr}} &= \frac{1}{2} \frac{5\eta}{3} \sum_j \frac{F_{ij}}{d_i d_j} (\mathbf{v}_{ij}^2 + (\mathbf{v}_{ij} \cdot \mathbf{e}_{ij})^2) \\ &\quad - 2\kappa \sum_j \frac{F_{ij}}{d_i d_j} T_{ij} \\ \dot{\mathbf{Q}}_i^\alpha \Big|_{\text{irr}} &= \frac{2}{\zeta} \mathbf{F}_i^\alpha, \end{aligned} \quad (4.40)$$

where η is the shear viscosity of the solvent and κ the thermal conductivity. The geometrical factor F_{ij} is given by

$$F_{ij} = -\frac{W'(r_{ij})}{r_{ij}}. \quad (4.41)$$

Note that concerning the irreversible part of the dynamics, the solvent and dumbbells are completely uncoupled and, therefore, the solvent irreversible dynamics is identical to that in Ref. [73].

By collecting the reversible part of the dynamics Eqs. (4.33) and the irreversible part of the dynamics Eqs. (4.40) we obtain the following set of *deterministic* equations, corresponding to Eq. (A.1)

$$\begin{aligned}
\dot{\mathbf{r}}_i &= \mathbf{v}_i \\
m\dot{\mathbf{v}}_i &= \sum_j \left[\frac{\mathbf{\Pi}_i}{d_i^2} + \frac{\mathbf{\Pi}_j}{d_j^2} \right] \cdot \omega_{ij} \\
&\quad - \frac{5\eta}{3} \sum_j \frac{F_{ij}}{d_i d_j} (\mathbf{v}_{ij} + (\mathbf{e}_{ij} \cdot \mathbf{v}_{ij}) \mathbf{e}_{ij}) \\
\dot{E}_i &= -\frac{\mathbf{\Pi}_i}{d_i^2} : \sum_j \omega_{ij} \mathbf{v}_{ij} \\
&\quad + \frac{1}{2} \frac{5\eta}{3} \sum_j \frac{F_{ij}}{d_i d_j} (\mathbf{v}_{ij}^2 + (\mathbf{v}_{ij} \cdot \mathbf{e}_{ij})^2) \\
&\quad - 2\kappa \sum_j \frac{F_{ij}}{d_i d_j} T_{ij} \\
\dot{\mathbf{Q}}_i^\alpha &= \frac{\mathbf{Q}_i^\alpha}{d_i} \cdot \sum_j \omega_{ij} \mathbf{v}_{ij} + \frac{2}{\zeta} \mathbf{F}_i^\alpha.
\end{aligned} \tag{4.42}$$

This set of equations have the very appealing features of conserving energy and total momentum $\mathbf{P} = \sum_i m\mathbf{v}_i$, and leading to a positive production of entropy $\dot{S}(x) \geq 0$.

The evolution of \mathbf{r}_i , \mathbf{v}_i , E_i is identical to that of a simple fluid without dumbbells, as given in Ref. [73], except for the additional dumbbell contribution to the stress tensor in Eq. (4.32). Apart from that, we recognise in these equations the different physical processes involved. In the momentum equation, viscous forces proportional to the viscosity try to reduce velocity differences between fluid particles. In the energy equation, a viscous heating term proportional to the shear viscosity describes how the kinetic energy which is dissipated by the friction forces leads to an increase of internal energy of the particles. Also in this energy equation, the heat conduction term, with overall magnitude given by the thermal conductivity of the solvent, tries to reduce temperature differences between fluid particles.

Finally, the last set of equations governs the dynamics of the elongation of every single dumbbell in the solution. Let us discuss with some detail this set of equations for the simplest case of Hookean dumbbells. For Hookean dumbbells $\mathbf{F}_i^\alpha = -H\mathbf{Q}_i^\alpha$, where H is the spring constant, and the last irreversible term describes an exponential decay governed by a time scale given by $\zeta/2H$. Given an initial elongation of every dumbbell in each fluid particle, this term relaxes it towards a zero elongation. The advective term cannot do anything against this relaxation and, actually, $\mathbf{Q}_i^\alpha = 0$ is the final solution of the equations for the dumbbell elongation. Apparently, we have derived a very stupid model in which the dumbbells just relax towards zero elongations, the dumbbell contribution to the stress tensor vanishes, and we are back to the model for a Newtonian fluid.

Of course, an essential element is lacking in the above set of equations, which is the presence of thermal fluctuations. Thermal fluctuations are the crucial bit that renders the present model sensible and useful for the simulation of polymer solutions. The way

to proceed is to formulate the GENERIC stochastic differential equations as shown in Appendix A. This has been done for the Newtonian model in [73] and leads to a proper thermodynamic version of the original Dissipative Particle Dynamics model.

For the viscoelastic model presented here, the set of stochastic equations are [74].

$$\begin{aligned}
d\mathbf{r}_i &= \mathbf{v}_i dt \\
md\mathbf{v}_i &= \sum_j \left[\frac{\boldsymbol{\Pi}_i}{d_i^2} + \frac{\boldsymbol{\Pi}_j}{d_j^2} \right] \cdot \omega_{ij} dt \\
&\quad - \frac{5\eta}{3} \sum_j \frac{F_{ij}}{d_i d_j} (\mathbf{v}_{ij} + (\mathbf{e}_{ij} \cdot \mathbf{v}_{ij}) \mathbf{e}_{ij}) dt + k_B \left[\frac{\partial \mathbf{M}}{\partial x} \right]_{\mathbf{v},i} + md\tilde{\mathbf{v}}_i \\
dE_i &= -\frac{\boldsymbol{\Pi}_i}{d_i^2} : \sum_j \omega_{ij} \mathbf{v}_{ij} dt \\
&\quad + \frac{1}{2} \frac{5\eta}{3} \sum_j \frac{F_{ij}}{d_i d_j} (\mathbf{v}_{ij}^2 + (\mathbf{v}_{ij} \cdot \mathbf{e}_{ij})^2) dt \\
&\quad - 2\kappa \sum_j \frac{F_{ij}}{d_i d_j} T_{ij} dt + k_B \left[\frac{\partial \mathbf{M}}{\partial x} \right]_{E,i} + d\tilde{E}_i \\
d\mathbf{Q}_i^\alpha &= \frac{\mathbf{Q}_i^\alpha}{d_i} \cdot \sum_j \omega_{ij} \mathbf{v}_{ij} dt - \frac{2H}{\zeta} \mathbf{Q}_i^\alpha dt + d\tilde{\mathbf{Q}}_i^\alpha.
\end{aligned} \tag{4.43}$$

Let us notice that the inclusion of the stochastic terms $d\tilde{\mathbf{v}}_i$ and $d\tilde{E}_i$ requires, following the GENERIC formalism overviewed in appendix 1, to consider additional terms in the equation which are proportional to $\partial \mathbf{M} / \partial x$. This ensures that the two nice properties mentioned above, conservation of energy and positive production of entropy, continue to remain valid also for the stochastic set of equations. An explicit form for the terms appearing in the momentum and energy equations involves the following sums over the particles

$$\left[\frac{\partial \mathbf{M}}{\partial x} \right]_{\mathbf{v},i} = \sum_j \left(\frac{\partial}{\partial \mathbf{v}_j} \frac{d\tilde{\mathbf{v}}_i d\tilde{\mathbf{v}}_j^T}{2k_B dt} + \frac{\partial}{\partial E_j} \frac{d\tilde{\mathbf{v}}_i d\tilde{\mathbf{E}}_j}{2k_B dt} \right) \tag{4.44}$$

and

$$\left[\frac{\partial \mathbf{M}}{\partial x} \right]_{E,i} = \sum_j \left(\frac{\partial}{\partial \mathbf{v}_j} \frac{d\tilde{E}_i d\tilde{\mathbf{v}}_j^T}{2k_B dt} + \frac{\partial}{\partial E_j} \frac{d\tilde{E}_i d\tilde{E}_j}{2k_B dt} \right) \tag{4.45}$$

which has been evaluated in detail in [73].

Concerning the lack of a correspondent term in the equation for the dumbbells elongation, it is clear that the specific form of the noise which we choosed in eq.(4.38), implies identically $\partial \mathbf{M}_{ij} / \partial \mathbf{Q}_i = 0$. The stochastic set of equations (4.43) should be used in place of the deterministic ones, eq.(4.42), if the thermal fluctuations in the hydrodynamic variables play a crucial role in the physical problem.

A particularly interesting feature of this fluid particle model is that thermal fluctuations depend on the size of the fluid particles, in accordance with usual concepts of equilibrium statistical mechanics. Therefore, for large enough fluid particles, the thermal fluctuations in the momentum and energy equation can be neglected. Of course, this is consistent with the fact that in order to simulate a basket ball in a swimming pool we do not introduce thermal fluctuations in the description whereas if we want to simulate a micron sized colloidal particle we will necessarily need to introduce thermal fluctuations. The essential physical reason for the dependence of the thermal fluctuations on the size of the fluid particle is that the momentum and energy are extensive quantities.

Whereas thermal fluctuations can be neglected in the final stochastic equations for the momentum and energy, they cannot be neglected at all for the dynamics of the dumbbell elongation. The dumbbell elongation is not an extensive variable, it is rather a mesoscopic variable for which the fluctuations are an important component of its full dynamics. The effect of the thermal fluctuations in the dynamics of the elongation variable is quite dramatic. Although the dumbbells want to relax towards zero elongation, the thermal noise guarantees a permanent kick-off this state of zero elongation. This slight deviation from zero is sufficient for the convective term in the elongation equation in Eq. (4.42) to “drag” the ends of the dumbbell apart. In a steady shear flow, for example, the system will reach a stationary situation where, although the elongation of each dumbbell is zero on average, the resulting distribution is not isotropic, leading to a non-zero contribution to the stress tensor (see section 4.8).

For the numerical results presented in this chapter we will assume to simulate fluid particle whose size is so large that we can neglect thermal fluctuations in the momentum and energy equations. The final set of stochastic equations reads therefore

$$\begin{aligned}
d\mathbf{r}_i &= \mathbf{v}_i dt \\
md\mathbf{v}_i &= \sum_j \left[\frac{\mathbf{\Pi}_i}{d_i^2} + \frac{\mathbf{\Pi}_j}{d_j^2} \right] \cdot \omega_{ij} dt \\
&\quad - \frac{5\eta}{3} \sum_j \frac{F_{ij}}{d_i d_j} (\mathbf{v}_{ij} + (\mathbf{e}_{ij} \cdot \mathbf{v}_{ij}) \mathbf{e}_{ij}) dt \\
dE_i &= -\frac{\mathbf{\Pi}_i}{d_i^2} : \sum_j \omega_{ij} \mathbf{v}_{ij} dt \\
&\quad + \frac{1}{2} \frac{5\eta}{3} \sum_j \frac{F_{ij}}{d_i d_j} (\mathbf{v}_{ij}^2 + (\mathbf{v}_{ij} \cdot \mathbf{e}_{ij})^2) dt \\
&\quad - 2\kappa \sum_j \frac{F_{ij}}{d_i d_j} T_{ij} dt \\
d\mathbf{Q}_i^\alpha &= \frac{\mathbf{Q}_i^\alpha}{d_i} \cdot \sum_j \omega_{ij} \mathbf{v}_{ij} dt - \frac{2H}{\zeta} \mathbf{Q}_i^\alpha dt + d\tilde{\mathbf{Q}}_i^\alpha.
\end{aligned} \tag{4.46}$$

Of course, due to the coupling between equations, the full set of equations is stochas-

tic even though there is only one noise source $d\tilde{\mathbf{Q}}_i^\alpha$. It may appear odd that having neglected thermal fluctuations in the momentum and energy equations, the equations for these variables still retain a stochastic character. However, we should remark that what we have neglected are spontaneous thermal fluctuations as they appear in the Landau-Lifshitz theory of fluctuating hydrodynamics. Its physical origin is the random interchange of solvent molecules between fluid particles, and these fluctuations are small as compared with the total amount of momentum or energy in the fluid particle. However, the fluctuations in the \mathbf{Q}_i^α variables have an *indirect* effect on the momentum and energy variables through the coupling via the stress tensor. The importance of this indirect coupling depends, of course, on the concentration of polymer molecules and the strength of the springs, and can make a crucial contribution to the dynamic behaviour of the fluid.

4.7 Polymer diffusivity

The model governed by Eqs. (4.46) describes the dynamics of every single dumbbell in the system. This approach is similar to CONNFESSIT [11], [85], where a stochastic simulation of the dumbbells is coupled with a numerical solution of the fluid flows. Of course, having to keep track of the evolution of every single dumbbell in each fluid particle is an expensive task. Note that, according to the last equation in (4.46), all the dumbbells of a given fluid particle will display essentially the same behaviour, at least in a statistical sense. The dynamics of different dumbbells of the same fluid particle differs only by the initial conditions and the actual sequence of random numbers used for the stochastic term. For this reason, we could focus on a given tagged dumbbell within each fluid particle and assume that the rest of dumbbells of that fluid particle “is doing the same thing”.

In addition, the model presented above has a constant number of dumbbells in every fluid particle. This does not seem to be a very reasonable assumption. After all, if the beads of each dumbbell are subject to thermal fluctuations, then the centre of mass of the dumbbell will suffer also from thermal fluctuations, leading to a diffusion of the centre of mass of the dumbbells within the region of a fluid particle until they cross the fluid particle’s “boundary”. This, eventually, should lead to an interchange of dumbbells between fluid particles. The model in Eqs. (4.46) does not allow for a change in time of the number of dumbbells in a fluid particle.

In order to encompass the possibility of describing polymer diffusion and, at the same time, reduce the number of variables to simulate, we present in this section a new model that differs from the one presented in the previous sections in the variables used to describe the state of the system. Now, each fluid particle will be characterised by its position \mathbf{r}_i , its velocity \mathbf{v}_i , its internal energy E_i , a *unique* vector \mathbf{Q}_i describing the elongation of a statistical representative of the dumbbells, *and* the number of dumbbells N_i^d within the fluid particle. By selecting a single elongation vector for every fluid particle we return to a version of the ten Bosch model which, in turn, is analogous to a Lagrangian version of the Brownian Configuration Field Approach [12]. The Brownian Configuration Field Approach is similar to the CONNFESSIT approach except that only

one suitably correlated elongation variable is kept for each fluid element. The connection between both approaches has been elucidated in Ref. [90] where it is shown that the Brownian Configuration Field approach can be understood as a variance reduction version of the CONNFESSIT approach.

Let us proceed to formulate the equations of motion for this new set of variables, by following the GENERIC strategy again. The total energy $E(x)$ of the system in the new variables is still given by Eq. (4.8) and the total entropy $S(x)$ has the same form as in Eq. (4.9), but now the entropy of a fluid particle is not given by (4.4) but rather it is postulated to be

$$S(E, \mathbf{Q}) = S^s(E) - \frac{N^d V^d(\mathbf{Q})}{T^s(E)} + k_B N^d (1 + \ln n^d \lambda_d^D). \quad (4.47)$$

Despite of its similar notation, the fluid particle entropy postulated in Eq. (4.47) depends on the energy, a *single* variable \mathbf{Q} and the number of dumbbells N^d whereas the fluid particle entropy (4.4) depends on the energy and the N^d elongation variables of each dumbbell in the fluid particle.

The derivatives of the energy and entropy with respect to the new variables are

$$\frac{\partial E}{\partial x} = \begin{pmatrix} \mathbf{0} \\ m\mathbf{v}_i \\ 1 \\ 0 \\ 0 \end{pmatrix}, \quad \frac{\partial S}{\partial x} = \begin{pmatrix} \sum_k \Omega_{jk} \frac{P}{d_k^2 T_k} \\ 0 \\ \frac{1}{T_j} \\ \frac{\mathbf{F}_j}{T_j} \\ -\frac{\mu_j^d}{T_j} \end{pmatrix}, \quad (4.48)$$

where we have introduced the chemical potential through

$$\frac{\mu^d}{T} = -\frac{\partial S}{\partial N^d} = k_B \ln(n^d \lambda_d^D) + \frac{V^d(\mathbf{Q})}{T}. \quad (4.49)$$

Due to the dilute assumption, we expect that the variation of the number of dumbbells does not affect appreciably the mass m of the fluid particle, which is still assumed to be constant. However, it might strongly affect the elastic properties of the fluid particle and for this reason we retain N^d as a variable.

Concerning the dynamics of the new variables, we basically construct a system of GENERIC equations by proposing L and M matrices. As far as the reversible part of the

dynamics is concerned we choose the following L matrix, to be compared with (4.21)

$$\mathbf{L}_{ij} = \frac{1}{m} \begin{pmatrix} \mathbf{0} & \mathbf{1}\delta_{ij} & \mathbf{0} & \mathbf{0} & \mathbf{0} \\ -\mathbf{1}\delta_{ij} & \mathbf{0} & \mathbf{\Delta}_{ij} & \mathbf{\Lambda}_{ij} & \mathbf{0} \\ \mathbf{0} & -\mathbf{\Delta}_{ji} & 0 & \mathbf{0} & 0 \\ \mathbf{0} & -\mathbf{\Lambda}_{ji}^T & \mathbf{0} & \mathbf{0} & \mathbf{0} \\ \mathbf{0} & \mathbf{0} & 0 & \mathbf{0} & 0 \end{pmatrix}. \quad (4.50)$$

This matrix ensures that $\dot{N}_i^d|_{\text{rev}} = 0$, this is, the reversible part of the dynamics does not change the number of dumbbells in each fluid particle. The dumbbells are simply transported by the reversible dynamics. From the argument in appendix C concerning the advection of a vector, the $\mathbf{\Lambda}_{ij}$ element is given by

$$\mathbf{\Lambda}_{ij} = -\frac{\mathbf{Q}_j}{d_j} \cdot \mathbf{\Omega}_{ij} \mathbf{1}, \quad (4.51)$$

and the degeneracy condition $L \frac{\partial S}{\partial x} = 0$ now leads to

$$\mathbf{\Delta}_{ij} = \frac{1}{d_j^2} \mathbf{\Omega}_{ij} \cdot \mathbf{\Pi}_j, \quad (4.52)$$

where the stress tensor of particle j , now takes the form

$$\mathbf{\Pi}_j = P_j \mathbf{1} + d_j N_j^d \mathbf{F}_j \mathbf{Q}_j, \quad (4.53)$$

to be compared with (4.32).

For the irreversible matrix M we now select

$$\begin{pmatrix} \mathbf{0} & \mathbf{0} & \mathbf{0} & \mathbf{0} & \mathbf{0} \\ \mathbf{0} & \frac{d\tilde{\mathbf{v}}_i d\tilde{\mathbf{v}}_j^T}{2k_B dt} & \frac{d\tilde{\mathbf{v}}_i d\tilde{E}_j}{2k_B dt} & \mathbf{0} & \mathbf{0} \\ \mathbf{0} & \frac{d\tilde{E}_i d\tilde{\mathbf{v}}_j^T}{2k_B dt} & \frac{d\tilde{E}_i d\tilde{E}_j}{2k_B dt} & 0 & \mathbf{0} \\ \mathbf{0} & \mathbf{0} & 0 & \frac{d\tilde{\mathbf{Q}}_i d\tilde{\mathbf{Q}}_j}{2k_B dt} & \mathbf{0} \\ \mathbf{0} & \mathbf{0} & \mathbf{0} & \mathbf{0} & \frac{d\tilde{N}_i^d d\tilde{N}_j^d}{2k_B dt} \end{pmatrix}. \quad (4.54)$$

where we have introduced a noise term $d\tilde{N}_i^d$ which is statistically independent of $d\tilde{\mathbf{v}}_i$, $d\tilde{E}_i$, $d\tilde{\mathbf{Q}}_i$. In the discussion in Appendix D we see that the mechanism by which the centre of mass of the dumbbells diffuse is essentially the same as the mechanism by which the elongation \mathbf{Q}_i^α of the dumbbells change, that is, the diffusion of each bead of the dumbbells.

In that respect, one would expect certain correlation between the process by which the number of dumbbells in a region of the fluid changes and the process of change of \mathbf{Q} . However, note that the elementary process by which N_i^d changes is the diffusion of the centre of mass for those dumbbells that are in the “boundary” between two fluid particles. The diffusion of these small number of particles near the boundary should not affect strongly the stochastic change of \mathbf{Q}_j and, for this reason, we assume $d\tilde{N}_i^d$ to be uncorrelated with $d\tilde{\mathbf{Q}}_i$, i.e. $d\tilde{N}_i^d d\tilde{\mathbf{Q}}_j = 0$, leading to the block diagonal form of the matrix M .

Now, concerning the stochastic changes of the number of dumbbells, we identify as the elementary stochastic process by which this number changes the random interchange of dumbbells between fluid particles due to the diffusive nature of the centre of mass of the dumbbells within a fluid particle. The mechanism is essentially the same as that of heat conduction as considered in Ref. [73] and we postulate the matrix term

$$\frac{d\tilde{N}_i^d d\tilde{N}_j^d}{2k_B dt} = \frac{1}{2k_B} \left[\delta_{ij} \sum_k D_{ik}^2 - D_{ij}^2 \right]. \quad (4.55)$$

where $D_{ij} = D_{ji}$. The irreversible evolution of the number of dumbbells will be, therefore,

$$\dot{N}_i^d|_{\text{irr}} = - \sum_j \frac{D_{ij}^2}{2k_B} \left[\frac{\mu_i^d}{T_i} - \frac{\mu_j^d}{T_j} \right]. \quad (4.56)$$

After the discussion in Appendix E, we find that a reasonable functional form for the coefficients D_{ij} is simply

$$D_{ij} = \left[\frac{F_{ij}}{d_i d_j} \frac{2}{\zeta} (T_i n_i^d + T_j n_j^d) \right]^{1/2}. \quad (4.57)$$

In this way, Eq. (4.56) becomes a smoothed particle hydrodynamics discretisation of an advection-diffusion equation.

We have thus completed the formulation of this new model. The equations are simply Eqs. (4.46) with only one elongation variable per fluid particle, the stress tensor given by Eq. (4.53), coupled to the diffusion equation

$$\begin{aligned} dN_i^d &= - \sum_j \left[\frac{F_{ij}}{d_i d_j} \frac{2}{\zeta} (T_i n_i^d + T_j n_j^d) \right]^{1/2} \left[\frac{\mu_i^d}{T_i} - \frac{\mu_j^d}{T_j} \right] dt \\ &+ k_B \left[\frac{\partial \mathbf{M}}{\partial x} \right]_{N^d, i} + d\tilde{N}_i^d. \end{aligned} \quad (4.58)$$

where

$$\begin{aligned}
\left[\frac{\partial \mathbf{M}}{\partial x}\right]_{N^d, i} &= \sum_j \left(\frac{\partial}{\partial N^d_j} \frac{d\tilde{N}_i^d d\tilde{N}_j^d}{2k_B dt} \right) \\
&= \frac{1}{2} \{ T_i d_i \sum_j \left[\sum_k \left(\frac{2F_{ik}}{d_i d_k \zeta} \right)^2 - 2 \left(\frac{2F_{ij}}{d_i^2 \zeta} \right)^2 \right] \right. \\
&\quad \left. + \sum_j \left(\frac{2F_{ij}}{d_i d_j \zeta} \right) T_j d_j \right\}. \tag{4.59}
\end{aligned}$$

This equation conserves the total number of dumbbells $\sum_i \dot{N}_i^d = 0$. The evolution of the number of dumbbells in each fluid particle is governed by the unbalance of dumbbell chemical potentials between neighbouring fluid particles that will produce an exchange of dumbbells between fluid particles. This equation couples with the momentum and energy equations through the stress tensor. Note that the variable N_i^d is extensive and we could neglect the additional stochastic forces in Eq. (4.58) so far as we consider fluid particle whose size is quite large. In this way, we are assuming that even though the suspension is dilute, every fluid particle contains a sufficiently large number of dumbbells for the fluctuations on the number of dumbbells to be negligible. It is of course possible to validate this assumption by explicitly including the thermal noise and assess its effect. For the sake of simplicity, we neglect here the stochastic forces (the last two terms Eq. (4.58)), in on the number of dumbbells.

4.8 Simulation results

In this section, we present simulation results in order to check and validate the present model. As a first step, we will assume that the number of dumbbells within each fluid particle is a constant equal to N_0^d , thus neglecting dumbbell diffusion between fluid particles. We will also assume that the thermal conductivity is very large in such a way that the temperature is already equilibrated to the same T_0 in all the fluid particles. A Hookean dumbbell spring will be assumed here. Although the model permits to study more general situations, the isothermal and constant dumbbell density case allows for a comparison with analytically known predictions for Hookean dumbbells.

The simulated isothermal equations are

$$\begin{aligned}
d\mathbf{r}_i &= \mathbf{v}_i dt \\
d\rho_i &= -\rho_i \sum_j \frac{m}{\rho_j} \mathbf{v}_{ij} \cdot \boldsymbol{\omega}_{ij} dt \\
md\mathbf{v}_i &= \sum_j \left[\frac{\boldsymbol{\Pi}_i}{d_i^2} + \frac{\boldsymbol{\Pi}_j}{d_j^2} \right] \cdot \boldsymbol{\omega}_{ij} dt \\
&\quad - \frac{5\eta_s}{3} \sum_j \frac{F_{ij}}{d_i d_j} (\mathbf{v}_{ij} + (\mathbf{e}_{ij} \cdot \mathbf{v}_{ij}) \mathbf{e}_{ij}) dt \\
d\mathbf{Q}_i &= \frac{\mathbf{Q}_i}{d_i} \cdot \sum_j \boldsymbol{\omega}_{ij} \mathbf{v}_{ij} dt - \frac{2H}{\zeta} \mathbf{Q}_i dt + d\tilde{\mathbf{Q}}_i,
\end{aligned} \tag{4.60}$$

with

$$\boldsymbol{\Pi}_i = (P_i^s + k_B T_0 n_0^d) \mathbf{1} - H n_0^d \mathbf{Q}_i \mathbf{Q}_i, \tag{4.61}$$

where $\rho_i = m d_i$ is the solvent mass density and $n_0^d = N^d/\mathcal{V}$ is the constant dumbbells number density. Note that we evaluate here the density by solving a discretized version of the continuity equation and not like in the simulations presented in chapter 1, by using a summation over the particle (4.1). We select an ideal gas equation of state for the solvent pressure $P_i^s = c_p \rho_i T_0$ where c_p is the specific heat at constant pressure. For the weight function, we have chosen the Lucy function

$$W(r) = c_W (1 + 3r/r_c)(1 - r/r_c)^3, \tag{4.62}$$

where $c_W = 5/\pi r_c^2$ in two dimensions and $c_W = 105/16\pi r_c^3$ in three dimension.

In order to make the previous equations dimensionless, we consider the following basic units: unit of mass m_s (mass of a solvent molecule), unit of length L_0 (box dimension), unit of time $\lambda_H = \xi/4H$ (viscoelastic decay time for Hookean dumbbell model), unit of temperature T_0 . We define a reference velocity in terms of the primary variables as $v_0 = L_0/\lambda_H$. By using these units, we can make the above equations dimensionless (variables with an overline are dimensionless)

$$\begin{aligned}
d\bar{\mathbf{r}}_i &= \bar{\mathbf{v}}_i d\bar{t} \\
d\bar{\rho}_i &= -\bar{\rho}_i \sum_j \frac{\bar{m}}{\bar{\rho}_j} \bar{\mathbf{v}}_{ij} \cdot \bar{\omega}_{ij} d\bar{t} \\
d\bar{\mathbf{v}}_i &= \sum_j \bar{m} \left[\frac{\bar{\boldsymbol{\Pi}}_i}{\bar{\rho}_i^2} + \frac{\bar{\boldsymbol{\Pi}}_j}{\bar{\rho}_j^2} \right] \cdot \bar{\omega}_{ij} d\bar{t} \\
&\quad - C_1 \sum_j \bar{m} \frac{\bar{F}_{ij}}{\bar{\rho}_i \bar{\rho}_j} (\bar{\mathbf{v}}_{ij} + (\mathbf{e}_{ij} \cdot \bar{\mathbf{v}}_{ij}) \mathbf{e}_{ij}) d\bar{t} \\
d\bar{\mathbf{Q}}_i &= \frac{\bar{\mathbf{Q}}_i}{\rho_i} \cdot \sum_j \bar{m} \bar{\omega}_{ij} \mathbf{v}_{ij} d\bar{t} - \frac{1}{2} \bar{\mathbf{Q}}_i d\bar{t} + d\tilde{\mathbf{Q}}_i,
\end{aligned} \tag{4.63}$$

with

$$\begin{aligned}
d\tilde{\mathbf{Q}}_i &= C_2 d\bar{\mathbf{U}}_i \\
\bar{\boldsymbol{\Pi}}_i &= (\bar{P}_i^s + C_3) \mathbf{1} - C_4 \bar{\mathbf{Q}}_i \bar{\mathbf{Q}}_i \\
\bar{P}_i^s &= C_5 \bar{\rho}_i.
\end{aligned} \tag{4.64}$$

Five non-dimensional constants appear in Eqs. (4.63)-(4.64),

$$C_1 = \frac{5\eta_s}{3\rho_0 L_0 v_0} \quad C_2 = \sqrt{\frac{k_B T_0}{H L_0^2}} \tag{4.65}$$

$$C_3 = \frac{N^d k_B T_0}{\rho_0 v_0^5 \lambda_H^3} \quad C_4 = \frac{N^d H}{\rho_0 v_0^3 \lambda_H} \quad C_5 = \frac{c_p T_0}{v_0^2} \tag{4.66}$$

The reference density is $\rho_0 = m_s N^s / L_0^3$. Here m_s represents the mass of a single solvent molecule and N^s the total number of solvent molecules contained in the box. Note that we have the usual dimensions for density, pressure, viscosity, etc. corresponding to 3D systems. On the other hand, we are performing 2D simulations, under the assumption of translationally invariant behaviour in the z-direction.

4.8.1 Theoretical results for Hookean dumbbells

Analytical results for an isothermal Couette flow for Hookean dumbbells are available in the literature [4], and give exact prescriptions for the dependence of the material functions and the stretching of the dumbbells $\langle Q^2 \rangle$ as a function of the shear rate in a steady shear flow. Let us assume a 2D steady shear flow. The Cartesian components of the velocity field are by definition

$$v_x = \dot{\gamma} y \quad v_y = 0, \tag{4.67}$$

where $\dot{\gamma} = \partial v_x / \partial y$ is the shear rate. Let us consider now only the polymeric contribution to the pressure tensor. It can be written in tensorial notation:

$$\tau_{\alpha\beta}^p = k_B T_0 n_0^d \delta_{\alpha\beta} - H n_0^d \mathbf{Q}_\alpha \mathbf{Q}_\beta, \quad (4.68)$$

where the Greek indices indicate the spatial coordinates. For Hookean dumbbells, it can be shown that the stress components and material functions in the final steady state configuration are [4]:

$$\tau_{xy}^p = -n_0^d k_B T_0 \lambda_H \dot{\gamma}, \quad (4.69)$$

$$\tau_{yy}^p - \tau_{xx}^p = 2n_0^d k_B T_0 \lambda_H^2 \dot{\gamma}^2. \quad (4.70)$$

From Eq. (4.69) and Eq. (4.70), we obtain the polymer contribution to the shear viscosity η_p and the first normal stress difference Ψ_1 ,

$$\eta_p = -\frac{\tau_{xy}^p}{\dot{\gamma}} = n_0^d k_B T_0 \lambda_H \quad (4.71)$$

$$\Psi_1 = \frac{\tau_{yy}^p - \tau_{xx}^p}{\dot{\gamma}^2} = 2n_0^d k_B T_0 \lambda_H^2. \quad (4.72)$$

In this Hookean model, all material functions are constant, independent of the shear rate. It is also found that the global dumbbell stretching takes the form (2D):

$$\frac{\langle Q^2 \rangle}{\langle Q_{eq}^2 \rangle} = 1 + (\lambda_H \dot{\gamma})^2. \quad (4.73)$$

This shows that the Hookean dumbbells continue to stretch indefinitely as the shear rate is increased. This characteristic of the dynamics based on the Hookean model is inadequate for the description of realistic polymeric solutions. In fact, it is well-known that the viscosity and first normal stress coefficient should decrease for increasing shear rate instead of remaining constant. The failure of the model is related to the infinite extensibility which is shown in Eq. (4.73). Nevertheless, although this model does not provide an accurate description of a polymeric solution, it allows for exact comparisons with numerical results. More complex models like the FENE model, can be easily taken into account.

4.8.2 Setup of the numerical simulations

In order to produce a uniform stable shear flow, we apply the well-known Lees-Edwards boundary conditions [36]. The periodic image criterion is applied in both spatial directions in order to simulate an infinite periodic medium. In addition, a shear is imposed along the y -axis simply by moving in opposite directions the periodic boxes at the top and the bottom of the central simulation box. Their respective velocities are $\pm v_{box} = \dot{\gamma} L_0$, where $\dot{\gamma}$ is the desired shear rate. Particles crossing the edge at the top of the simulation box are re-inserted at the bottom with the same y -component of the

velocity v_y but with opposite v_x . A linear stable velocity profile corresponding to the equation (4.67) is therefore produced.

The numerical parameters of our simulations are: the reference temperature, chosen to be the typical room temperature $T_0 = 300$ K, the reference time $\lambda_H = 1.0 \times 10^{-6}$ s and the reference length $L_0 = 1.0 \times 10^{-5}$ m which corresponds to the length of the box. The reference velocity is therefore $v_0 = L_0/\lambda_H = 10$ m s $^{-1}$. We choose a value for m_s corresponding to the mass of a water molecule ($m_s = 2.98 \times 10^{-26}$ kg) and total number of solvent molecules $N^s = 3.35 \times 10^{13}$. This gives a solvent density $\rho_0 = 10^3$ kg m $^{-3}$ corresponding to typical values for water under standard conditions.

There are other input parameters which influence the dynamics. The solvent shear viscosity $\eta_s = 10^{-3}$ kg m $^{-1}$ s $^{-1}$. The reference dumbbell number density is defined as $n_0^d = N^d/L_0^3$, where N^d is an arbitrary number corresponding to the total number of dumbbells contained in the simulation box. The viscoelastic behaviour is due to the last term in the stress tensor in Eq. (4.61). This term is proportional to N^d and controls the magnitude of the deviatoric non-Newtonian effects. Indeed, for $N^d = 0$ we recover the Newtonian fluid dynamics. The value of N^d is determined accordingly with all the other parameters in order to obtain a suitable polymeric viscosity consistent with Eq. (4.71). Here we assumed $N^d = 10^8$. With these parameters and by using the formulas (4.71)-(4.72), we obtain the polymeric contribution to the viscosity $\eta_p = 4.142 \times 10^{-4}$ kg m $^{-1}$ s $^{-1}$ and the first normal stress coefficient $\Psi_1 = 8.284 \times 10^{-10}$ kg m $^{-1}$ in S.I. units. Therefore, in our numerical framework, their dimensionless values are $\eta_p = 4.142 \times 10^{-3}$ and $\Psi_1 = 8.284 \times 10^{-3}$. As already noticed, these viscometric functions for a Hookean spring model should be independent on the shear rate. The spring constant H can be determined using the the Stokes-Einstein relation, so that $H = 6\pi\eta_s a/4\lambda_H$, where a is the radius of a bead and λ_H the reference time. Here we chose $a = 4.0 \times 10^{-10}$ m which gives a value of $H = 1.88 \times 10^{-6}$ kg s $^{-2}$. In addition, the equilibrium value for $\langle Q_{eq}^2 \rangle$ in Eq. (4.73) (averaged over all the box domain) for zero shear rate should be equal to $\langle Q_{x,eq}^2 \rangle + \langle Q_{y,eq}^2 \rangle = 2C^2 = 2k_B T_0/H L_0^2 = 4.4 \times 10^{-5}$ in dimensionless units.

In the equation of state c_p is chosen equal to 462 J kg $^{-1}$ K $^{-1}$. As the speed of sound is defined as $c_s = \sqrt{\partial p/\partial \rho} = \sqrt{c_p T_0}$, we obtain a value equal to 372.3 m s $^{-1}$. Its value in reduced units is 37.2 which is almost 10 times bigger than the typical box velocity whose maximum value is 5 (corresponding to the highest shear rate simulated $\dot{\gamma} = 10$). This choice of c_s prevents compressibility effects and retains the divergence-free velocity conditions according to Monaghan [91].

The cutoff radius r_c for the ‘‘smoothed particle’’ is chosen 0.08 in reduced units. From a computational point of view, such a choice of r_c involves nearly 50 neighbours for each ‘smoothed particle’ which is a quite large but necessary number for an accurate estimate of the viscometric functions. Finally, the total number M of simulated fluid particle is 2500.

4.8.3 Numerical results

In this section we present the results of a Couette shear flow experiment. The polymeric viscosity η_p , first normal stress coefficient Ψ_1 and global stretching $\langle Q^2 \rangle$ are extracted from 7 different runs corresponding to different values of the shear rate $\dot{\gamma}$. Finally, we

compare the numerical results with the analytical ones coming from Eqs. (4.69)-(4.73).

Given the homogeneous flow field developed by the boundary conditions, we evaluate the global quantities which we are interested in by taking the average of their local values defined at the position of every fluid particle. For example, $\langle \tau_{\alpha\beta} \rangle = \frac{1}{M} \sum_{i=1}^M \tau_{\alpha\beta}^i$, where M is the number of the simulated SPH particles.

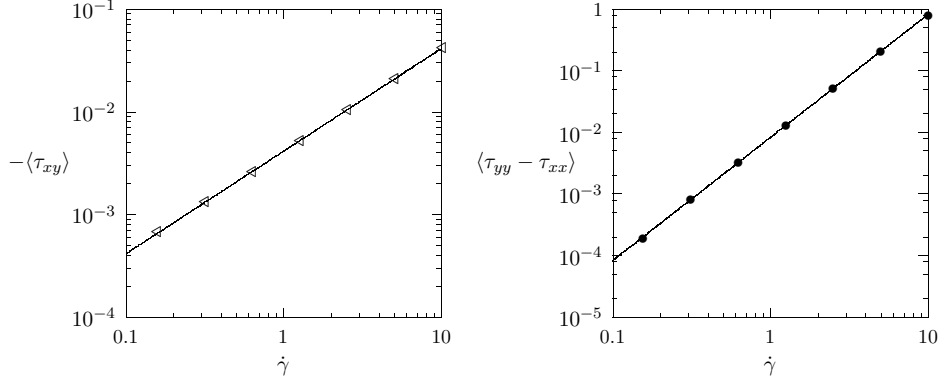


Figure 4.2: Steady-state off-diagonal component of the polymeric dimensionless stress tensor τ_{xy} (\triangle left) and difference between the steady-state diagonal components of the polymeric dimensionless stress tensor $\tau_{yy} - \tau_{xx}$ (\bullet right) as a function of shear rate $\dot{\gamma}$. The solid lines represent the theoretical prediction in Eq. (4.69)- (4.70) .

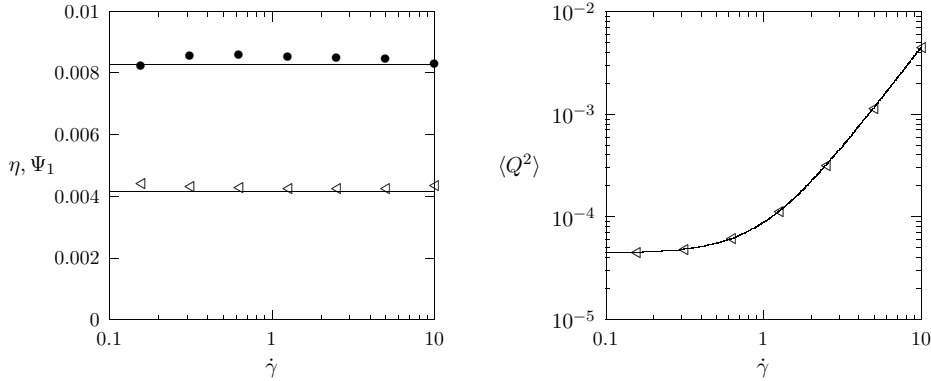


Figure 4.3: Left: Dimensionless polymeric viscosity η_p (\triangle) and first normal stress coefficient ψ_1 (\bullet) versus shear rate $\dot{\gamma}$. The numerical results are compared with the theoretical constant values predicted from Eqs. (4.71), (4.72) in solid lines. Right: Steady-state molecular dimensionless stretching $\langle Q^2 \rangle$ versus shear rate. Triangles are the simulation results and the solid line is the theoretical prediction in Eq. (4.73).

In Fig. 4.8.3 we plot $\langle \tau_{xy} \rangle$ and $\langle \tau_{yy} - \tau_{xx} \rangle$, respectively, as functions of the shear rate. The symbols correspond to the results of the simulations while the solid lines are the theoretical previsions corresponding to equations (4.69)-(4.70). As prescribed, their

values increase respectively linearly and quadratically with $\dot{\gamma}$. The x and y -scale are both logarithmic and cover a range of $\dot{\gamma}$ from about 0.1 to 10 in reduced units.

As already pointed out, the components of the polymeric stress should increase with the shear rate in such a way that the viscosity and the first normal stress coefficient remain constant as prescribed by equations (4.71)- (4.72). In Fig. 4.8.3 we plot η_p and Ψ_1 and compare them with their theoretical constant values. This shows that the agreement is also quantitatively good over all the range of $\dot{\gamma}$ simulated. It must be pointed out that no fit parameters have been used.

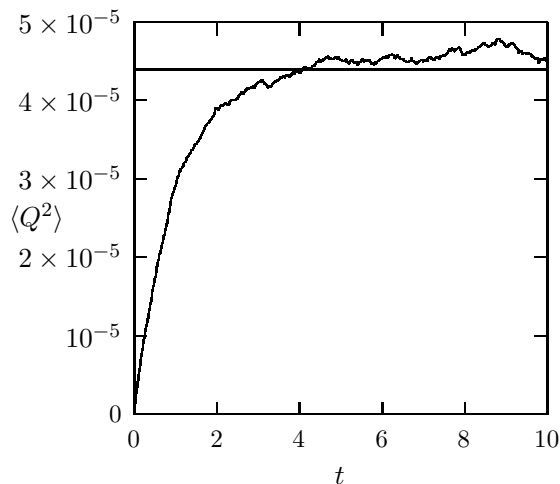


Figure 4.4: Molecular dimensionless stretching growth curve corresponding to a shear rate $\dot{\gamma} = 0.156$. It can be observed that the steady-state value of $\langle Q^2 \rangle$ fluctuates around the equilibrium value corresponding to zero shear rate. This shows that the agreement with the theory is achieved quantitatively also in the small shear rate regime.

Eq. (4.73) shows that the dumbbells continue to stretch as the shear is increased. This is a particular property of the Hookean dumbbell model. In Fig. 4.8.3 we plot the global molecular stretching $\langle Q^2 \rangle$. Even in the global stretching we achieved a very good quantitative agreement with the analytical results. In addition, also the exact output equilibrium value for the average square elongation vector is recovered in the limiting case of small shear rate. In this regime a limiting value is obtained corresponding to the equilibrium (zero shear rate) stretching. This can not be observed in the previous picture because of its smallness compared with the values corresponding to high $\dot{\gamma}$. In the next figure it is shown the temporal evolution of $\langle Q^2 \rangle$ for a shear flow with $\dot{\gamma} = 0.156$. The agreement with the theoretical prevision for $\langle Q_{eq}^2 \rangle$ is clearly visible in Fig. 4.8.3.

Finally, in Fig. 4.5 we present snapshots of the Q -vector configuration at different times and for a fixed shear rate $\dot{\gamma} = 10$. The x and y -axes represent respectively the Q_x and Q_y components of the elongation of the dumbbell representative of every simulated fluid particle. The snapshots correspond to times $t = 0.1, 0.3, 0.6, 1.0, 2.0, 4.0$. As expected, we observe the stretching of Q_x component while in the y -direction the configuration tends to that one of equilibrium at zero shear rate.

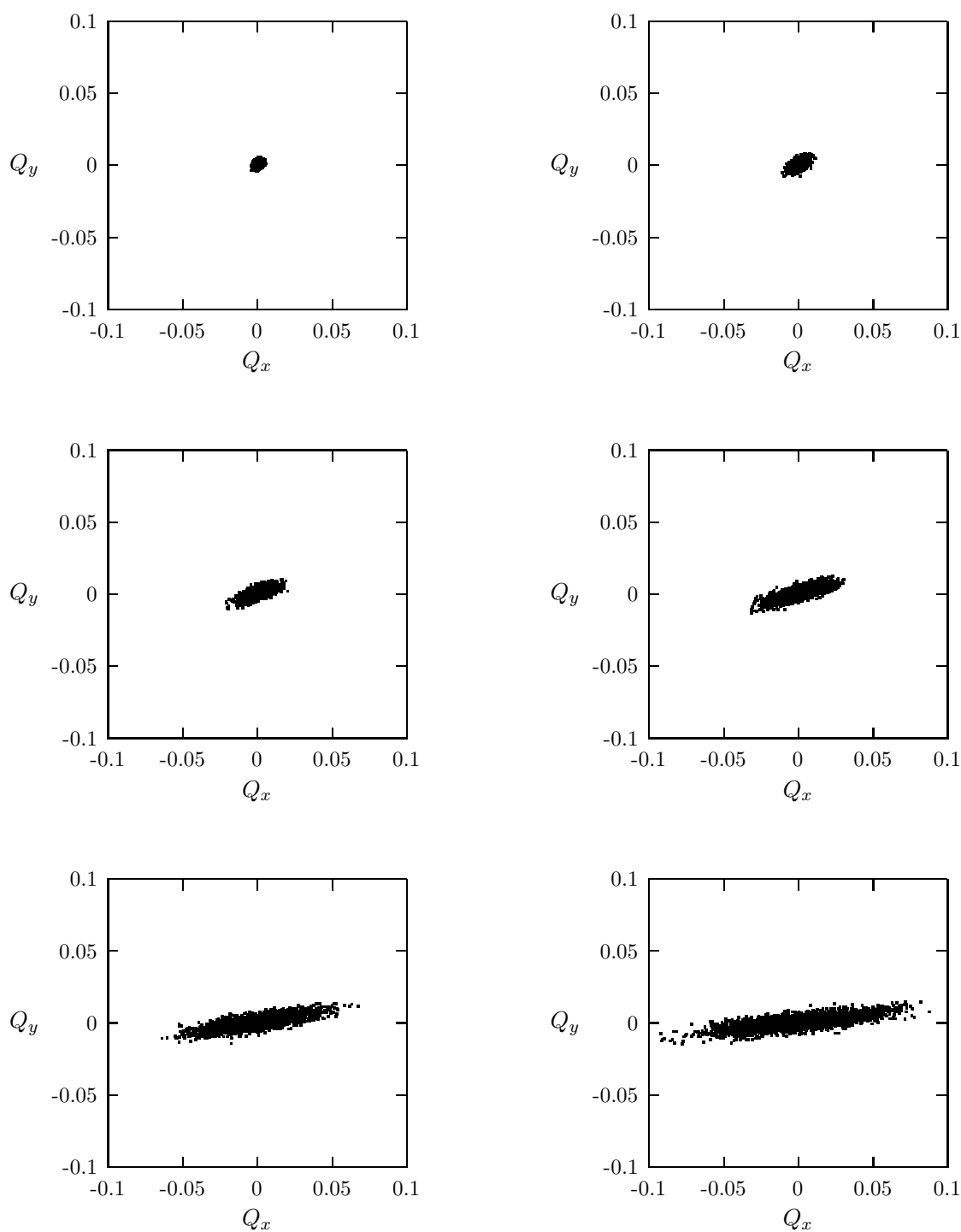


Figure 4.5: The dimensionless elongation of the dumbbell representative of every fluid particle in a start up of the shear flow at times $t = 0.1, 0.3, 0.6, 1.0, 2.0, 4.0$. Initially the dumbbells distribute isotropically but as time proceeds, the distribution becomes more and more anisotropic.

We notice also that at every time the stretching in the x -direction increases, but always preserving the symmetry of the particle distribution around the origin in the Q -plane, that is, on average over all the box the components of the Q -vector are zero.

4.9 Final remarks

Inspired by a Dissipative Particle Dynamics model formulated by ten Bosch [30], we have proposed a fluid particle model for the simulation of dilute polymeric solutions. Special attention has been paid to the thermodynamic consistency of the model, by writing it within the GENERIC framework. Actually, several basic differences between the model presented and that of ten Bosch [30] arise from the thermodynamic consistency of our model. First, our model includes a fluid particle volume variable and, therefore, the conservative forces in the momentum equation are replaced by actual pressure forces. As we have shown in Ref. [73], the conservative forces in the original classic DPD model are not very physical and do not allow to study *arbitrary* equations of state. Second, our model includes an internal energy variable and it allows to study non-isothermal processes. Again, this can be regarded as an improvement over the classic DPD model. Finally, we have introduced the number of dumbbells as an additional variable, which allows to study diffusive processes of dumbbells which are absent in the ten Bosch model.

From a more technical point of view, we observe that our model has a smaller number of parameters and functions than the ten Bosch model. For example, the antisymmetry of L forces the α and β parameters of ten Bosch model to be exactly the same. Also, the solvent parameters are the physical transport coefficients, which are directly given as an input. There is no need to perform a kinetic theory of the model in order to obtain the transport coefficients in terms of the model parameters, as it is done in Ref. [30].

Our approach also puts the ten Bosch model in a conceptual framework that highlights the validity and limitations of the model as a tool for simulating viscoelastic materials. From the microscopic calculation of the entropy and the physical arguments used to derive the equations of motion, it is apparent that this model should provide a good description for *dilute* polymeric solutions. Semi-dilute solutions could perhaps be treated by including excluded volume effects of the dumbbells and mean field interactions between dumbbells using similar ideas as those of van der Waals for simple fluids. Polymer melts cannot be described by our model. A continuum theory for polymer melts in non-isothermal situations has been presented in Ref. [92], which makes use of a conformation tensor for describing the microstructure of the melt. The continuum equations for polymer melts in Ref. [92] could also be discretized in terms of fluid particles with a well-defined underlying physical picture that respects the laws of thermodynamics.

In this chapter, we have presented numerical simulations for isothermal homogeneous shear flow without polymer diffusivity. For reasons of simplicity, we have modelled the polymer molecules with Hookean dumbbells, although more realistic models for polymer molecules can also be considered. Finite extensibility and more complex bead-spring models [4] are easily implemented. The simulation results are preliminary but, nevertheless, reproduce the known theoretical predictions without fitting parameters.

Of course, the potential of the method lies in the possibility of exploring more complex non-isothermal, non-homogeneous, and non-Hookean situations.

A final comment on the connection between our model and the Brownian Configuration Fields (BCF) method is in order. In BCF, there is also only one elastic variable per (Eulerian) computational cell, and the goal is to reduce the noise inherent in the method by using the same sequence of random kicks for all the position over the domain. Then one has one realization of the vector field \mathbf{Q} (and consequently one realization of the polymeric pressure tensor), which are completely correlated over all the space. When the divergence of the stress tensor is evaluated in the momentum equation, it is usually done by a two-points difference discretisation, and, because of the total correlation between tensor fields in different points, the noise is dramatically reduced. In the SPH discretisation of the momentum equation, the gradients are represented by a sum (in order to have an antisymmetric force in the particle index) and not by a difference. Therefore, our method is intrinsically noisy and the level of fluctuations cannot be reduced by the trick in BCF (or we would lose exact momentum conservation). In order to study non-homogeneous flows, the two options are either to use a sufficiently large number of fluid particles in such a way that we can perform spatial averages over many particles underlying the same shear flow or to use a very big number of dumbbells per fluid particle as in the CONNFESSIT approach. The last option represents, from a numerical point of view, a very difficult task because the correspondent algorithm could be potentially very demanding in terms of CPU-time and memory requirements. This topic will be the subject of the next chapter where we will present also a new method able to avoid, at least partially, the computational bottleneck mentioned above.

Chapter 5

Multiscale simulations of viscoelastic flows

In this chapter we consider the problem of a consistent description of complex flows based on a multiscale formulation. As already mentioned in Chapter 2, traditional numerical methods based on the solution of suitable macroscopic constitutive equations, relating viscoelastic stress to history deformation (i.e. Jaumann-Maxwell model), represent an established tool in computational rheology. However, these approaches present some difficulties mostly related to the correctness and accuracy of the model constitutive equation used. Indeed, it is well-known that their derivations from kinetic theory involve a number of unphysical closure approximations which can have a major influence on the final results. In the attempt to solve this problem, new techniques emerged in the last years which couple the macroscopic hydrodynamic scales of the flow with a microscopic consistent evaluation of the viscoelastic stress tensor based on coarse-grained kinetic models. These *micro-macro methods* allow to describe a complex fluid by a multiscale modelling using directly microscopic results. In spite of their physical appealing, it has been early recognized that the correspondent numerical implementations can be very demanding in term of memory and CPU-time resources. The goal of this chapter is to give a general overview of the micro-macro methods recently used in computational rheology, discussing the drawbacks and finally to present a new hybrid technique able to correct some of them at least in some specific case.

The scheme of the chapter is the following: Sec. 5.1 overviews briefly the micro-macro methods, while in sec. 5.2 it is described rigorously the multiscale formalism for the study of dilute polymeric solutions: this is generally based on the solution of a Fokker-Planck equation by using stochastic methods. At this point it will be clear that one of the main issue in micro-macro simulations is represented by the reduction of the memory requirements. This is achieved in a new hybrid method, presented in Sec. 5.3, which splits the stochastic dynamics and the storage of the relevant variables at every time step in such a way to optimise the computer resources. Finally, in Sec. 5.4 numerical results are presented and compared with the traditional methods based on Brownian Dynamics simulations while in Sec. 5.5 possible improvements and applications are discussed.

5.1 Micro-macro methods for complex fluids

Computational fluid dynamics for non-Newtonian flows is to date a well-established field of research which has experienced in the last decades several improvements from both the conceptual and numerical point of view. Finite element methods, finite volumes, boundary elements, smoothed particle dynamics, as that presented in Chapter 3, have been developed able to produce accurate and stable solutions for a wide range of flow fields [3, 95, 96, 50].

These methods, however, rely on the knowledge of an exact constitutive relationship between stress and deformation, which is not available for non-trivial, ‘realistic’ models. Although promising results have been obtained using different closures, the range of their applicability is still unresolved, or severely limited. Focusing on this problem, ten years ago emerged the idea of the CONNFESSIT micro-macro approach (Calculation of Non-Newtonian Flows using Finite Elements and Stochastic Simulation Techniques) [11, 97], further abbreviated as CT in the following. It combines a finite element calculation of the macroscopic flow fields with a microscopic evaluation of the viscoelastic extra stress tensor based on Brownian Dynamics (BD) simulations of polymer molecules. This approach obviously bypasses the need of closed constitutive equations and avoids all problems related to their validity and degree of approximation. Viscoelasticity is introduced in the scheme in an elegant and physically motivated way just by evolving all the polymer variables and then extracting stresses from their micro-configurations. However, in spite of its undoubtedly physical appeal, it has been noticed early that a fully CT simulation is enormously memory and time consuming. In fact, this stochastic technique is intrinsically noisy and, in order to achieve accurate evaluations of the stress tensor in one position over the domain, the level of fluctuations must be drastically reduced by using a very large number of dumbbells. This drawback involves a big amount of memory requirements for every discretizing element, posing many problems in order to make simulations in situations of practical interest, where a very large number of grid points is necessary to discretize all the computational domain and to capture all the relevant length scales of the problem. 3D and/or turbulence simulations coupled with complex boundary conditions are up to now completely far from the numerical capabilities of the present generation of workstations. On the other hand, very recently have been performed fully-developed turbulence simulations in simple channel geometries by using order of million cells discretizing the physical domain and thousands of dumbbells pro cell in order to evaluate the extra stress via BD. To our knowledge, this represents the state-of-the-art large scale parallel stochastic simulations of CT type [98].

In order to avoid this problem modifications have been proposed, such as ‘variance reduced CONNFESSIT’ (VRCT), and ‘Brownian Configuration Fields’ (BCF), both using a manageable number of freedom degrees. They rely on the idea of using suitable fully correlated ensembles of dumbbells. The key point of the VRCT method is the concept of control variables which should have the same fluctuations as the random variable of interest and vanishing averages. When, during a run, the control variable is subtracted from the variable of interest, the average of the latter should not be affected from this operation, but its fluctuation should be considerably reduced. The way by

which such control variables are constructed, i.e. parallel process simulations, has been discussed in [99].

The second approach, Brownian configuration Fields (BCF) [12] relies on the idea of replacing the collection of individual polymer molecules with an ensemble of configuration fields. On every element on the spatial domain is therefore defined only one dumbbell connector. All of them have the same initial conditions and are subjected to same sequence of random kicks during the flow dynamics. This corresponds to one particular realization of the flow field which is completely correlated over all the space. At this point, one should notice that the extra stress tensor appears in the momentum equation under divergence operation. Stresses are calculated from two-points differences between nearby elements. When performing the usual divergence operation a large noise suppression takes place (provided that adjacent elements have very similar flow histories). The connection between the two approaches has been recently clarified further in [90]. A variation of BCF, where time steps are splitted into a BD step followed by a convective step, where the distribution is projected onto an orthogonal polynomial basis has been presented in [114]. We should also mention the Lagrangian Particle Method (LPM) [13, 100, 101], which combines an Eulerian finite element solution of the conservation equations with a Lagrangian computation of the extra-stress tensor by using a certain number of discrete particles convected by the flow. Due to its Lagrangian nature it is not required to keep track of the motion of every dumbbells, as in the first-generation CT, and, at the same time, the intrinsic convective term contained in the $\hat{\text{I}}$ to-stochastic equations is naturally taken into account. LPM simulations have been performed with correlated and uncorrelated ensembles of dumbbells in order to study the effect of the variance reduction on the results. It has been pointed out that the polymer stress results extracted from one particular run with correlated ensembles are much smoother than for fully uncorrelated systems but, by performing many independent runs, they vary a lot from one to the other. These deviations in the results are due to an incomplete realization of the initial configurational distribution when using a finite number of correlated dumbbells. This finding constitutes a major problem emerging when introducing unrealistic correlations in simulations while effectively reducing the number of freedom degrees. Upon increasing the number of simulated dumbbells in each of the ensembles discussed above, the results tend to exhibit the same statistical properties, no matter if correlated or uncorrelated ensembles have been used. In other words, as the number of internal freedom degrees becomes larger, variance reduction is no longer achieved. A detailed review of micro-macro methods for multiscale simulations of viscoelastic flows can be found in [9].

The hybrid BDDFS method (Brownian Dynamics and Distribution Function Storing) presented in this chapter, avoids the storage problem by using a smaller quantity of information compressed in a discretized configurational distribution function (D-CDF) [102]. All physical quantities of interest in the flow calculation are completely described by this function, which itself can be accurately obtained by using suitable grids in the configuration space with an economically small resolution. We use a representative set of dumbbells to evolve the D-CDF. They are created (consistently with the D-CDF at the previous time step) and overwritten at every time step. We do not

need to store them. The only memorised quantities will be the values of the D-CDF discretized on a grid, while on the other hand, the extra stress tensor will be evaluated as average over a large number of dumbbells (without memory costs) in order to achieve an accuracy comparable with a conventional BD routine.

To summarise: With CT you need large memory and large CPU time. With BCF, LPM and VRCT you need few memory and small CPU time, but the results could be not so accurate because of the 'poor' sample over initial configurations using few correlated stochastic representations. For BDDFS you need small memory but large CPU time (comparable with CT), however you do not have to do any assumption of similar flow histories to obtain variance reduction. In addition, the results of BDDFS are so accurate as the standard uncorrelated CT approach. Finally, for spectral methods you need small memory and small CPU time.

Concerning chain length, for CT, BCF, LPM, and VRCT the required resources increase 'normally' with chain length, for 'Brownian Dynamics and Distribution Function Storing' (BDDFS) the memory costs increase fast, and spectral methods become unfeasible already for short chains. Concerning numerical accuracy the use of a fully uncorrelated ensembles of dumbbells (CT or BDDFS) should be preferred. In fact, the hypothesis of similar flow histories (which is assumed in order to have noise reduction) is quite questionable in particular situations of interest as for instance in turbulence flows where the velocity field changes remarkably in nearby points. For flows near boundaries where – even for moderate Reynolds numbers – the velocity 'jumps' from a finite value rapidly to zero at the wall, the resolution of the BDDFS lattice – and therefore its memory costs – does not necessarily increase. It should however increase, if the distribution function becomes peaked around a preferred aligned state, i.e., at large Reynolds numbers where spectral methods (if applicable) offer advantages.

5.2 Microscopic kinetic model and standard CT approach

The main task of a microscopic description of the polymeric fluid is to motivate suitable expressions relating the macroscopic stress tensor, which appears in the Navier-Stokes equations, to the additional structural variables. Additional equations of change have then to couple the macroscopic flow field to the additional variables. In order to illustrate this approach in some detail, let us consider the general Navier-Stokes equation written in Lagrangian form and equipped with the usual extra stress tensor introducing elastic effects

$$\frac{d\mathbf{v}}{dt} = -\frac{1}{\rho}\nabla p + \frac{\eta_s}{\rho}\Delta\mathbf{v} + \frac{1}{\rho}\nabla \cdot \boldsymbol{\tau}^p, \quad (5.1)$$

where η_s is the solvent viscosity and $\boldsymbol{\tau}^p$ is the polymeric contribution to the total stress tensor. We assumed here that we are dealing with a perfect incompressible flow so that $\nabla \cdot \mathbf{v} = 0$ and all corresponding terms are removed in the momentum equation (5.1). Challenging is the evaluation of the components of $\boldsymbol{\tau}^p$ at (\mathbf{x}, t) . Microscopically,

a dilute polymer solution (polymers dissolved in Newtonian solvent) is typically modelled by non-interacting dumbbells consisting of two beads connected with a spring and subjected to a dissipative force with friction coefficient ζ plus a stochastic contribution. Each dumbbell is described in terms of its orientation and length, i.e., by a vector \mathbf{Q} connecting two beads. The evolution equation for the CDF $\psi(\mathbf{x}, \mathbf{Q}, t)$ for dumbbells in dilute solution follows from standard kinetic theory for this problem and reads [4]

$$\frac{d\psi}{dt} = -\frac{\partial}{\partial \mathbf{Q}} \cdot \left(\boldsymbol{\kappa} \cdot \mathbf{Q} - \frac{2}{\zeta} \mathbf{F}(\mathbf{Q}) \right) \psi - \frac{2k_B T}{\zeta} \frac{\partial^2}{\partial \mathbf{Q}^2} \psi, \quad (5.2)$$

where k_B is Boltzmann's constant, T is the kinetic temperature and $\psi(\mathbf{x}, \mathbf{Q}, t)d\mathbf{Q}$ represents the probability of having a dumbbell located in \mathbf{x} with a connector vector in the range $[\mathbf{Q} - d\mathbf{Q}, \mathbf{Q} + d\mathbf{Q}]$. Equation (5.2) describes convection and diffusion of the CDF $\psi(\mathbf{x}, \mathbf{Q}, t)$ subjected to the (transposed) macroscopic deformation rate tensor $\boldsymbol{\kappa}(\mathbf{x}, t) = (\nabla \mathbf{v}(\mathbf{x}, t))^T$ and $\mathbf{F}(\mathbf{Q})$ represents the spring force acting between bonded beads. At this point, we should be able to recover the extra stress tensor $\boldsymbol{\tau}^p$ directly from the knowledge of the CDF at the corresponding location. We can use Kramer's expression for the stress tensor

$$\boldsymbol{\tau}^p = -nk_B T \mathbf{1} + nH \langle \mathbf{F}(\mathbf{Q})\mathbf{Q} \rangle, \quad (5.3)$$

where n is the number density of dumbbells, and $\mathbf{1}$ the unit tensor. The average of a quantity $f(\mathbf{Q})$ is defined via $\langle f \rangle = \int \psi f(\mathbf{Q})d\mathbf{Q}$. The problem, Eq. (5.1), supplemented with Eqs. (5.2)-(5.3), is therefore well-defined. Once the initial conditions for the macroscopic velocity field $\mathbf{v}(\mathbf{x}, t_0)$ and for the microscopic CDF $\psi(\mathbf{x}, \mathbf{Q}, t_0)$ are known, the strategy is to integrate Eq. (5.1) using a suitable evolution scheme (i.e., Euler, Predictor-Corrector, etc.), then to evaluate the macroscopic gradient $\boldsymbol{\kappa}(\mathbf{x}, t)$ (from the new velocity field) and to insert it into Eq. (5.2). By integrating Eq. (5.2) we obtain a new CDF ψ , when introduced in Eq. (5.3), produces a new extra stress tensor field $\boldsymbol{\tau}^p(\mathbf{x}, t)$ for the momentum equation, thus closing the loop. Despite of its apparent simplicity, the described way to proceed poses many computational problems. In fact, Eq. (5.2) is a second-order partial differential equation with derivatives in both configurational and physical space. Consequently, it should be integrated on a high-order dimensional space. This approach is generally considered quite uneconomic and only few numerical works appeared in the literature based on this strategy [103, 104, 105]. Using spectral methods, however, is an alternative for low-dimensional problems such as the dumbbell dynamics considered in this work, see, e.g. [10, 106, 107, 4, 108, 109]. For more complex kinetic models (e.g. multibead chains with more than two beads) the integration of the Fokker-Planck equation on the respective higher-order configurational space via spectral methods loses its efficiency, and becomes conceptually cumbersome, while the structure of stochastic techniques remains unchanged, independent of chain length, as long as hydrodynamic interactions between beads are disregarded.

An approximate treatment of this problem, probably the one mostly adopted, and which we would therefore like to mention, is to motivate a closed equation for the extra stress tensor starting from the microscopic equations (5.2)-(5.3). Exact closures are derivable only in a few simple, technologically irrelevant, cases. An exact solution

is possible for the Hookean dumbbells model (where the spring force $\mathbf{F}(\mathbf{Q})$ is linear in \mathbf{Q}) giving the so called Oldroyd-B differential constitutive equation. Although this model works quite well for small shear rate flows, inaccurate results are returned as the shear rate increases. This failure is related to the Hookean dumbbells infinite extensibility which comes together with a constant, shear-independent, Newtonian viscosity. Experimentally, one observes a pronounced shear thinning (decreasing viscosity) for dilute polymeric solutions with increasing flow rate. A more sophisticated microscopic description is obtained by considering anharmonic spring forces which allow to ensure finite extensibility even in extremely strong flow situations. In the early 70's Warner proposed the so called FENE (Finite Extensibility Non-linear Elastic) force law

$$\mathbf{F}(\mathbf{Q}) = \frac{H\mathbf{Q}}{1 - Q^2/Q_{\max}^2}, \quad Q \leq Q_{\max}, \quad (5.4)$$

where $Q = |\mathbf{Q}|$. Equation (5.4) is a nonlinear spring force with a Q -dependent elastic coefficient which gets stiffer as the spring is extended providing a maximum elongation Q_{\max} . In the case of FENE force there is no exact closure relation for the stress tensor, but approximations such as the so-called Peterlin approximation (FENE-P) which involves a preaveraged denominator in Eq. (5.4) are frequently used [4]. The FENE-P constitutive equation for the orientation tensor $\mathbf{A} \equiv \langle \mathbf{Q}\mathbf{Q} \rangle$ reads

$$\frac{d\mathbf{A}}{dt} = \boldsymbol{\kappa} \cdot \mathbf{A} + \mathbf{A} \cdot \boldsymbol{\kappa}^T + \frac{4k_B T}{\zeta} \mathbf{1} - \frac{4H/\zeta}{1 - Tr(\mathbf{A})/Q_{\max}^2} \mathbf{A}, \quad (5.5)$$

and the macroscopic polymer stress $\boldsymbol{\tau}^p$ is obtained by the use of the following analogous Kramer's expression

$$\boldsymbol{\tau}^p = -nk_B T \mathbf{1} + \frac{nH}{1 - Tr(\mathbf{A})/Q_{\max}^2} \mathbf{A}. \quad (5.6)$$

The FENE-P model is amply used for numerical studies of viscoelastic fluids because of its small hardware requirements which make it amenable to computer simulations in comparison with purely microscopic models where the kinetic equation (5.2) must be solved. On the other hand the physical connection with the microscopic description contained in the FENE model is direct, except for the Peterlin approximation. It should be pointed out, that numerical comparisons between FENE and FENE-P models exhibit most qualitative disagreement when strong elastic effects take place [11, 110, 111] and in the presence of strong shear flows as in the case of turbulent boundary layers [98, 112]. The range of validity of such approximations is an open issue and also its quantitative effect on the exact solutions based on Eq. (5.2) equipped with Eq. (5.4). Consequently it should be highly desirable to perform direct simulations based on the exact FENE model.

The goal of CT is to evaluate a solution of the exact kinetic equation (5.2), but in a way which permits to avoid the computational bottleneck caused from its numerical discretisation on the high-order configurational space [11, 97]. The main idea is based on a stochastic evaluation of the CDF of the dumbbells ψ instead of its determination based on Eq. (5.2). Use is made of the fact, that the Fokker-Planck equation (5.2) has an

equivalent formulation in terms of a stochastic Markovian process (Langevin equation). To be more specific, if we consider a set of N_d dumbbells $\{\mathbf{Q}_1, \mathbf{Q}_2, \dots, \mathbf{Q}_{N_d}\}$ distributed over the domain, the resulting equivalent formulation of Eq. (5.2) reads

$$d\mathbf{Q}_\alpha(t) = \left(\boldsymbol{\kappa}(t) \cdot \mathbf{Q}_\alpha(t) - \frac{2}{\zeta} \mathbf{F}(\mathbf{Q}_\alpha(t)) \right) dt + \sqrt{\frac{4k_B T}{\zeta}} d\mathbf{W}_\alpha(t), \quad (5.7)$$

which represents the Itô stochastic differential equation for each individual dumbbell $\alpha = 1, \dots, N_d$. The quantities $d\mathbf{W}_\alpha$ denote N_d independent stochastic Wiener processes. The set of dumbbell elongation vectors evolve at every time step following Eq. (5.7). This procedure constitutes the BD method. The extra stress tensor is calculated by applying Kramer's expression (5.3) to the new set of dumbbell variables, i.e.,

$$\boldsymbol{\tau}^p = -nk_B T \mathbf{1} + nN_d^{-1} \sum_{\alpha=1}^{N_d} \mathbf{F}(\mathbf{Q}_\alpha) \mathbf{Q}_\alpha. \quad (5.8)$$

Finally, as above, the polymeric stress enters into the macroscopic flow calculation via Eq. (5.1). This approach has been successfully implemented for non-trivial flow problems such as the start-up of flow between two parallel plates and for an elongational steady flow in an abrupt 4:1 axisymmetric contraction [11, 85, 113]. These simulations have been performed by using a rather small number of dumbbells or number of spatial cells. However, the main limitation of the approach is related to the computer hardware performance. CPU time and, mainly, memory requirements become significantly high whenever a large ensemble of polymer molecules is needed. In terms of computer memory, for example, if we discretize the equation (5.2) on a domain divided in N_c computational elements, we need at least a number of floating points proportional to $N_d N_c$. This corresponds to simulating N_c ensembles of N_d uncorrelated dumbbells, one for each cell on the domain. Basic statistics tells that the level of fluctuations of a quantity evaluated as an average over n independent values is of order $O(n^{-1/2})$. Therefore, in order to determine the value of the extra stress tensor on a specific grid position \mathbf{x} with a reasonable level of statistical noise, we should use a very large number of independent trajectories: for example, an accuracy of the 0.1% would require at least 10^6 dumbbells. Next we should present the memory-saving BDDFS approach.

5.3 The hybrid BDDFS method

For the sake of simplicity we will describe the BDDFS methodology only in the configurational space omitting the label corresponding to the additional discretisation of the macroscopic conservation equations. The generalisation for inhomogeneous flows is straightforward. The basic idea of the hybrid BDDFS method lies on a discrete representation of the configurational distribution function (CDF), such as for spectral methods, but instead of solving rather complicated equations for the coefficients we solve simple Langevin equations for particles re-sampled from the D-CDF. The result is an improvement of the hardware requirement of a standard BD routine. Also, we do not rely on the formulation and solvability of the nonlinear differential equations for coefficients of

the CDF. Thus, the evolution step is performed by $\hat{\text{Ito}}$ stochastic differential equation for a set of N_d dumbbells, i.e. its realizations, and we avoid storing all the microscopic dumbbell configurations.

It is obvious from Eq. (5.3) that the only information needed to extract the macroscopic polymeric stress is that one contained in a coarse-grained description of the CDF and not the exact microscopic configuration of every single dumbbell. The CDF, however, should often be accurately discretized in every element of the spatial domain by using a number of grid point N_f in the \mathbf{Q} -space much smaller than N_d . If we confirm that quantitative predictions remain unchanged within a given accuracy while introducing a D-CDF with optimum (small N_f) resolution, the computational advantage is as large as N_d/N_f in terms of memory costs.

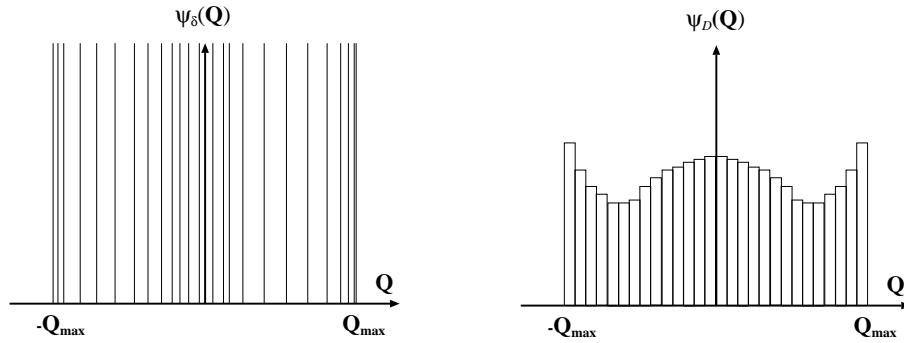


Figure 5.1: Schematic picture of the two representations of the CDF. On the left side, the δ -Dirac representation ψ usually adopted in BD simulations. On the right side, the coarse-grained description represented by the D-CDF ψ_D evaluated by using an uniform square grid in the \mathbf{Q} -space (bounded for FENE dumbbells).

The two following alternative representations of a CDF are schematically sketched in Fig. 5.1: 1) The exact Dirac representation of the CDF $\psi(\mathbf{Q})$ used in standard BD:

$$\psi(\mathbf{Q}) \propto \sum_{\alpha=1}^{N_d} \delta(\mathbf{Q} - \mathbf{Q}_\alpha) \quad (5.9)$$

where \mathbf{Q}_α are the N_d microscopic dumbbell vectors, δ denotes a Dirac distribution, and 2) The D-CDF $\psi_D(\mathbf{Q})$ which represents the coarse-grained description (histogram) defined on a grid in the configurational space discretized with N_f cells. For the latter we subdivided the configurational domain (bounded in the case of FENE dumbbells) on an uniform square grid with cells of size ΔQ in each dimension, i.e.,

$$\psi_D(\mathbf{Q}) \propto \sum_{k=1}^{N_f} \psi_k \delta_{\Delta Q}(\mathbf{Q} - \mathbf{Q}^{(k)}) \quad (5.10)$$

where $\mathbf{Q}^{(k)}$ denotes the centre position of cell k , the weights ψ_k are defined by

$$\psi_k = \int_{Q_x^{(k)} - \frac{\Delta Q}{2}}^{Q_x^{(k)} + \frac{\Delta Q}{2}} \int_{Q_y^{(k)} - \frac{\Delta Q}{2}}^{Q_y^{(k)} + \frac{\Delta Q}{2}} \int_{Q_z^{(k)} - \frac{\Delta Q}{2}}^{Q_z^{(k)} + \frac{\Delta Q}{2}} \psi(\mathbf{Q}) dQ_x dQ_y dQ_z \quad (5.11)$$

and the distribution $\delta_{\Delta Q}(\mathbf{Q})$ is defined as

$$\delta_{\Delta Q}(\mathbf{Q} - \mathbf{Q}^{(k)}) = \begin{cases} 1 & \text{if } \forall \nu \in \{x, y, z\} |Q_\nu - Q_\nu^{(k)}| < \frac{\Delta Q}{2}, \\ 0 & \text{otherwise.} \end{cases} \quad (5.12)$$

In the above, Q_ν denote Cartesian coordinates of \mathbf{Q} for the 3D case. Once the square grid in \mathbf{Q} -space has been defined, cf. Fig. 5.2, the coefficients ψ_k in Eq. (5.10) represent the number of dumbbells whose connectors lie within cell k . A coarsening step from ψ to ψ_D is thus performed by a simple histogram operation. An inverse operation or ‘reconstruction’ requires an assumption about the distribution function ψ which is not available at level ψ_D . In this manuscript we will test the simplest assumption where cell k is reconstructed by a number of ψ_k dumbbells uniformly distributed over the cell. Alternatively, one may take into account gradients of the D-CDF. The ‘local’ reconstruction is performed by a double loop over all cells $k = 1..N_f$ and over the (extracted) number of dumbbells ψ_k . A particular ‘reconstructed’ connector vector \mathbf{Q}_α is therefore generated at every cycle via

$$\mathbf{Q}_\alpha = \sum_k \mathbf{Q}^{(k)} \delta_{\Delta Q}(\mathbf{Q}_\alpha - \mathbf{Q}^{(k)}) + \frac{\Delta Q}{2} \mathbf{r}_\alpha \quad (5.13)$$

where \mathbf{r}_α is a random vector homogeneously distributed over the unit square. Obviously, the inverse operation does not take into account all microscopic information, that is, dynamics on length scales smaller than ΔQ won’t be resolved. We will return to this aspect in the next section.

Having introduced the D-CDF we can turn to the description of its dynamics. To this end we revisit the standard BD time loop. Without loss of generality let us consider a simple Euler scheme for the evolution from time $t_n \equiv n\Delta t$ with time increment Δt to t_{n+1} , i.e., from time step n to step $n + 1$:

$$\mathbf{Q}_\alpha^{n+1} = \mathbf{Q}_\alpha^n + \left(\boldsymbol{\kappa}^n \cdot \mathbf{Q}_\alpha^n - \frac{1}{2\lambda_H} \mathbf{F}(\mathbf{Q}_\alpha^n) \right) \Delta t + \sqrt{\frac{1}{\lambda_H}} \Delta \mathbf{W}_\alpha^n, \quad (5.14)$$

for all dumbbells $\alpha = 1..N_d$. This represents a time-discretized dimensionless version of Eq. (5.7), where we introduced the relaxation time $\lambda_H = \zeta/4H$ and connector vectors \mathbf{Q} are made dimensionless (keeping the same symbol) by the reference length $\sqrt{k_B T/H}$; $\boldsymbol{\kappa}^n$ denotes $\boldsymbol{\kappa}$ at time n . The increments $\Delta \mathbf{W}_\alpha^n$ of the Wiener processes are made of Gaussian distributed random components with mean 0 and variance 1. When considering inhomogeneous flow problems, the processes can be (a priori freely) chosen as correlated or uncorrelated in space, that is, we can consider the same sequence of random kicks for every cell discretizing the Navier-Stokes equation in physical space, or independent sequences. The standard BD needs to store all the dumbbell coordinates \mathbf{Q}_α^n for $\alpha = 1..N_d$ at least for one time step n in order to obtain new configurations at time $n + 1$.

This ‘problem’ is avoided by the BDDFS approach during the following three-step procedure, which has to be performed N_d times: (a) reconstruction of dumbbell configuration α consistent with the D-CDF at time n , (b) evolution of reconstructed dumbbell α from n to $n+1$, and, (c) accumulating the D-CDF for time $n+1$. If interacting dumbbells

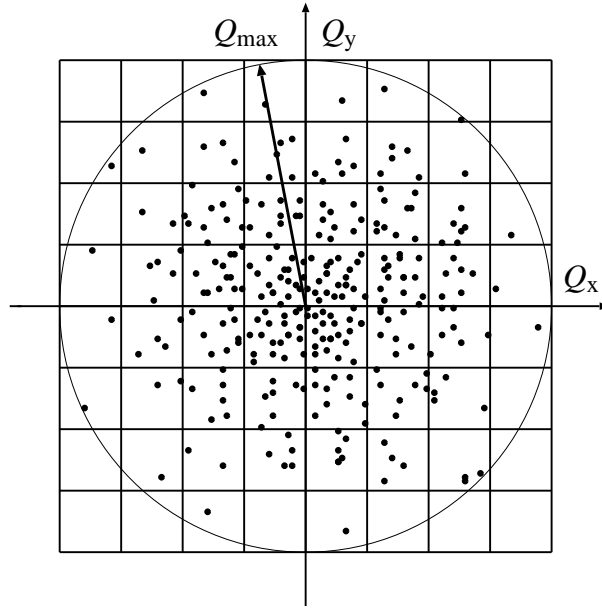


Figure 5.2: Discretisation of the two-dimensional configurational space for the FENE dumbbells model. The black points represent the configurational variables (stretching) of every FENE dumbbell (N_d) flowing through the domain discretized in the BDDFS method by using a grid with N_f cells. The circle represents the boundary of the configurational space corresponding to the finite maximum extensibility Q_{\max} .

with finite cutoff interaction distance were considered, instead of reconstructing a single dumbbell, a finite set of dumbbells has to be constructed using neighbour lists (requiring an irrelevant amount of memory). To be more specific, for the case of non-interacting dumbbells, (a) requires the suitable generation of a single particular dumbbell vector \mathbf{Q} consistent with ψ_k^n (known at time step n) via Eq. (5.13) where \mathbf{Q}_α is replaced by \mathbf{Q} . For (b) we evaluate the intermediate quantity \mathbf{Q}' following the usual BD equation (5.14) where \mathbf{Q}_α^n and \mathbf{Q}_α^{n+1} are replaced by \mathbf{Q} and \mathbf{Q}' , respectively. For (c), according to Eq. (5.11), the evolved quantity \mathbf{Q}' contributes to the D-CDF $\psi_{k'}^{n+1}$ of cell k' , where k' may be different from k .

See Fig. 5.3 for a schematic drawing of the BDDFS loop which returns the time evolution of the weights ψ_k , but does not store the dynamics of individual dumbbells \mathbf{Q}_α . We just need to provide an initial ψ_k^n . Two single microscopic dumbbell connector vectors \mathbf{Q} , \mathbf{Q}' are needed to evolve the D-CDF such that the memory requirement is produced by the resolution of the D-CDF alone. One should notice that the number of numerical operations for BDDFS is about the same as for a standard BD. The histogram update does not produce costs and the equally distributed random numbers needed in Eq. (5.13) together with the Gaussian random numbers of Eq. (5.14) can be combined within a single set of Gaussian distributed random numbers with variance $\Delta Q/12 + \sqrt{1/\lambda_H}$.

We should motivate the choice of cubic cells for the D-CDF. Fast generation of reconstructed values compatible with an arbitrary ψ based on the transformation method

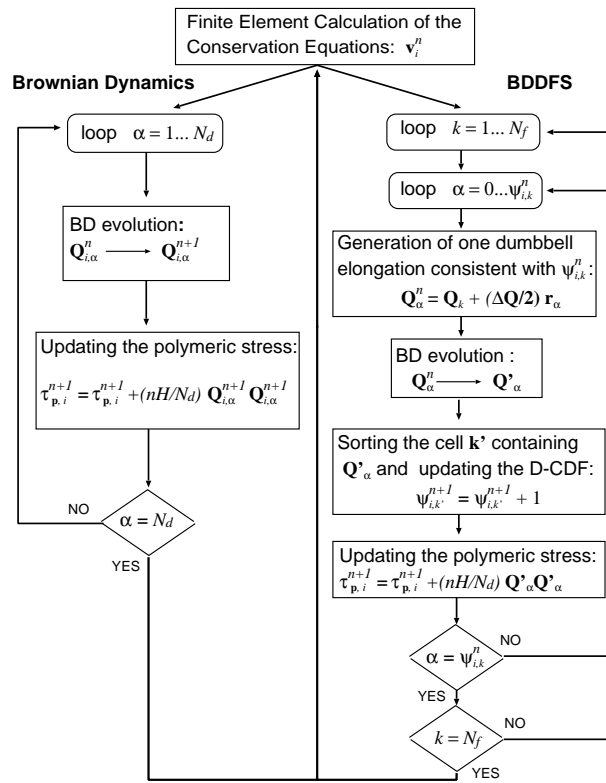


Figure 5.3: Scheme of the numerical loop in the two cases: BD vs. BDDFS. The loop corresponds here to one particular time step t_n . Here we introduced also a label i indicating the discretisation of the conservation equations in the physical space. The label serves as a reminder for the time-loop adopted in CT -type calculations. The double loop in BDDFS is equivalent to the single loop over all the N_d dumbbell elongations, but here we do not store N_d variables $\mathbf{Q}_{i,\alpha}^n$, but one single dumbbell variable \mathbf{Q} is needed, and the memorised information is stored in N_f grid weights $\psi_{i,k}^n$.

are possible only when the inverse of the probability function is easily computable numerically or analytically; this scheme needs the generation of only one random number in order to produce the suitably distributed value. On the other hand, for D-CDF, for which an inverse is not accessible, a time consuming rejection method must be used. Within the described BDDFS approach an inverse has not to be constructed due to the fact that we are using a histogram representing the D-CDF. This particularly simple discretisation is therefore crucial for keeping BDDFS comparably fast with conventional BD. In this respect BDDFS has advantages upon other possible, sophisticated, representations of the CDF based on basis function sets as for example that one developed by Jendreck, de Pablo and Graham [114]. In their case a set of linear equation in N_d unknowns must be solved at every time step in order to recover a consistent microscopic configuration.

5.4 Numerical results

In this section we will present numerical results for the case of a homogeneous shear flow and will discuss the accuracy, limitations and advantages of BDDFS compared with standard BD (with N_d uncorrelated dumbbells). This simple test case should provide a significant indication on how BDDFS behaves in terms of efficiency when considering inhomogeneous flows. For this flow geometry we have $\mathbf{v}(\mathbf{x}) = \dot{\gamma} \mathbf{x} \cdot \mathbf{e}_y \mathbf{e}_x$, i.e., the transposed deformation rate tensor reads $\boldsymbol{\kappa} = \dot{\gamma} \mathbf{e}_x \mathbf{e}_y$, i.e., it is a ‘constant’ parameterised by the shear rate $\dot{\gamma}$, and the \mathbf{e} ’s denote cartesian base vectors. We implemented two algorithms for FENE dumbbells corresponding to the BD and BDDFS method, respectively. The evolution equation is solved by a simple first-order Euler algorithm. This is not the best choice for all purposes. Second-order predictor-corrector, suitable Runge-Kutta methods or semi-implicit algorithms [97], may be preferably used to perform the runs, but the Euler version is sufficient to compare the accuracy, CPU time and memory requirements of the two methods. In order to simulate FENE dumbbells one commonly implements a routine preventing a dumbbell to have an extension bigger than the maximum allowed stretch Q_{\max} , cf. Eq. (5.4). We choose a simple rejection method where only moves for which $1 - Q/Q_{\max} > (0.02 \lambda_H^{-1} \Delta t)^{1/2}$ are allowed. The BD routine has been implemented and applied to N_d (going from 1600 to 10^6) uncorrelated dumbbells in a single cell $N_c = 1$ at given shear rate. For the BDDFS algorithm the D-CDF is stored on a limited 2D square box domain in the \mathbf{Q} -space with edge equal to $2Q_{\max}$ consistent with the maximum extension of a FENE dumbbell, cf. Fig. 5.2. The integration time step has been chosen as $\Delta t = 0.01 \lambda_H$. For simulations with a $n_c \times n_c = 200 \times 200$ grid, for which $N_f = n_c^2 = 40000$, the effect of shear rate on shear viscosity η , first viscometric function Ψ_1 and squared dumbbell stretch Q^2 is reported in Figs. 5.4, 5.5.

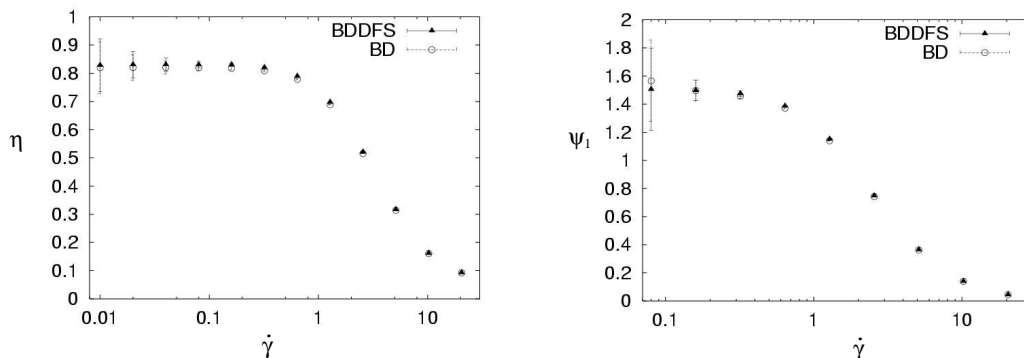


Figure 5.4: Effect of shear rate on shear viscosity η and first viscometric function Ψ_1 . Comparisons between (○) BD vs. (△) and BDDFS are shown. The total number of simulated FENE dumbbells is $N_d = 10^6$ while in the BDDFS case, we still use N_d dumbbells but the coarse-grained D-CDF is recorded just in $N_f = 40000$ grid points. Averages were sampled from 900 steady state values (in equidistant time units) between $t = 1.0 \lambda_H$ and $t = 10 \lambda_H$.

The plotted values for the material functions have been obtained by extracting their

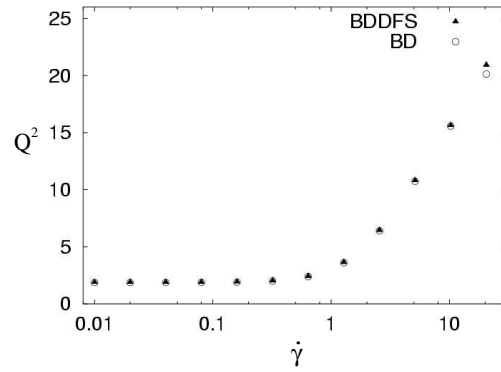


Figure 5.5: Dependence of the global stretching Q^2 on shear rate. (\circ) BD vs. (\triangle) BDDFS.

averages once the system achieved a steady state. Results are also compared with those obtained via BD in Figs. 5.4, 5.5.

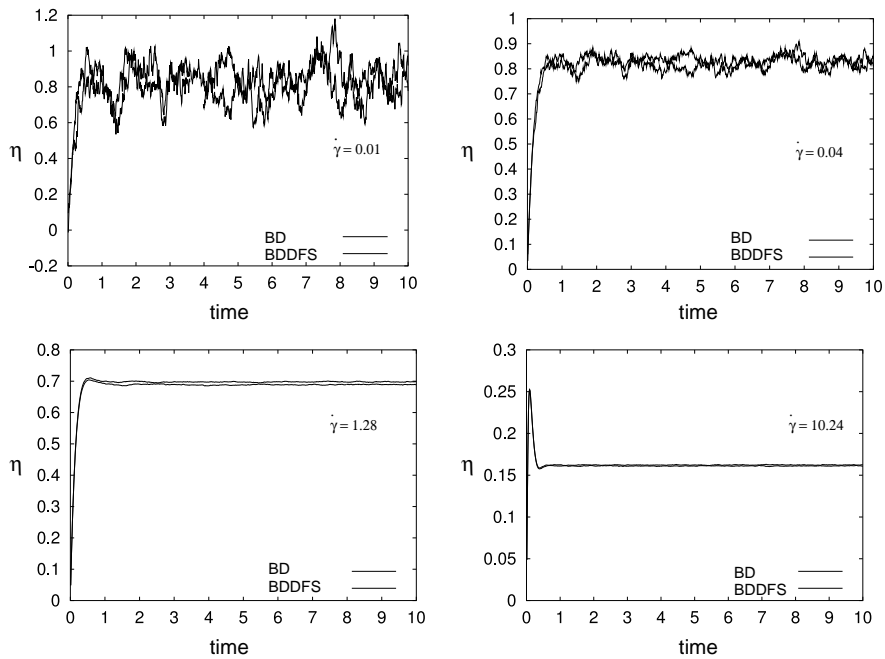


Figure 5.6: Evolution of the polymer viscosity η for different shear rates $\dot{\gamma} = 0.01, 0.04, 1.28, 10.24$. The BDDFS method was implemented by using a grid 200×200 .

The agreement between the two methods is not only very good concerning the averages but also with respect to the amount of fluctuations and to the transient properties. Results extracted from the two runs therefore exhibit the same accuracy. With decreasing shear rate the error bars increase while we are keeping the maximum physical time ($10\lambda_H$) for all simulation runs.

Figure 5.6 provides transient data for several shear rates. In Fig. 5.7 we show

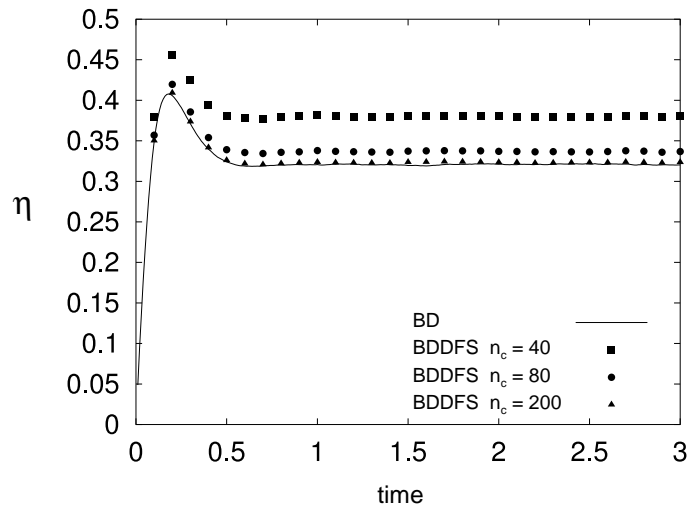


Figure 5.7: Comparisons in the evolution of η vs time at rate $\dot{\gamma} = 5$ between BDDFS (with different grids) and BD. The grids used were: $n_c = 40, 80, 200$. As it can be observed, the error remains limited and constant also in the unsteady steady state. The agreement between the two methods in the evaluation of the viscometric functions, as shown in Figs. 5.6, 5.4, and Eq. (5.5), is not only a steady state feature but it is still valid in the transient case.

results for BDDFS runs with three different grid resolutions and also compare them with the ‘exact’ solution obtained with $N_d = 10^6$ dumbbells. Let us consider now some brief remarks on the error present in the results of Fig. 5.7. This indeed represents a strong limitation of the BDDFS method when going to simulate situations in higher-order configurational space, (i.e. polymer-chains model) where a much larger number of grid points must be used to discretise the CDF. As already discussed in section 5.3, this preliminary version of the BDDFS method extracts the information from the stochastic dynamics which is stored in a vector of integers representing only the numbers of dumbbells ψ_k contained in every cell of the grid. Of course, in this picture, we forget all the information coming from the dynamics ‘within’ the size of one cell. This could be the most important source of errors appearing in Fig. 5.7. In fact, at every time step the dumbbell configuration is re-created in every cell without any reference to a possible inhomogeneous internal distribution. On the other hand, during a time step the dumbbells will move through the domain, sometimes crossing the cell boundaries but sometimes remaining in the same cell ψ_k . The result of this motion changes only the internal distribution of the molecules (within ψ_k) which is not taken into account from the present BDDFS routine (i.e the dumbbell configuration is updated by considering a homogeneous distribution over the cell, Eq. 5.13). This can be seen as a limitation of the BDDFS routine into capture displacements of the centre of mass of the dumbbells within the cells, and resulting in an artificial numerical viscosity (due to the grid) added to the theoretical one. Modifications of the present BDDFS method, where also the internal distribution is taken into account, are currently under investigation. First preliminary results seem suggest that a much smaller number of grid points could be used for the same accuracy.

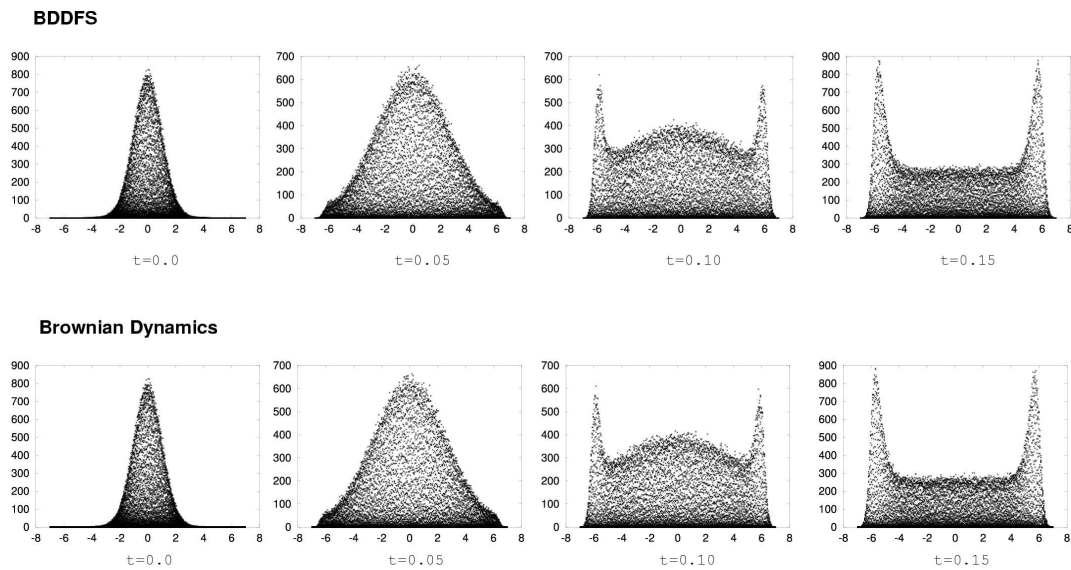


Figure 5.8: Comparison in the time evolution of the x -projection of D-CDF between the BDDFS and the BD routines for a shear rate $\dot{\gamma} = 10.24$. The D-CDF has been evaluated in the BD by using an equivalent partition of the domain as in the BDDFS method and counting the number of dumbbell contained in every cell. It should be pointed out that this information, in the BD, represents only an output, while in the BDDFS it plays a crucial role in the dynamics. The two evolutions exhibit practically no differences.

Figure 5.8 shows a comparison between the D-CDF obtained via BDDFS (top) and the one evaluated by BD (bottom) at different time steps. Since overall quantitative agreement is obvious for sufficiently large grids next we will compare the two methods concerning accuracy and hardware requirements. For this purpose the value of the shear rate is fixed at a comparable large value $\dot{\gamma} = 5$ where the configurational distribution function is not uniform, and BDDFS with a homogeneous grid is tested seriously. We performed BDDFS simulations with grids varying from 40×40 to 1000×1000 . The latter case is irrelevant from a practical point of view because there is actually no memory advantage but it is still useful as a limiting case.

In Tab. 5.1 we summarise hardware requirements (CPU time and memory), steady state values and variances of the material functions for the two methods. While CPU time requirements are comparable at fixed N_d , the memory advantage of the BDDFS is evident from Tab. 5.1. As expected, with decreasing grid resolution the errors increase. For instance, in the case of a 200×200 grid with $N_d = 10^6$, the results are comparable with those extracted from the corresponding BD run (considered as reference values) within 1% and with the same statistical error, while the memory saving ratio is of order 50. Reducing the resolution of the grid to 40×40 the error for shear viscosity increases systematically to around 18%. The small BDDFS tendency to overestimate viscosity values we associate with an effective artificial viscosity due to the grid. This effect prevents us to extract accurate averages for low-resolution grids, and it vanishes for sufficiently large grids. While Table 5.1 shows results at a large shear rate, where

method	$\sqrt{N_d}$	$\sqrt{N_f}$	CPU [s]	mem [MB]	η	Ψ_1	Q^2
BD	1000	-	2.36(1)	15.616(1)	0.3202(4)	0.3734(3)	10.582(9)
BDDFS	1000	40	2.72(1)	0.016(1)	0.3730(5)	0.4065(4)	11.707(9)
BDDFS	1000	80	2.73(1)	0.052(1)	0.3341(5)	0.3830(3)	10.896(9)
BDDFS	1000	200	2.73(1)	0.316(1)	0.3213(4)	0.3747(3)	10.622(9)
BDDFS	1000	1000	3.04(1)	8.316(1)	0.3207(4)	0.3737(3)	10.588(9)
BD	200	-	0.131(1)	0.616(1)	0.324(2)	0.374(2)	10.61(5)
BDDFS	200	40	0.152(1)	0.016(1)	0.372(3)	0.407(2)	11.71(5)
BDDFS	200	80	0.154(1)	0.052(1)	0.335(3)	0.386(2)	10.97(5)
BDDFS	200	200	0.160(1)	0.316(1)	0.322(2)	0.377(2)	10.67(5)
BD	80	-	0.031(1)	0.092(1)	0.328(6)	0.375(4)	10.7(1)
BDDFS	80	40	0.040(1)	0.016(1)	0.366(7)	0.401(5)	11.6(1)
BDDFS	80	80	0.042(1)	0.052(1)	0.331(6)	0.382(4)	10.9(1)
BD	40	-	0.008(1)	0.016(1)	0.33(1)	0.383(8)	10.8(2)
BDDFS	40	40	0.010(1)	0.016(1)	0.35(1)	0.395(9)	11.3(2)

Table 5.1: Quantitative comparisons between the BD, with N_d dumbbells, and the BDDFS with many different grids of size N_f . CPU time (for one time step), memory requirements, averages and standard deviations for the steady-state material functions are listed. All the results considered here correspond to simulations performed with a shear rate $\dot{\gamma} = 5.0$. Errors listed within brackets are given in terms of the uncertainty in the last digit.

method	$\sqrt{N_d}$	$\sqrt{N_f}$	CPU [s]	mem [MB]	η
BD	1000	-	2.36(1)	15.616(1)	0.77(9)
BD	100	-	0.05(1)	0.148(1)	0.4(9)
BDDFS	1000	100	2.73(1)	0.080(1)	0.73(9)

Table 5.2: Quantitative comparisons between the BD and the BDDFS for a shear rate $\dot{\gamma} = 0.01$. Hardware requirements, averaged polymeric viscosity and standard deviations are listed for three different runs. See also Fig. 5.9.

the advantages of BDDFS are obvious, but not as large as for lower rates.

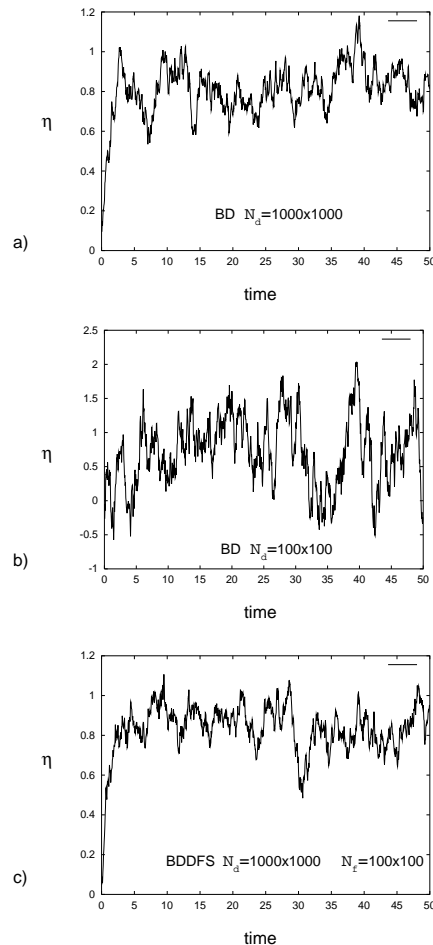


Figure 5.9: Evolution of the polymeric viscosity compared between the BD and the BDDFS for a shear rate $\dot{\gamma} = 0.01$. (a) BD simulation performed with $N_d = 10^6$ dumbbells. (b) BD simulation with $N_d = 10^4$ dumbbells: with such a small stochastic sample the random fluctuations increase and the signal is almost indistinguishable. (c) BDDFS run with $N_d = 10^6$ but with only $N_f = 10^4$ grid points. The accuracy is now comparable to the case (a) but with a memory lowering factor of order 200 and comparable CPU time (see Tab. 5.2).

If this is valid for high shear rates, it Table 5.2 collects additional results at low shear rate, $\dot{\gamma} = 0.01$. This table reports values for three different runs corresponding to BD with $N_d = 10^6, 10^4$ and BDDFS with $N_d = 10^6$ and $N_f = 10^4$. We see, that from the BD simulations with $N_d = 10^6$ an average can be evaluated for the polymeric viscosity with an accuracy of 11%. At the same (physical) time, the much faster BD run with $N_d = 10^4$ does not yield a significant nonzero measure because of the strong fluctuations present in such a small stochastic sample. BDDFS averages, comparably accurate with the former case, are obtained with a much smaller quantity of memory involved; memory saving is up to 95.5%. Further details are provided by Fig. 5.9, where the time evolutions of the polymeric viscosities are plotted for the three situations reported in Tab. 5.2.

In Figure 5.10 we plot the steady state values for the viscometric functions obtained with different grid resolutions. The plateau corresponding to the 'exact' BD solution is visible, indicating the good convergence of the numerical scheme.

5.5 Final remarks

In this chapter we have collected some evidence that BDDFS may be useful for studying rigorously the flow of complex fluids where memory requirement becomes a relevant issue, and where approximate solutions to the underlying Fokker-Planck equation do not provide an alternative. The BDDFS memory requirement can be further reduced by making use of symmetries of the CDF, by using pointers, or adaptive grids, rather than a static and partially empty grid. This is of particular relevance for situations far from equilibrium, i.e., at strong flows. Needless to say, memory costs can be reduced also within conventional BD by considering a smaller numbers N_d of molecules, upon increasing errors in an antagonistic fashion.

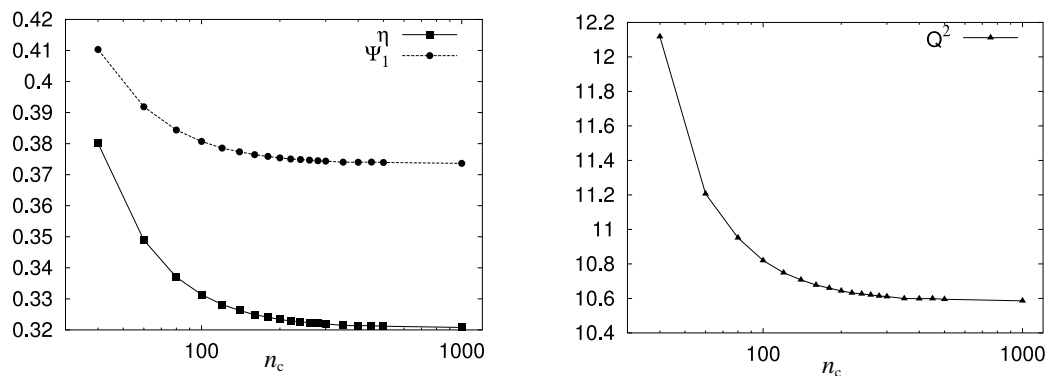


Figure 5.10: Grid refinement plots for the averaged steady-state material functions. 19 runs have been performed with different grid resolution going from $n_c \times n_c = 40 \times 40$ to $n_c \times n_c = 1000 \times 1000$. For a poor resolution ($n_c = 40$) the error in the estimate of the viscosity, first normal stress coefficient (left) and global stretching (right) are quite large. A resolution of $n_c \times n_c = 200 \times 200$ (small compared with $N_d = 10^6$) gives accurate results. See also Tab. 5.1.

It was the goal of the current research to test if the concept of D-CDF has advantages over the conventional approach. This has been confirmed for the case of a homogeneous, laminar, flow, specially in the limit of small shear rates (or Deborah number) where the classical stochastic techniques must use a very large number of realizations for an accurate evaluation of the stress.

Its simplicity concerning implementation efforts may be another appealing factor. If hardware limits the performance of conventional CT runs with a required large number of particles, BDDFS may provide the cheapest way out of this problem.

As a final remark, we should point out that the implementation of the CT methodology (via BDDFS or still BD) in a Smoothed Particle Dynamics code is an other

interesting computational issue. Indeed, as we have already mentioned in the first section, the 'state-of-the-art' micro-macro methods suffer of some difficulties related to the fact that they do not describe the flow in a fully Lagrangian fashion. This is for example the case of the traditional CT, where molecules are dispersed through the flow domain: the consequent algorithmic complexity due to their search and track can be result in serious computational drawbacks. In addition, it is not generally ensured that a sufficient number of molecules (for an accurate estimate of the stress tensor via (5.8)) will be present in every finite elements at every time step. This makes very difficult, if not impossible, an accurate control of the statistical error in the stress evaluation. This drawbacks are partially solved by the BCF and LPM methods, which, by considering respectively a correlated configuration field and a set of Lagrangian particles, can avoid the problems mentioned above. Nevertheless, these approaches are not exempt from difficulties: BCF can not be applied to an uncorrelated field, therefore problems characterised by physical fluctuations (i.e. turbulence) can not be described, while LPM, as recognized by Keunings in [13], can suffer of unphysical (over-smoothed) transfer of momentum between the Lagrangian evaluation of the stress and the Eulerian solution of the hydrodynamic fields. From this point of view, the Smoothed Particle Dynamics method, being fully Lagrangian, could in principle bypass all these problems, indeed 1) dumbbells tracking is not necessary as long as we consider element ('smooth particle') moving with the flow (only dumbbells diffusion should consider as we discussed in Chapter 4); 2) we do not have any problem related to unphysical coupling between grids. To our knowledge, if implemented, this would be the first every fully Lagrangian CT method in the literature. Needless to say, it could be very useful for a wide range of problems, i.e. free surface viscoelastic flows. We reserve to do this work in the next future.

Chapter 6

Conclusions

In this work, a general study on the applicability of the Lagrangian Smoothed Particle Hydrodynamics method for the solution of viscoelastic flow problems was carried out. The pursued research directions were developed along three different paths which we can denote as follows: macroscopic, mesoscopic and multiscale approach for viscoelastic fluids. In the first part of this thesis, a generalisation of SPH, i.e. Smoothed Particle Dynamics method, was presented, which is able to study complex viscoelastic phenomena by previous incorporation of a macroscopic constitutive equation for the stress tensor based on the corotational Maxwell model. The accuracy of the method was proven first in simple Newtonian cases and then tested in a variety of viscoelastic situations, including velocity profile relaxations in channel geometries, steady bulk shear flows, unsteady shear flows of a viscoelastic matrix in a periodic array of non-rotating rigid inclusions. The results obtained showed that the methodology is able to reproduce accurately, also quantitatively basis, many theoretical solutions recoverable in simple cases. In addition the strength of the scheme lies on its flexibility, which make it suitable to study more complex physical situations. The Lagrangian nature of the Smoothed Particle Dynamics method takes into account in the most natural way the hyperbolic character of the rheological constitutive equation, bypassing the need to consider special stability treatment, as “upwind” schemes, and allowing to simulate general unsteady flow problems. In addition, the absence of an underlying grid and the adaptivity of the particle system, avoids the problem of using complicate mesh, rezoning procedures or other grid-dependent drawbacks. Such peculiarity suggests that the method should represent an ideal alternative for problems dealing with irregular/complicate geometries (where an Eulerian scheme should use time-consuming preprocessing mesh-generation procedures) or even for free-surface flow problems, which we did not discuss in the present work, but which represent a natural field of application for future research. However, some problems still persist that are connected with an accurate treatment of boundary conditions which, although very easy to implement, do not achieve, in the opinion of the author, the performance obtained in well-established Eulerian techniques, where an accumulated numerical experience is available.

As often pointed out in the course of this work, the method for macroscopic flow problems becomes inapplicable to physical situations in which the length scales char-

acterizing the problem are quite 'small'. The word 'small' in this context is related to the presence of fluctuations in the thermodynamic subsystem considered. Indeed, it is well-known that as far as we are studying problems involving colloidal suspensions, microphase separation, polymer mixtures or any other kind of system where a crucial role is played by thermal diffusion, it is essential to use a description consistent with a fluctuating hydrodynamic theory. Fluctuations in the fluid variables must therefore be introduced in a way which respects the fundamental laws of physics, that is, First and Second Laws of Thermodynamics. The main result of the second part of this thesis was the construction of a thermodynamically consistent model for viscoelastic fluids in the sense given above. This was done using the GENERIC formalism which permits to build, in an easy and elegant way, physical models consistent with the previous laws. The elastic dynamics were introduced in the hydrodynamic formalism by considering a further variable associated to every particle and representing its elongational state. Very simple physical argumentations brought to the definition of an evolution rule which follows an Itô stochastic differential equation. A particularly interesting feature of the resulting set of equations is that the thermal fluctuations depend on the size of the fluid particles. This means that for large enough fluid particles, the thermal fluctuations in the energy and momentum equations can be neglected in accordance with the extensive nature of such variables. Contrary to the previous cases, the thermal fluctuations cannot be neglected at all in the stochastic equations for the dumbbell elongations and indeed they do not depend on the size of the particles. The reason for this is related to the fact that the dumbbell elongations are purely mesoscopic variables (we cannot extend their definitions to a macroscopic level) and for them the stochastic term is an essential part of the dynamics. The main conclusion is therefore that this model, as it has been developed, should have an applicability only for mesoscopic problems and not for a local description of a macroscopic flow. Nevertheless, one could argue that a connection to the micro-macro approaches is still possible by considering these elongational variables as one possible realization of the configurational field (in the sense given in BCF) even if here, as it has been stressed at the end of Chapt. 4, the advantages of variance reduction present in BCF, are less evident. The generalisation of this methodology for the study of macroscopic field, following the CONNFFESSIT philosophy, should resort to the CPU-time consuming and memory requiring procedure of averaging over a large set of stochastic realizations of the same hydrodynamic flow.

In the context of micro-macro simulations and after the considerations presented above, we attempted in Chapt. 5, an investigation on possible efficient algorithms for multiscale CONNFFESSIT-type simulations of polymer solutions. From the model previously developed, it is clear that, whenever interested in applying it to macroscopic flows, the problem of variance reduction for the stochastic estimate of the stress tensor should be addressed. As discussed in detail in Chapt. 5, there exists a huge variety of flow situations in which the standard variance reduction algorithms can not be applied. In such problems, a brute averaging routine involving very large ensembles of stochastic realizations is necessary so far. In the last part of this work, we presented a new hybrid method, i.e. Brownian Dynamics and Distribution Function Storing (BDDFS), which offers numerical advantages over traditional stochastic integrators like Brownian

Dynamics (BD). The method is based on a dual representation of the configurational distribution function: a Dirac-delta representation (commonly used in BD), and a discretized configurational distribution function (D-CDF) defined on square coarse-grained grid in the configurational space. The dynamics are split in two steps: the evolution based on a typical BD step and a further part consisting in the storage and recovery of a smaller set of relevant variables, i.e. the values of the D-CDF on the grid. As far as the number of grid points used is smaller than the number of dumbbells, for the same level of accuracy, the BDDFS method offers memory advantage over classical BD routines. This was tested in a homogeneous shear flow for different values of the shear rate. Although the memory advantage resulted to be quite modest in the range of high shear rates (where a small stochastic ensemble already gives accurate estimates for the stress tensor), a large memory reduction was obtained in the limit of small shear rates, where the difficulties of the stochastic techniques are well-known. For the same accuracy and comparable CPU-time, the BDDFS method offers a lowering memory factor of order 200 over a standard BD routine. This peculiarity of the BDDFS method could turn out to be very useful in simulations of viscoelastic flows where a large number of freedom degrees must be take into account to discretize finely the physical domain or to produce accurate local ensemble averages (i.e viscoelastic turbulent flows). Although the method appears to be very promising for simple dumbbell models, it seems to become cumbersome for higher dimensional spaces describing for example polymer-chain models. In such situations, the algorithmic complexity of the BDDFS method, being based on the fully discretisation of the configurational space, should increase much faster than for standard stochastic BD routines. Nevertheless, further investigations in this direction are still called for in order to compare the two methods for increasing numerical resolution and higher dimensional spaces where the accuracy of the BD method, depending on the underlying distribution function, can not be specified 'a priori'.

Appendix A

Review of GENERIC

In this appendix, we present a brief summary of the GENERIC framework [86]. The state of a system at a given level of description is described by a set of variables that form a vector x . The energy and the entropy are two of the basic building blocks of the GENERIC formalism and they should be expressed as functions of the state variables at the given level of description. The GENERIC dynamic equations are given then by

$$\frac{dx}{dt} = L \cdot \frac{\partial E}{\partial x} + M \cdot \frac{\partial S}{\partial x}. \quad (\text{A.1})$$

The first term in the right hand side is named the *reversible* part of the dynamics and the second term is named the *irreversible* part. The predictive power of GENERIC relies in the fact that very strong requirements exist on the matrices L, M leaving relatively small room for the physical input about the system. First, L is antisymmetric whereas M is symmetric and positive semidefinite. Most important, the following *degeneracy* conditions should hold

$$L \cdot \frac{\partial S}{\partial x} = 0, \quad M \cdot \frac{\partial E}{\partial x} = 0. \quad (\text{A.2})$$

These properties ensure that the energy is a dynamical invariant, $\dot{E} = 0$, and that the entropy is a non-decreasing function of time, $\dot{S} \geq 0$, as can be proved by a simple application of the chain rule and the equations of motion (A.1). In the case that other dynamical invariants $I(x)$ exist in the system (as, for example, linear or angular momentum), then further conditions must be satisfied by L, M . In particular,

$$\frac{\partial I}{\partial x} \cdot L \cdot \frac{\partial E}{\partial x} = 0, \quad \frac{\partial I}{\partial x} \cdot M \cdot \frac{\partial S}{\partial x} = 0, \quad (\text{A.3})$$

which ensure that $\dot{I} = 0$.

The deterministic equations (A.1) are, actually, an approximation in which thermal fluctuations are neglected. If thermal fluctuations are not neglected, the dynamics is described by the following stochastic differential equations [89]

$$dx = \left[L \cdot \frac{\partial E}{\partial x} + M \cdot \frac{\partial S}{\partial x} + k_B \frac{\partial}{\partial x} \cdot M \right] dt + d\tilde{x}, \quad (\text{A.4})$$

to be compared with the deterministic equations (A.1). The deterministic additional term involving the Boltzmann constant k_B appears due to the stochastic interpretation of the equation which is taken to be the Itô interpretation. The stochastic term $d\tilde{x}$ in Eq. (A.4) is a linear combination of independent increments of the Wiener process. It satisfies the mnemotechnical Itô rule

$$d\tilde{x}d\tilde{x}^T = 2k_B M dt, \quad (\text{A.5})$$

which means that $d\tilde{x}$ is an infinitesimal of order 1/2 [93]. Eq. (A.5) is a compact and formal statement of the Fluctuation-Dissipation theorem.

In order to guarantee that the total energy and dynamical invariants do not change in time, a strong requirement on the form of $d\tilde{x}$ holds,

$$\frac{\partial E}{\partial x} \cdot d\tilde{x} = 0, \quad \frac{\partial I}{\partial x} \cdot d\tilde{x} = 0, \quad (\text{A.6})$$

implying the last equations in (A.2) and (A.3). The geometrical meaning of (A.6) is clear. The random kicks produced by $d\tilde{x}$ on the state x are orthogonal to the gradients of E, I . These gradients are perpendicular vectors (strictly speaking they are one forms) to the hypersurface $E(x) = E_0, I(x) = I_0$. Therefore, the kicks let the state x always within the hypersurface of dynamical invariants.

Appendix B

Microscopic calculation of entropy

In this appendix we compute the entropy of a thermodynamic system composed of a set of N^s solvent molecules and N^d dumbbells. We understand this system as the portion of fluid that constitutes a fluid particle. The dumbbells are a highly simplified model of a real polymer molecule. The purpose of this calculation is to provide specific analytical expressions for the entropy which may have some resemblance with the actual entropy of a dilute polymer system. We denote by z the set of microscopic degrees of freedom of the system, which are $\mathbf{r}_i, \mathbf{p}_i$ for the position and momentum of the solvent molecules, $\mathbf{R}_i, \mathbf{Q}_i$ for the centre of mass and relative position of the dumbbells, and \mathbf{P}_i for the bead momentum. We will denote schematically $\mathbf{r} = \{\mathbf{r}_i, i = 1, \dots, N^s\}$, $\mathbf{R} = \{\mathbf{R}_i, i = 1, \dots, N^d\}$, $\mathbf{Q} = \{\mathbf{Q}_i, i = 1, \dots, N^d\}$. The Hamiltonian is given by

$$\begin{aligned} H(z) &= \sum_i^{N^s} \frac{\mathbf{p}_i^2}{2m_s} + \sum_i^{2N^d} \frac{\mathbf{P}_i^2}{2m_d} \\ &+ V^s(\mathbf{r}) + V^{sd}(\mathbf{r}, \mathbf{R}, \mathbf{Q}) + V^d(\mathbf{Q}). \end{aligned} \quad (\text{B.1})$$

Here we have introduced the potential energy of the solvent molecules $V^s(r)$ which depends only on the coordinates of the solvent molecules, the potential energy of interaction between solvent and beads $V^{sd}(\mathbf{r}, \mathbf{R}, \mathbf{Q})$ of the dumbbells, and finally, the potential energy of interaction of the dumbbells $V^d(\mathbf{R}, \mathbf{Q})$. In order to be able to obtain analytical expressions, we will assume that the suspension is dilute in such a way that the potential energy of interaction between solvent and dumbbells can be neglected in front of the solvent potential energy, this is, $V^{sd}(\mathbf{r}, \mathbf{R}, \mathbf{Q}) = 0$. Also, we will assume that the interaction between different dumbbells is negligible and, therefore, the potential energy of the dumbbells does not depend on the centre of mass variables, i.e., $V^d(\mathbf{R}, \mathbf{Q}) = V^d(\mathbf{Q})$.

The entropy, defined as the logarithm of the “number of microstates” compatible with a given macrostate E, \mathbf{Q} is given by the classic Boltzmann definition

$$S(E, \mathbf{Q}) = k_B \ln \int dz \delta(H(z) - E) \delta(\mathbf{Q}(z) - \mathbf{Q}). \quad (\text{B.2})$$

The measure dz is given by the product of solvent and dumbbell measures

$$dz = \frac{d^{N^s} \mathbf{p} d^{N^s} \mathbf{r}}{h^{DN^s} N^s!} \times \frac{d^{2N^d} \mathbf{P} d^{N^d} \mathbf{Q} d^{N^d} \mathbf{R}}{h^{D2N^d} N^d!}. \quad (\text{B.3})$$

Here, k_B is the Boltzmann constant and h is the Planck constant. The factorials $N^s!$, $N^d!$ come from the quantum indistinguishability of the molecules and dumbbells. Note that the entropy $S(E, \mathbf{Q})$ depends implicitly on N^s, N^d, V , where the volume V appears because the integrals over coordinate variables are defined over the physical volume.

Under the dilute assumption, it is possible to perform explicitly the integrals over the centre of mass variables. In this case, the integrand of (B.2) does not depend on the centre of mass variable and each integral over the centre of mass vector produces just a volume factor V . We can also perform the integral over the elongation variables in the delta functions in Eq. (B.2), with the result

$$\begin{aligned} S(E, \mathbf{Q}) &= k_B \ln \frac{V^{N^d}}{N^d!} \int \frac{d^{2N^d} \mathbf{P}}{h^{D2N^d}} \int \frac{d^{N^s} \mathbf{p} d^{N^s} \mathbf{r}}{h^{DN^s} N^s!} \\ &\times \delta \left(H^s(r, \mathbf{p}) - \left[E - V^d(\mathbf{Q}) - \sum_i \frac{\mathbf{P}_i^2}{2m_d} \right] \right), \end{aligned} \quad (\text{B.4})$$

where the solvent Hamiltonian is

$$H^s(\mathbf{r}, \mathbf{p}) = \sum_i \frac{\mathbf{p}_i^2}{2m_s} + V^s(\mathbf{r}). \quad (\text{B.5})$$

If we introduce the solvent entropy through the usual definition

$$S^s(\mathcal{E}) = k_B \ln \int \frac{d^{N^s} \mathbf{p} d^{N^s} \mathbf{r}}{h^{DN^s} N^s!} \delta(H^s(\mathbf{r}, \mathbf{p}) - \mathcal{E}), \quad (\text{B.6})$$

we can write Eq. (B.4) in the following way

$$\begin{aligned} S(E, \mathbf{Q}) &= k_B \ln \frac{V^{N^d}}{N^d!} \int \frac{d^{2N^d} \mathbf{P}}{h^{D2N^d}} \\ &\times \exp \left\{ \frac{1}{k_B} S^s \left(E - V^d(\mathbf{Q}) - \sum_i \frac{\mathbf{P}_i^2}{2m_d} \right) \right\}. \end{aligned} \quad (\text{B.7})$$

This equation is exact, as far as the dilute assumption holds. Of course, we would like to have a more manageable expression not involving an integral over dumbbell momenta.

For this reason, we will expand the solvent entropy in the following way

$$\begin{aligned}
S^s \left(\mathcal{E} - \sum_i^{2N^d} \frac{\mathbf{P}_i^2}{2m_d} \right) &= S^s(\mathcal{E}) - \frac{1}{T^s(\mathcal{E})} \sum_i^{2N^d} \frac{\mathbf{P}_i^2}{2m_d} \\
&+ \frac{1}{2C_V^s(\mathcal{E})} \left(\sum_i^{2N^d} \frac{\mathbf{P}_i^2}{2m_d} \right)^2 - \dots,
\end{aligned} \tag{B.8}$$

where $\mathcal{E} = E - V^d(\mathbf{Q})$ and we have introduced the usual thermodynamic derivatives of the entropy with respect to the energy, that is, the temperature T^s and the heat capacity at constant volume C_V^s . Note that the solvent entropy is a first order function of its variables, this is,

$$S^s(\mathcal{E}, N^s, V) = N^s s(e, n), \tag{B.9}$$

where $e = \mathcal{E}/N^s$ is the energy per unit molecule and $n = N^s/V$ is the number density. Eq. (B.9) implies the following scaling on the number of solvent molecules N^s of the derivatives of the solvent entropy appearing in Eq. (B.8)

$$\begin{aligned}
\frac{1}{T^s(\mathcal{E})} &= \frac{\partial}{\partial \mathcal{E}} S^s(\mathcal{E}, N^s) = s^{(1)}(e, n) \\
\frac{1}{C_V^s(\mathcal{E})} &= \frac{\partial^2}{\partial \mathcal{E}^2} S^s(\mathcal{E}, N^s) = \frac{1}{N^s} s^{(2)}(e, n) \\
\frac{\partial^M}{\partial \mathcal{E}^M} S^s(\mathcal{E}, N^s) &= \frac{1}{N^{s(M-1)}} s^{(M)}(e, n),
\end{aligned} \tag{B.10}$$

where the superscript (M) denotes the M -th derivative with respect to e of the solvent entropy per molecule $s^s(e, n)$. Given the scaling in Eq. (B.10), we have that (B.7) becomes

$$\begin{aligned}
S(E, \mathbf{Q}) &= k_B \ln \frac{V^{N^d}}{N^{d!}} \exp \left\{ \frac{1}{k_B} S^s(\mathcal{E}) \right\} \\
&\times \int \frac{d^{2N^d} \mathbf{P}}{h^{D2N^d}} \exp \left\{ -\beta^s(\mathcal{E}) \sum_i^{2N^d} \frac{\mathbf{P}_i^2}{2m_d} \right\} \\
&+ \mathcal{O} \left(\frac{1}{N^s} \right),
\end{aligned} \tag{B.11}$$

where we have introduced $\beta^s(\mathcal{E}) = 1/k_B T^s(\mathcal{E})$. The Gaussian integral is now trivially performed and we obtain,

$$\begin{aligned}
S(E, Q) &= S^s(E - V(Q)) + k_B \ln \frac{V^{N^d}}{N^{d!}} \left(\frac{2\pi m_d}{h^2 \beta^s} \right)^{DN^d} \\
&+ \mathcal{O}\left(\frac{1}{N^s}\right).
\end{aligned} \tag{B.12}$$

Of course, within the same approximation of neglecting terms that scale as the inverse of the number of solvent molecules, we can also write

$$\begin{aligned}
S(E, \mathbf{Q}) &= S^s(E) - \frac{V(\mathbf{Q})}{T^s(E)} + k_B \ln \frac{V^{N^d}}{N^{d!}} \left(\frac{2\pi m_d}{h^2 \beta^s} \right)^{DN^d} \\
&+ \mathcal{O}\left(\frac{1}{N^s}\right).
\end{aligned} \tag{B.13}$$

The last term corresponding to the integration over the centre of mass of the dumbbells has the form of an ideal gas contribution. By using Stirling's approximation ($\ln N! \approx N \ln N - N$), this ideal gas term has the usual form

$$\ln \frac{V^{N^d}}{N^{d!} \lambda_d^{DN^d}} = N^d (1 + \ln n^d \lambda_d^D), \tag{B.14}$$

where $n^d = N^d/V$ is the dumbbell density and we have introduced the thermal wavelength of the beads by

$$\lambda_d = \left(\frac{h^2}{2\pi m_d k_B T^s(\mathcal{E})} \right)^{1/2}, \tag{B.15}$$

and our final result is

$$\begin{aligned}
S(E, \mathbf{Q}) &= S^s(E) - \frac{V(\mathbf{Q})}{T^s(E)} + k_B N^d (1 + \ln n^d \lambda_d^D) \\
&+ \mathcal{O}\left(\frac{1}{N^s}\right).
\end{aligned} \tag{B.16}$$

Appendix C

Advection of a vector

We present here an heuristic argument in order to motivate Eq. (4.25). Consider two neighboring points $\mathbf{r}_1, \mathbf{r}_2$ in a velocity field $\mathbf{v}(\mathbf{r})$. After a small time τ , these points have moved to positions $\mathbf{r}'_1, \mathbf{r}'_2$ which are given by

$$\begin{aligned}\mathbf{r}'_1 &= \mathbf{r}_1 + \tau v(\mathbf{r}_1) \\ \mathbf{r}'_2 &= \mathbf{r}_2 + \tau v(\mathbf{r}_2).\end{aligned}\tag{C.1}$$

If we consider the vectors $\Delta\mathbf{r} = \mathbf{r}_2 - \mathbf{r}_1$ and $\Delta\mathbf{r}' = \mathbf{r}'_2 - \mathbf{r}'_1$ we have

$$\Delta\mathbf{r}' = \Delta\mathbf{r} + \tau(v(\mathbf{r}_2) - v(\mathbf{r}_1)).\tag{C.2}$$

By expanding the velocity field $v(\mathbf{r}_2)$ around \mathbf{r}_1 we obtain

$$\Delta\mathbf{r}' = \Delta\mathbf{r} + \tau\Delta\mathbf{r}\cdot\nabla v(\mathbf{r}_1).\tag{C.3}$$

Therefore,

$$\dot{\Delta\mathbf{r}} = \frac{\Delta\mathbf{r}' - \Delta\mathbf{r}}{\tau} = \Delta\mathbf{r}\cdot\nabla v(\mathbf{r}_1),\tag{C.4}$$

which provides the time rate of change in a Lagrangian frame of a small vector $\Delta\mathbf{r}$ as it moves “anchored” with the flow.

Appendix D

Diffusion of dumbbells

Consider a dumbbell diffusing in a fluid at constant temperature. We understand that this fluid is that portion of fluid which is contained in a fluid particle, with respect to the reference frame of the fluid particle and with the temperature corresponding to that fluid particle. For the sake of the discussion, though, we assume the fluid as infinite and at rest. We assume that each bead of the dumbbell is describing a diffusive overdamped motion governed by the following stochastic equations

$$\begin{aligned}d\mathbf{r}^1 &= \frac{\mathbf{F}(\mathbf{r}^1 - \mathbf{r}^2)}{\zeta} + (2D_0)^{1/2} d\mathbf{W}^1 \\d\mathbf{r}^2 &= \frac{\mathbf{F}(\mathbf{r}^2 - \mathbf{r}^1)}{\zeta} + (2D_0)^{1/2} d\mathbf{W}^2,\end{aligned}\tag{D.1}$$

where $\mathbf{r}^1, \mathbf{r}^2$ are the positions of the first and second beads of the microscopic dumbbell, $\mathbf{F}(\mathbf{r}^1 - \mathbf{r}^2)$ is the force that bead \mathbf{r}^2 exerts on \mathbf{r}^1 , and D_0 is the diffusion coefficient of the beads, given by the Stokes-Einstein relation $D_0 = k_B T / 6\pi\eta a$, where a is the bead of radius a and η is the solvent shear viscosity. The vectorial independent increments of the Wiener process satisfy

$$d\mathbf{W}^\alpha d\mathbf{W}^\beta = \delta^{\alpha\beta} \mathbf{1} dt.\tag{D.2}$$

By changing to centre of mass $\mathbf{R} = (\mathbf{r}^1 + \mathbf{r}^2)/2$ and relative coordinate $\mathbf{Q} = \mathbf{r}^1 - \mathbf{r}^2$ variables, we have

$$\begin{aligned}d\mathbf{R} &= (2D_0)^{1/2} \frac{d\mathbf{W}^1 + d\mathbf{W}^2}{2} \\d\mathbf{Q} &= \frac{\mathbf{F}(\mathbf{Q})}{\zeta} + (2D_0)^{1/2} (d\mathbf{W}^1 - d\mathbf{W}^2) \\&= \frac{\mathbf{F}(\mathbf{Q})}{\zeta} + d\tilde{\mathbf{Q}}.\end{aligned}\tag{D.3}$$

In order to compute the diffusive motion of the centre of mass of the dumbbells, we need

$$d\mathbf{R} \cdot d\mathbf{R} = D_0 dt,\tag{D.4}$$

which corresponds to a diffusion coefficient $D_0/2$. The physical meaning of this is that the dumbbell is subject to *two* friction forces (one for each bead), and therefore the centre of mass diffuses with *half* the diffusion coefficient of each bead. We also need to compute

$$d\tilde{\mathbf{Q}} \cdot d\tilde{\mathbf{Q}} = 4D_0 dt. \quad (\text{D.5})$$

This means that the average dumbbell elongation \mathbf{Q} is subject to a random walk with a diffusion coefficient given by $2D_0$.

Appendix E

SPH discretisation of the advection diffusion equation

Consider the advection diffusion equation for the concentration of a passive density $n(\mathbf{r}, t)$ in a velocity field $\mathbf{v}(\mathbf{r}, t)$,

$$\frac{\partial n}{\partial t} = -\nabla \cdot n\mathbf{v} + \nabla \cdot \frac{Tn}{\zeta} \nabla \frac{\mu}{T}, \quad (\text{E.1})$$

where $\mu = \mu(n(\mathbf{r}, t))$ is the chemical potential field and $T = T(\mathbf{r})$ is the temperature field. For a very dilute system, one can use the ideal gas form for the chemical potential $k_B T \ln n$. If we further assume an isothermal system, the above equation becomes

$$\frac{\partial n}{\partial t} = -\nabla \cdot n\mathbf{v} + D\nabla^2 n, \quad (\text{E.2})$$

where $D = k_B T / \zeta$ is the diffusion coefficient and $\zeta = 6\pi\eta a$ is the friction coefficient of the beads of radius a with the solvent of shear viscosity η .

We write Eq. (E.1) in Lagrangian form by using the usual substantial derivative

$$\frac{d}{dt} = \frac{\partial}{\partial t} + \mathbf{v} \cdot \nabla, \quad (\text{E.3})$$

so we obtain

$$\frac{dn}{dt} = -n(\nabla \cdot \mathbf{v}) + \nabla \cdot \frac{Tn}{\zeta} \nabla \frac{\mu}{T}, \quad (\text{E.4})$$

which expresses the time rate of change of the concentration field as we move with the flow field.

Our aim is to discretize (E.4) on the fluid particles following the smoothed particle hydrodynamics philosophy. a discrete version of (E.4) would read

$$\dot{n}_i = -n_i^d (\nabla \cdot \mathbf{v})_i + \left(\nabla \cdot \frac{Tn}{\zeta} \nabla \frac{\mu}{T} \right)_i. \quad (\text{E.5})$$

Instead of working with the density n_i^d we prefer to work with $N_i = n_i/d_i$ the actual number of suspended particles in the fluid particle of volume d_i^{-1} . This variable evolves

according to

$$\dot{N}_i = -N_i \frac{\dot{d}_i}{d_i} - \frac{n_i}{d_i} (\nabla \cdot \mathbf{v})_i + \frac{1}{d_i} \left(\nabla \cdot \frac{Tn}{\zeta} \nabla \frac{\mu}{T} \right)_i. \quad (\text{E.6})$$

This equation is still a meaningless collection of symbols until we specify how the derivatives in the parenthesis are computed. The divergence of the velocity field $(\nabla \cdot \mathbf{v})_i$ at the location of the i -th fluid particle can be computed from Eq. (4.28). The final result can be written as

$$(\nabla \cdot \mathbf{v})_i = \frac{\dot{\mathcal{V}}_i}{\mathcal{V}_i} = -\frac{\dot{d}_i}{d_i}. \quad (\text{E.7})$$

The physical meaning of this equation is clear, the divergence of the velocity field is associated to the relative rate of change of the volume of the fluid particles, as expected. After substitution of Eq. (E.7) into (E.6) one obtains

$$\dot{N}_i = \frac{1}{d_i} \left(\nabla \cdot \frac{Tn}{\zeta} \nabla \frac{\mu}{T} \right)_i, \quad (\text{E.8})$$

and we observe that if the dynamics is given by the advection diffusion equation (E.1) then the rate of change of the number of suspended particles as we follow the fluid is entirely due to irreversible processes (governed by the transport coefficient ζ). This is consistent with our requirement that the reversible part of the dynamics for \dot{N}_i is zero, as expressed in Eqs. (4.33).

We still have to provide an expression for the derivatives appearing in Eq. (E.8). We follow here the interpolant method first proposed by Cleary and Monaghan [94]. As a preliminary, we introduce the isotropic function $F(r)$ through

$$\nabla W(r) = -\mathbf{r}F(r), \quad (\text{E.9})$$

which satisfies

$$\int d\mathbf{r} \mathbf{r} \cdots \mathbf{r} F(r) = 0, \quad (\text{E.10})$$

if the number of \mathbf{r} 's is odd, by isotropy. It also satisfies

$$\int d\mathbf{r} \mathbf{r} \mathbf{r} \mathbf{r} F(r) = \mathbf{1}, \quad (\text{E.11})$$

as can be proved from

$$\int d\mathbf{r} \mathbf{r} \nabla W(r) = -\mathbf{1}. \quad (\text{E.12})$$

This equation is obtained from a partial integration and the normalisation of the weight function $W(r)$.

Now, consider the following integral

$$\int d\mathbf{r} (B(\mathbf{r}') + B(\mathbf{r}))(A(\mathbf{r}') - A(\mathbf{r}))F(|\mathbf{r} - \mathbf{r}'|), \quad (\text{E.13})$$

where $A(\mathbf{r}), B(\mathbf{r})$ are arbitrary functions that change slowly on the scale of the range of $W(r)$ and $F(r)$. By Taylor expanding $A(\mathbf{r}'), B(\mathbf{r}')$ around \mathbf{r} , neglecting terms of order higher than the second, and using Eqs. (E.10), (E.11) we obtain that the above integral is given by $\nabla \cdot (B(\mathbf{r})\nabla A(\mathbf{r}))$, up to terms involving higher order derivatives. The next step in SPH is to discretize the integral on the locations of the particles

$$\begin{aligned} & \int d\mathbf{r} (B(\mathbf{r}_i) + B(\mathbf{r})) (A(\mathbf{r}_i) - A(\mathbf{r})) F(|\mathbf{r} - \mathbf{r}_i|) \\ & \approx \sum_j \frac{1}{d_j} (B(\mathbf{r}_i) + B(\mathbf{r}_j)) (A(\mathbf{r}_i) - A(\mathbf{r}_j)) F(|\mathbf{r}_j - \mathbf{r}_i|). \end{aligned} \quad (\text{E.14})$$

So finally, we obtain the following interpolant for computing the second derivatives at a particle location, i.e.

$$(\nabla \cdot (B(\mathbf{r})\nabla A(\mathbf{r})))_i \approx \sum_j \frac{1}{d_j} (B_i + B_j) A_{ij} F_{ij}, \quad (\text{E.15})$$

where $B_i = B(\mathbf{r}_i)$, $A_{ij} = A(\mathbf{r}_i) - A(\mathbf{r}_j)$ and $F_{ij} = F(|\mathbf{r}_j - \mathbf{r}_i|)$.

With this result (E.15) inserted into (E.8), we can readily obtain a discretized version of Eq. (E.1) on the Lagrangian grid of moving fluid particles in the form

$$\begin{aligned} \dot{N}_i &= \frac{1}{d_i} \left(\nabla \cdot \frac{Tn}{\zeta} \nabla \frac{\mu}{T} \right)_i \\ &= \sum_j \frac{F_{ij}}{d_j d_i} \left(\frac{T_i n_i}{\zeta} + \frac{T_j n_j}{\zeta} \right) \left(\frac{\mu_i}{T_i} - \frac{\mu_j}{T_j} \right). \end{aligned} \quad (\text{E.16})$$

Note that this equation conserves the total number of suspended particles, $\sum_i \dot{N}_i = 0$.

Bibliography

- [1] M. J. Crochet, A. R. Davies, and K. Walters, *Numerical Simulation of Non-Newtonian Flow* (Elsevier, Amsterdam, 1984)
- [2] R. Keunings, *Simulation of viscoelastic fluid flow*, in: C.L. Tucker III, (Ed.), *Fundamentals of Computer Modeling for Polymer Processing* (Hanser, Munich, 1989) pp. 402.
- [3] F. P. T. Baaijens, Mixed finite element methods for viscoelastic flow analysis: a review, *J. Non-Newt. Fluid Mech.* **79**, 361 (1998).
- [4] R. B. Bird, R. C. Armstrong. O. Hassager *Dynamics of Polymeric Liquids*, Vol. 1 (John Wiley, NY, 1976).
- [5] P. Ilg, *Reduced Description of Kinetic Models of Polymer Dynamics*, Ph.D. Thesis, Wissenschaft und Technik Verlag, Berlin, 2002.
- [6] R. I. Tanner, *Engineering Rheology* (Clarendon Press, Oxford, 1988).
- [7] R. G. Larson, *Constitutive Equations of Polymer Melts and Solutions* (Butterworths, Boston, 1987).
- [8] R. G. Owens and T. N. Phillips, *Computational rheology* (Imperial College Press, London, 2002).
- [9] R. Keunings, Micro-Macro methods for the multiscale simulations of viscoelastic flow using molecular models of kinetic theory , to appear in *Rheology Reviews 2004*, D.M. Bindings and K. Walters (2003).
- [10] A. Lozinski, C. Chauviere, J. Fang and R. G. Owens, Fokker-Planck simulations of fast flows of melts and concentrated polymer solutions in complex geometries, *J. Rheol.* **47**(2), 535 (2002).
- [11] M. Laso and H.C. Öttinger, Calculation of viscoelastic flow using molecular models: the CONFFESSIT approach. *J. Non-Newt. Fluid Mech.* **47**, 1 (1993).
- [12] M. A. Hulsen, A. P. G. van Heel, and B. H. A. A. van den Brule, Simulation of viscoelastic flows using Brownian configuration fields, *J. Non-Newt. Fluid Mech.* **70**, 79 (1997).

- [13] P. Halin, G. Lielens, R. Keunings, and V. Legat, The Lagrangian Particle Method for Macroscopic Micro-Macro Viscoelastic Flow Computations, *J. Non-Newt. Fluid Mech.* **79**, 387 (1998).
- [14] L. B. Lucy, A numerical approach to the testing of the fission hypothesis, *Astron. J.* **83**, 1013 (1977).
- [15] R. A. Gingold and J. J. Monaghan, Smoothed particle hydrodynamics theory and application to non-spherical stars, *Mon. Not. R. Astron. Soc.* **181**, 375 (1977).
- [16] H. Takeda, S. M. Miyama and M. Sekiya, Numerical Simulation of Viscous Flow by Smoothed Particle Hydrodynamics, *Prog. Theor. Phys.* **92**(5), 939 (1994).
- [17] J. J. Monaghan, Simulating Free Surface Flows with SPH, *J. Comput. Phys.* **110**, 399 (1994).
- [18] S. Siegler, and H. Riffert, Smoothed Particle Hydrodynamics Simulations of Ultra-relativistic Shocks with Artificial Viscosity. *Astrophys. J.* **531**, 1053 (2000).
- [19] L. D. Libersky, A. G. Petschek, T. C. Carney, J. R. Hipp, and F. A. Allahdadi, High Strain Lagrangian Hydrodynamics, *J. Comput. Phys.* **109**, 67 (1993).
- [20] A. G. Petschek and L. D. Libersky, Cylindrical Smoothed Particle Hydrodynamics, *J. Comput. Phys.* **109**, 76 (1993).
- [21] L. D. Libersky and A. G. Petschek, *Smooth Particle Hydrodynamics With Strength of Materials*, in: *Advances in the Free-Lagrange Method*, Moran, WY, USA, June 1990, edited by H. E. Trease, M. J. Fritts and W. P. Crowley, *Lect. Notes in Phys.* (Springer-Verlag, New York/Berlin, 1991), Vol. 395, p. 248.
- [22] C. Maveyraud, W. Benz, A. Sornette, and D. Sornette, Solid friction at high sliding velocities: An explicit three-dimensional dynamical smoothed particle hydrodynamics approach, *J. Geophys. Res.* **104**, 28769 (1999).
- [23] R. Speith, H. Riffert, and H. Ruder, *Numerical Fluid Dynamics in Astrophysics with Smoothed Particle Hydrodynamics*, in: Bungartz H.-J., Durst F., Zenger C. (eds.): *High Performance Scientific and Engineering Computing, Lecture Notes in Computational Science and Engineering* (1999) pp. 417.
- [24] O. Flebbe, S. Münzel, H. Herold, H. Riffert, H. Ruder, Smoothed Particle Hydrodynamics: Physical Viscosity and the simulation of accretion disk, *Astroph. J.* **431**, 754 (1994).
- [25] C.V. Chaubal, A. Srinivasan, Ö. Egecioglu, and L.G. Leal, SPH techniques for the solution of kinetic theory problems *J. Non-Newt. Fluid Mech.* **70**, 125 (1997).
- [26] T. Bubeck, M. Hipp, S. Httemann, S. Kunze, M. Ritt, W. Rosenstiel, H. Ruder, and R. Speith, *Parallel SPH on Cray T3E and NEC SX-4 using DTS*, in: Krause E., Jger W. (eds.): *Proc. High Performance Computing in Science and Engineering 1998* (1999) pp. 396.

- [27] R. Di Lisio, E. Grenier, and M. Pulvirenti, The convergence of the SPH method, *Computer Math. Applic.* **35**, 95 (1998).
- [28] P. Español, M. Serrano, and H. C. Öttinger, Thermodynamically admissible form for discrete hydrodynamics, *Phys. Rev. Lett.* **83**, 4552 (1999).
- [29] P. Espanol, *Europhys. Lett.* **39**, 606 (1997); *Phys. Rev. E* **57**, 2930 (1998).
- [30] B.I.M. ten Bosch, On a extension of Dissipative Particle Dynamics for viscoelastic flow modelling, *J. Non-Newt. Fluid Mech.* **83**, 231 (1999).
- [31] S. Shao, E. Y. M. Lo, Incompressible SPH method for simulating Newtonian and non-Newtonian flows with a free surface, *Advances in Water Resources* **26** (7), 787 (2003).
- [32] W. Benz, *Smoothed Particle Hydrodynamics: A Review*, in: *The Numerical Modelling of Nonlinear Stellar Pulsation: Problems and Prospects, Les Arcs, France, March 1989*, edited by J. R. Buchler, Nato ASI Series (Kluwer Academic, Boston, MA, 1990), Vol. 302, p. 269.
- [33] J. Monaghan, Smoothed Particle Hydrodynamics, *Annu. Rev. Astron. Astrophys.* **30**, 543 (1992).
- [34] J. J. Monaghan, An Introduction to SPH, *Comp. Phys. Commun.* **48**, 89 (1988).
- [35] R. W. Hockney and J. W. Eastwood, *Computer Simulation Using Particles* (McGraw-Hill, New York, 1981)
- [36] M. P. Allen and D. J. Tildesley, *Computer Simulation of Liquids* (Clarendon Press, Oxford, 1987).
- [37] O. Kum, W. G. Hoover, Viscous conducting flows with smooth-particle applied mechanics, *Phys. Rev. E* **52**, 4889 (1995).
- [38] S. J. Cummins, M. Rudman, An SPH Projection Method, *J. Comp. Phys.* **152**, 584 (1999).
- [39] G. K. Batchelor, *An Introduction to Fluid Dynamics* (Cambridge University Press, Cambridge, 1967).
- [40] L. D. Landau and E. M. Lifshitz, *Fluid Mechanics* (Pergamon Press, London, 1959).
- [41] J. Von Neumann and R. D. Richtmeyer, A Method for the Numerical Calculation of Hydrodynamic Shocks, *J. Appl. Phys.* **21**, 232 (1950).
- [42] J. P. Morris, P. J. Fox, and Y. Zhu, Modeling Low Reynolds Number Incompressible Flows Using SPH, *J. Comput. Phys.* **136**, 214 (1997).
- [43] J. P. Morris and J. J. Monaghan, A Switch to Reduce SPH Viscosity, *J. Comput. Phys.* **136**, 41 (1997).

- [44] J. P. Morris, *Analysis of Smoothed Particle Hydrodynamics with Applications*, Ph.D. Thesis, Monash University, Melbourne, Australia, 1996.
- [45] W. G. Hoover and S. Hess, Equilibrium and nonequilibrium thermomechanics for an effective pair potential used in smooth particle applied mechanics, *Physica A* **231**, 425 (1996).
- [46] H. A. Posch, W. G. Hoover and O. Kum, Steady-state shear flows via nonequilibrium molecular dynamics and smooth-particle applied mechanics, *Phys. Rev. E* **52**, 1711 (1995).
- [47] W. H. Press, S. A. Teukolsky, W. T. Vetterling, and B. P. Flannery, *Numerical Recipes in C: The Art of Scientific Computing* (Cambridge University Press, Cambridge, 1992), p. 847.
- [48] J. H. Ferziger, M. Peric, *Computational Methods for Fluid Dynamics* (Springer-Verlag Berlin, 1997).
- [49] R. L. Panton, *Incompressible Flow* (John Wiley, NY, 1984).
- [50] M. Ellero, M. Kröger and S. Hess, Viscoelastic flows studied by Smoothed Particle Dynamics. *J. Non-Newtonian Fluid Mech.* **105**, 35 (2002).
- [51] D. D. Joseph, *Fluid Dynamics of Viscoelastic Liquids* (Springer-Verlag Berlin, Applied mathematical sciences, v.84, 1990).
- [52] A. W. Lees and S. F. Edwards, The computer study of transport process under extreme conditions, *J. Phys.* **C5**, 1921 (1972).
- [53] A. Bömer and T. Klimpel, Plastic deformation of corrugated rails - a numerical approach using data of rail steel, *Wear* **253**, 150 (2002).
- [54] K. Sugino, H. Kageyama and C. Urashima, Metallurgical improvement of rail for the reduction of rail-wheel contact fatigue failures, *Wear* **144**, 319 (1991).
- [55] B. N. J. Perrson, *Sliding Friction* (Springer-Verlag, Berlin, 1998).
- [56] J. Ahlström and B. Karlsson, Microstructural evaluation and interpretation of the mechanically and thermally affected zone under railway wheel flats, *Wear* **232**, 1 (1999).
- [57] H. Krause and C. Schroelkamp, Influence of non-metallic inclusions on the wear behaviour of ferrous materials in nominally dry friction systems, *Wear* **120**, 353 (1987).
- [58] H. T. Zhu and H. M. Zbib, A macroscopic model for plastic flow in metal-matrix composites, *Int. J. of Plasticity* **11** (4), 471 (1995).

- [59] S. Piazzolo, P. D. Bons and C. W. Passchier, The influence of matrix rheology and vorticity on fabric development of populations of rigid objects during plane strain deformation, *Tectonophysics* **351**, 315 (2002).
- [60] Stankovic, M. Kröger, and S. Hess, Recognition and analysis of local structure in polycrystalline configurations, *Comput. Phys. Commun.* **145**, 371 (2002).
- [61] M. Kröger, I. Stankovic, and S. Hess, Towards multiscale modeling of metals via embedded particle computer simulations, *Multiscale Model. Simul.* **1**, 25 (2003).
- [62] Stankovic, S. Hess, and M. Kröger, Structural changes and viscoplastic behavior of a generic embedded atom model metal in steady shear flow, *Phys. Rev. E* **69**, 021509 (2004).
- [63] R. M. Christensen, *Mechanics of composite materials* (Wiley, New York, 1979).
- [64] Q. S. Yang and Q. H. Qin, Micro-mechanical analysis of composite materials by BEM, to appear in *Eng. Analys. with Bound. Elem.*(2004).
- [65] P. Gilormini and J. C. Michel, Finite element solutions of the problem of a spherical inhomogeneity in an infinite power-law viscous matrix, *Eur. J. Mech. A/Solids* **17**, 725 (1998).
- [66] G. Pennacchioni, L. Fasolo, M. M. Checchi and L. Salasnich, Finite-element modelling of simple shear flow in Newtonian and non-Newtonian fluids around a circular rigid particle, *J. Struct. Geol.* **22**, 683 (2000).
- [67] T. Masuda and N. Mizuno, Deflection of non-Newtonian simple shear flow around a rigid cylindrical body by the Finite Element Method, *J. Struct. Geol.* **18** (8), 1089 (1996).
- [68] S. K. Samanta, N. Mandal and C. Chakraborty, Flow pattern around rigid inclusions in a multiple inclusion system undergoing bulk simple shear deformations, *J. Struct. Geol.* **25**, 209 (2003).
- [69] S. Chapman and T. G. Cowling, *The Mathematical Theory of Non-Uniform Gases*, (Cambridge University Press Cambridge, 1970).
- [70] D. Doolen, *Lattice Gas Methods for partial differential equations*, (Addison-Wesley, 1987).
- [71] P. J. Hoogerbrugge and J. M. V. A. Koelman, Simulating Microscopic Hydrodynamics Phenomena with Dissipative Particle Dynamics, *Europhys. Lett.* **19**, 155 (1992).
- [72] P. Español and P. Warren, Statistical mechanics of Dissipative Particle Dynamics, *Europhys. Lett.***30**, 191 (1995).
- [73] P. Español and M. Revenga, Smoothed Dissipative Particle Dynamics, *Phys. Rev. E* **67**, 026705 (2003).

- [74] M. Ellero, P. Español and E. G. Flekkoy, Thermodynamically consistent fluid particle model for viscoelastic flows, *Phys. Rev. E* **68**, 041504 (2003).
- [75] J. M. V. A. Koelman and P. J. Hoogerbrugge, Dynamic simulations of hard-sphere suspensions under steady state shear, *Europhys. Lett.* **21**, 363 (1993).
- [76] E. S. Boek, P. V. Coveney, H. N. W. Lekkerkerker, and P. van der Schoot, Simulating the rheology of dense colloidal suspensions using dissipative particle dynamics, *Phys. Rev. E* **55**, 3124 (1997).
- [77] M. Whittle and E. Dickinson, On simulating colloids by dissipative particle dynamics: Issues and complications, *Journal of Colloid and Interface Science* **242**, 106 (2001).
- [78] A. G. Schlijper, P. J. Hoogerbrugge and C. W. Manke, Computer simulation of dilute polymer solutions with the dissipative particle dynamics method, *J. Rheol.* **39**, 567 (1995).
- [79] N. A. Spenley, Scaling laws for polymers in dissipative particle dynamics, *Europhys. Lett.* **49**, 534 (2000).
- [80] P. V. Coveney and K. Novik, Erratum: Computer simulations of domain growth and phase separation in two-dimensional binary immiscible fluids using dissipative particle dynamics, *Phys. Rev. E* **55**, 4831 (1997).
- [81] S. I. Jury, P. Bladon, S. Krishna, and M. E. Cates, Test of dynamical scaling in three-dimensional spinodal decomposition, *Phys. Rev. E* **59**, R2535 (1999).
- [82] C. M. Wijmans, B. Smit, and R. D. Groot, Phase behavior of monomeric mixtures and polymer solutions with soft interaction potentials, *J. Chem. Phys.* **114**, 7644 (2001).
- [83] P. B Warren, Dissipative particle dynamics, *Curr. Opinion Colloid Interface Sci.* **3**, 620 (1998).
- [84] P. Español, *Dissipative Particle Dynamics*, in: *Trends in Nanoscale Mechanics: Analysis of Nanostructured Materials and Multi-Scale Modeling*, edited by V. M. Harik and M. D. Salas editors (Kluwer 2003).
- [85] K. Feigl, M. Laso, and H. C. Öttinger, The CONNFFESSIT approach for solving a two-dimensional viscoelastic fluid problem, *Macromolecules* **28**, 3261 (1995).
- [86] H. C. Öttinger and M. Grmela, Dynamics and Thermodynamics of complex fluids. II. Illustrations of a general formalism, *Phys. Rev. E* **56**, 6633 (1997).
- [87] M. Serrano and P. Español, Thermodynamically consistent mesoscopic fluid particle model, *Phys. Rev. E* **64**, 46115, (2001).
- [88] E. G. Flekkoy, P. V. Coveney, and G. D. Fabritiis, Foundations of dissipative particle dynamics, *Phys. Rev. E* **62**, 2140 (2000).

- [89] H. C. Öttinger, General projection operator formalism for the dynamics and thermodynamics of complex fluids, *Phys. Rev. E* **57**, 1416, (1998).
- [90] H. C. Öttinger, B. H. A. A. van den Brule and M. A. Hulsen, Brownian configuration fields and variance reduced CONNFFESSIT, *J. Non-Newt. Fluid Mech.* **70**, 255 (1997).
- [91] J. J. Monaghan, *New Developments in Smoothed Particle Hydrodynamics*, in: *Meshfree Methods for Partial Differential Equations*, Lecture notes in computational science and engineering, Vol. 26 edited by M. Griebel and M. A. Schweitzer (Springer-Verlag, Berlin, 2002).
- [92] M. Dressler, B. J. Edwards and H. C. Öttinger, *Rheol. Acta* **38**, 117 (1999).
- [93] C. Gardiner, *Handbook of Stochastic Methods* (Springer-Verlag, Berlin, 1983).
- [94] P. W. Cleary and J. J. Monaghan, Conduction Modelling using Smoothed Particle Hydrodynamics, *J. Comp. Phys.* **148**, 227 (1999).
- [95] M. Rappaz, M. Bellet and M. Deville, *Numerical Modeling in Material Science and Engineering* (Springer-Verlag, Berlin Heidelberg, 2003)
- [96] A. Chandra and S. Mukherjee, *Boundary Element Methods in Manufacturing* (Oxford University Press, 1997)
- [97] H.C. Öttinger, *Stochastic Processes in Polymeric Fluids* (Springer, Berlin Heidelberg New York, 1996)
- [98] Q. Zhou and R. Akhavan, A comparison of FENE and FENE-P dumbbells and chain models in turbulent flow, *J. Non-Newtonian Fluid Mech.* **109**, 115 (2003).
- [99] M. Melchior and H. C. Öttinger, Variance reduced simulations of polymer dynamics, *J. Chem. Phys.* **105**(8), 3316 (1996).
- [100] X. Gallez, P. Halin, G. Lielens, R. Keunings and V. Legat, The adaptative Lagrangian particle method for macroscopic and micro-macro computations of time-dependent viscoelastic flows, *Comput. Methods Appl. Mech. Engrg.* **180**, 345 (1999).
- [101] P. Wapperom, R. Keunings and V. Legat, The backward-tracking Lagrangian particle method for transient viscoelastic flows, *J. Non-Newtonian Fluid Mech.* **91**, 273 (2000).
- [102] M. Ellero and M. Kröger, The hybrid BDDFS method: memory saving approach for CONNFFESSIT-typer simulations , *J. Non-Newtonian Fluid Mech.* (2004) in press.
- [103] X.-J. Fan, Viscosity, first normal stress-coefficients, and molecular stretching in dilute polymer solutions, *J. Non-Newtonian Fluid Mech.* **17**, 125 (1985).

- [104] X.-J. Fan, Viscosity, first normal stress-coefficient and molecular stretching in concentrated solutions and melts, *J. Non-Newtonian Fluid Mech.* **17**, 251 (1985).
- [105] J. K. Suen, Y. L. Joo and R. C. Armstrong, Molecular orientation effects in viscoelasticity, *Annu. Rev. Fluid Mech.* **134**, 417 (2002).
- [106] A. Lozinski and C. Chauviere, A fast solver for Fokker-Planck equation applied to viscoelastic flow calculations, submitted to Elsevier Science, (2003).
- [107] C. Chauviere, J. Fang, A. Lozinski and R. G. Owens, On the numerical simulation of flows of polymer solutions using high-order methods based on the Fokker-Planck equation, *Int. J. Mod. Phys. B* **17**, 9 (2003).
- [108] M. Kröger, Flow-alignment and rheology of polymer melts. Computation of the single-link orientational distribution function. *Makromol. Chem. – Macromol. Symp.* **81** (1994) 83.
- [109] M. Kröger, Simple models for complex nonequilibrium fluids, *Phys. Rep.* **390**, 453 (2004).
- [110] M. Herrchen and H. C. Öttinger, A detailed comparison of various FENE dumbbell models *J. Non-Newtonian Fluid Mech.* **68**, 17 (1997).
- [111] R. Keunings, On the Peterlin approximation for finite extensible dumbbells, *J. Non-Newtonian Fluid Mech.* **68**, 85 (1997).
- [112] P. Ilg, E. De Angelis, I. V. Karlin, C. M. Casciola and S. Succi, Polymer dynamics in wall turbulent flow, *Europhys. Lett.* **58** (4), 616 (2002).
- [113] M. Laso, M. Picasso, and H. C. Öttinger, 2D time-dependent viscoelastic flow calculations using CONNFFESSIT, *AIChE J.* **43**, 877 (1997).
- [114] R. M. Jendrejack, J. J. de Pablo and M. D. Graham, A method for multiscale simulations of flowing complex fluids, *J. Non-Newtonian Fluid Mech.* **108**, 123 (2002).
- [115] J. Bonvin and M. Picasso, Variance reduction methods for CONNFFESSIT-like simulations, *J. Non-Newtonian Fluid Mech.* **84**, 191 (1999).
- [116] T. W. Bell, G. H. Nyland, J. J. de Pablo, and M.D. Graham, Combined Brownian dynamics and spectral simulation of the recovery of polymeric fluids after shear flow, *Macromolecules* **30**, 1806 (1997).